Title
Design, Control, and Analysis of an Electrostatic Bearing

Author
Andonian, Michael

Publication Date
2020

Peer reviewed|Thesis/dissertation

UNIVERSITY OF CALIFORNIA
Los Angeles

Design, Control, and Analysis of an Electrostatic Bearing

A dissertation submitted in partial satisfaction
of the requirements for the degree
Doctor of Philosophy in Mechanical Engineering

by

Michael Andonian

2020

ABSTRACT OF THE DISSERTATION

Design, Control, and Analysis of an Electrostatic Bearing

by

Michael Andonian
Doctor of Philosophy in Mechanical Engineering
University of California, Los Angeles, 2020
Professor Robert T. M'Closkey, Chair

The purpose of this research is to create a tool for electrostatically suspending planar, disk-shaped objects towards the effort to measure and analyze stem motion of planar disk-shaped resonators as a function of mass perturbations. Planar disk-shaped resonators, generally, operate as sensors which measure an object's rate of rotation. When measuring the vibratory response, resonant modes appear in degenerate pairs which are exploited in measurements to achieve exceptional signal-to-noise ratios relative to various noise sources. However, assorted errors and nonidealities in a resonator's fabrication "detune" the resonant frequencies. The resonator may be "tuned" by converging the split frequencies together through systematic mass modifications with post-fabrication techniques. No quantitative analysis has demonstrated changes in the dynamics at the resonator stem as a result of the mass perturbations. By electrostatically suspending a disk resonator, hard-mounts are removed, and repeatable and controllable boundary conditions are established for comparing analogous resonators. The electrostatic suspension of a disk is representative of an "electrostatic bearing" .

Two systems are modeled and analyzed to assess the dynamics of an electrostatically controlled object and assist in the design of stabilizing controllers. Inherently, each system is unstable and requires feedback control to adjust the forces acting on the electrostatically suspended body until a desired reference is achieved. Further, electrical measurements

representative of the body's pose require compensation to achieve stability due to the colocation of the force actuation and sensing pick-off. A single degree of freedom system is initially fabricated and analyzed both experimentally and through the use of a modeling paradigm to aid in the development of the more complicated suspension platform, debug the electronics interface, and determine the methods of signal conditioning. The modeling paradigm, fabrication techniques, and electronics interface are then extended to a suspended disk platform. The model indicates the suspension system is not strongly stabilizable if only the electrode-disk gap measurements are available. Consequently, an unstable controller is proposed that stabilizes the disk. To control the lateral degrees of freedom, measurements of the disk's lateral position are used to regulate its in-plane motion. Comparisons of the model results and experimental results are given.

The dissertation of Michael Andonian is approved.

James S. Gibson

Sudhakar Pamarti

Tsu-Chin Tsao

Robert T. M'Closkey, Committee Chair

University of California, Los Angeles

2020

To Florence Miyasato,

TABLE OF CONTENTS

LIST OF FIGURES

LIST OF TABLES

ACKNOWLEDGMENTS

I am deeply grateful for the support, advice, and patience of all the individuals who have played a role in encouraging me through the duration of my time at UCLA. I have been fortunate to be surrounded by so many people willing to help me see this research through to the end. In many ways, this dissertation is a testament to their sustained aid and contributions.

I would like to thank my thesis committee: Drs. Steve Gibson, Tsu-Chin Tsao, and Sudhakar Pamarti. Their insights and advice have always proved invaluable and their courses helped me grow as an engineer and researcher. Thank you to the many professors who have challenged me along the way: Drs. Tetsuya Iwasaki, Jason Speyer, Robert Kinsey, Hassan Babaie, and Jeff Eldredge. A big thank you to the staff in the MAE Department: Marla Cooper, Angie Castillo, Abel Lebon, Lance Kono, and Collin Llewellyn. I would also like to thank Benjamin Tan and Miguel Lozano for all the times I dropped in on them, needing help at a moments notice, and how willing the two of them were to assist.

I am enormously thankful for the support provided to me by the Nanoelectronics Research Facility at UCLA. Without them, the entirety of my research would not have been possible. Thank you to Hoc Ngo, Tom Lee, and Brian Matthews for your guidance through the various steps of my fabrication process. Also, thank you to Joe Zendejas, who has advised me through the fabrication process from the start and made sure I produced exactly what I was looking for every time.

Thank you to all of my peers in Dr. M'Closkey's lab along the way. I am sincerely privileged to have worked with a group of friends over the years. Dr. Dennis Kim, in many ways, I am a protege of you as well. You took me under your wing from the moment I stepped foot in Bob's lab and set an example of professionalism and dedication. To Drs. Amir Behbahani and Howie Ge, thank you for your advice and support over the years. The three of us made a great team in 107. I would also like to thank Stephen Schein and

Kenneth Pyle. Working with the two of you has been nothing short of entertaining.

Thank you to my friends, Roberto Cortes, Humberto Gonzalez, Andrew Grant, Quyen Vu, Greg Foster, Julia and Margo Tyack, James Duran, Jesus Chuy Lopez, Robert Young, Justin Toyofuku, Justin Kong, Alejandro Guillen, and Matt Asada.

A special thank you to Drs. Monique Chyba and George Wilkens. My academic journey would have never begun without your influence and support.

Of course, thank you to Dr. Robert T. M'Closkey. I will never forget the patience and respect you have shown me over the years. Your mentorship has extended beyond academics and you have always set the example for high integrity and standards. I will forever be thankful for your trust in me and help in navigating my academic and personal pursuits. I have thrived as a student, researcher, professional, and person under your guidance. This research and my future success will always be attributed to your commitment and counsel.

Lastly, my most earnest thank you to my family. This thesis is a true exemplification of your patience, love, and support. I thank all of my aunties, uncles, and cousins in Hawaii and California for all your love and constant encouragement over the years. A special thank you to Aunty Carrie and Grandma for being my primary support during my time in Hawaii. I could never express how much spending time with the two of you molded me into the person I am today. Thank you to my siblings, Amanda and David, for always keeping me grounded. Knowing I have your support is one of the foundational pieces to any and all success I earn. And of course, thank you to Mom and Dad. All of my achievements are as much yours as they are mine. To say this would not be possible without the two of you vastly understates your commitment and conviction to my pursuits. Thank you for all the love you have committed to me and my siblings.

VITA

Michael Andonian first earned his Bachelors of Science degree in Mathematics at the University of Hawaii at Manoa (UHM) in 2010. During this time, he participated in various undergraduate research projects including navigation of underwater autonomous vehicles, modeling pattern formation in cyanobacteria, and application of statistical tools to identify specific coral reef fish species by their feeding sounds. These projects were supported by the UHM, the National Science Foundation, and the Hawaii Space Grant Consortium.

Michael obtained his Master of Art degree in Mathematics from UHM in 2012 with a focus on applications of geometric control theory. His research extended existing knowledge of the applications to underwater autonomous vehicles and methods of solving the motion planning problem when thruster failure leads to loss in degrees of freedom. In the summer of 2011, he interned at the Jet Propulsion Laboratory with the radio science group, modeling ground-to-orbit communication. Outside of research, he was a member of the Math Department's Student and University Partnership for Educational Renewal in Mathematics, a partnership with Hawaii's Department of Education to promote methods of teaching mathematics in K-12 programs and underserved populations. He was hired as the Program Manager from 2012 to 2013.

Beginning in 2013, he pursued a PhD in Mechanical Engineering with a focus on the control of dynamical systems at University of California, Los Angeles. Michael would earn a Master of Science degree in Mechanical Engineering in 2018 while embracing his role as a teaching assistant (TA) for six years. In his first year as a TA, he was recognized by the Mechanical and Aerospace Engineering Department with its annual TA Award, awarded to a TA based on student evaluations and faculty recommendation. By his third year, he was hired as the department's Teaching Assistant Consultant to train new TAs in their duties and evidence-based teaching practices. His research interests include the control of unstable electromechanical systems, system identification, and filter design.

PUBLICATIONS AND PRESENTATIONS

Identification and compensation of feedthrough in an unstable electrostatic bearing

Michael Andonian and Robert T. M'Closkey, Mechatronics, 2020

Sensing and Control Interface for Precise Gap Control

Michael Andonian and Robert T. M'Closkey, Mechatronics, 2017

Creating Bathymetric Maps Using AUVs in the Magdalena River

Monique Chyba, John Rader, and Michael Andonian, Special Edition of Ship Science and Technology, 2011, Cartagena, Columbia

Geometric Control for Autonomous Underwater Vehicles: Overcoming a Thruster Failure

Sergio Grammatico, Monique Chyba, Michael Andonian, and Andrea Caiti, Decision and Control (CDC), 2010 49th IEEE Conference on, 2010, Atlanta, GA

Trajectory Design for Autonomous Underwater Vehicle for Basin Exploration

Dario Cazzaro, Luca Invernizzi, Monique Chyba, and Michael Andonian, 9th International Conf. on Computer Applications & Information Technology in the Maritime Industries, 2010, Gubbio, Italy

Using Geometric Control to Design Trajectories for an AUV to Map and Sample the Summit of the Loihi Submarine Volcano

Michael Andonian, Dario Cazzaro, Luca Invernizzi, Monique Chyba, and Sergio Grammatico, Autonomous Underwater Vehicles (AUV), 2010 IEEE/OES, 2010, Monterey, CA

CHAPTER 1

Introduction

1.1 Electrostatic Suspension Systems

Electrostatic suspension is realized by levitating an object made of conductive material within a electric field generated (typically) by a stator electrode configuration. These electrodes produce the necessary electric charge for biasing and controlling the test mass about some desired operating gap within the electrodes' geometry. Implementation of the electrostatic force actuation varies, as does the method of gap sensing, between gas, optical, and, most commonly, electrical detection. Regardless, active feedback control of the electric field is required to stabilize the suspended object as a result of the forces acting on the body.

A natural question arises as to the benefits of using electrostatic forces over magnetic forces. When considering a simple magnetostatic system (two magnetic poles separated by an air gap), the energy density of the magnetic field is given by

$$u = \frac{1}{2}\frac{B^2}{\mu_0}$$

where B is the flux density and μ_0 is the permeability of free space. Note, the energy density is independent of the gap of separation. In contrast, electrostatic systems are limited by the breakdown voltage which is dependent on the gap as well as the gas within. As dictated by Paschen's law, the energy density of the electric field increases with the volt-

age breakdown as the gap decreases. With gaps below several microns, electrostatic fields ideally provide the prospect for larger forces. When gaps are on the order of tens or hundreds of microns, the energy density of electric fields is substantially lower and, in such cases, the electrostatic force per unit area is relatively weak compared to magnetostatic force. This discrepancy can be diminished by operating an electrostatic system in vacuum. However, high-voltage and high-speed amplifiers are required to produce the necessary electrostatic forces for stability, raising the overall cost of materials. Nevertheless, one major advantage of electrostatic levitation is the ability to suspend non-ferromagnetic materials directly. Another advantage is simplicity of the electrode geometries, which are often planar, and provide ease in miniaturizing the system whereas the coils in electromagnets are a limiting factor. For the purposes of this thesis, the material of the proof mass to be suspended and the prospect of miniaturization dictated the argument for electrostatic suspension.

As mentioned, the method of the gap sensing and electrostatic force actuation in electrostatic systems varies. Both [JTK99] and [HGW02] employ a transformer scheme where the capacitance measurement is picked-off by a differential amplifier from a reflected impedance measurement. Capacitance measurements are taken using a differential op amp configuration in [GK03]. In [JTK99] the actuation of the proof mass is accomplished by controlling directly the potential on the proof mass, whereas [HGW02] and [GK03] ground the proof mass and control the potential on sets of electrodes. Similarly, [TTM02] directly controls the gap separation with potential drops across electrode pairs while a separate, orthogonal electrode senses the gap and the charge developed on the electrode is converted into a voltage.

Contactless manipulation of planar objects have previously been demonstrated in [WYH10, LHK95, MEF03, TWM12]. First, [WYH10, LHK95] demonstrate the suspension of silicon wafers for the purposes of contactless wafer transport. However, the planar translation of the disk is neglected in developing a model and control architecture. Although it is demonstrated that the disk is suspended, it is unclear whether or not all the measured

degrees-of-freedom are asymptotically stable in the sense of classical control parlance. As indicated in their results, the restoring forces in the lateral directions seem to passively stabilize these degrees-of-freedom. In large part, these forces are effective because of the high electrode voltages and the fact that the disk diameter and electrode geometry are the same size. The latter fact has implications on the effective fringe field forces which are absent in this research. In contrast, [TWM12] and [MEF03] show an electrostatically levitated micro-motor and a suspended ring gyro. One unique aspect of this work is the fabrication process used to create a method for measuring a "yaw" rotation. In addition, a direct method of measuring and controlling lateral translation is presented through in-plane electrodes. In comparison to this research, the effective electrode dimensions of the suspended disk to be presented do not exert strong fringe-field forces on the disk. As such, the lateral degrees-of-freedom must be stabilized by the feedback controller. However, in-plane electrodes are not fabricated to control lateral degrees-of-freedom. Including the lateral degrees-of-freedom in the modeling and analysis reveal strong coupling to the tilt, or angular, disk variables. The control design presented relies on this this coupling. Ultimately, stabilization of the disk's vertical and angular variables also stabilizes its lateral variables.

1.2 Electrostatic Suspension of Planar Resonators

The ultimate goal of this research is to develop an electrostatic suspension platform for experimentally quantifying changes in the dynamics of planar disk resonators with regard to perturbations of the resonators mass distribution. Motion at the stem, attachment point or anchor changes as a function of these perturbations is of particular interest. An example of the sort of planar resonator that will be tested with such a platform is discussed in [BKS17, SKS15] Generally, these devices operate as sensors which measure an object's rate of rotation. The axisymmetric form of an ideal vibrating ring produces resonant modes that appear in degenerate pairs, meaning the modes share the same reso-

nant frequency. These frequencies are exploited in measurements to achieve exceptional signal-to-noise ratios relative to various noise sources in the sensing instruments. However, assorted errors and nonidealities in a resonator's fabrication "detune" the resonant frequencies. The resonator may be "tuned" by converging the split frequencies together through systematic mass modifications in prescribed spoke sites with post-fabrication techniques. As mentioned, it is desirable to quantify how the reaction at the resonator stem-substrate interface changes under such modifications. Further, one established fact is the stem sinks the energy from the vibrating resonator. Yet no quantitative analysis has demonstrated changes in the dynamics at the stem as a result of the mass perturbations. Tests measuring the vibratory response of disks resonators involve a resonator mounted on some substrate. The lack of standardization with the stem-mount interface limits the scope of quantifying energy loss through the stem.

The purpose of this research is to address this problem by creating a tool to measure and analyze the stem motion as a function of mass perturbations. By electrostatically suspending a disk resonator, hard-mounts are removed, and repeatable and controllable boundary conditions, which do not introduce thermally-generated stresses in the resonator such as hard-mounts with thermally mismatched materials, are established for comparing analogous resonators. This device is representative of an "electrostatic bearing" . The nature of this research poses several problems that will be addressed:

- The unstable nature of the system requires feedback control to adjust forces acting on the disk until some reference command is achieved.

- Position measurements are corrupted by the control signals due to both the electrode configuration and electronics interface. These measurements require compensation to accurately estimate the dynamics of a suspended disk.

- Maximally flat surfaces are required across ranges several orders of magnitude larger than the gaps formed between the disk and adjacent surfaces. This presents unique fabrication challenges.

- Models of the system need to be built for complete analysis and to help develop intuition into the control design.

An electrostatically suspended object's configuration (in the classical dynamics sense of a position and orientation relative to an inertial reference frame) can be described by six degrees of freedom (DOF). For the purpose of suspending a planar resonator, the "yaw" degree of freedom would not be actively controlled, reducing the control problem to a 5-DOF system. Suspending the disk resonator is accomplished controlling the voltage on antagonistically arranged electrode pairs that apply attractive electrostatic forces (both upwards and downwards) to the disk. By measuring the capacitance between these same pairs of electrodes and the disk, an estimate of the both disk-electrode gaps can be inferred.

1.3 Transduction Description and Equations of Motion

With regards to the differential capacitance transduction and electrostatic forcing, the work here most closely resembles the scheme found in [Atk67] and [AB75], where both the gap sensing and control are achieved with a single pair of electrodes. In the research to follow, an equipotential object is situated over some electrode pattern. To develop the necessary voltages on the electrodes for the electrostatic forces, a specialized transformer is used. This transformer, shown in Fig. 1.1, consists of two primary legs wound such that the two primary inductances are equal and connected together via a center tap with the other two leads connected to pair of electrodes.

The center tap is connected to a primary lead of an auxiliary transformer (see Fig. 1.2), the secondary of which is driven by a high output current operational amplifier configured as a non-inverting amplifier with a variable gain. A signal generator drives the input of this op amp with a sinusoid, producing a large sinusoidal current which is stepped down by the subsequent transformer and runs to the center taps of the specialized transformers.

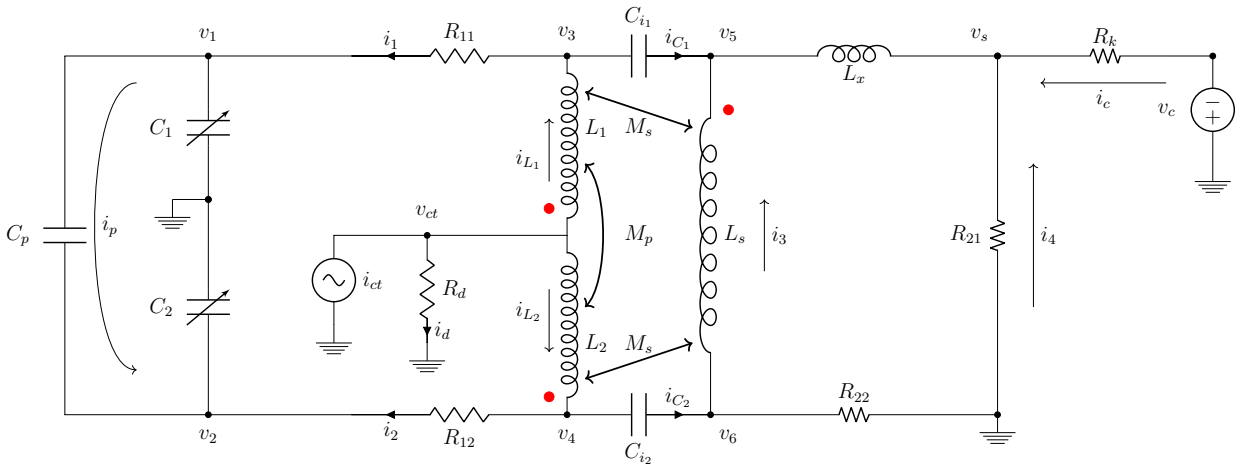

Figure 1.1: Circuit diagram representing the transformer used for detecting gap changes and for applying electrostatic forces to the body.

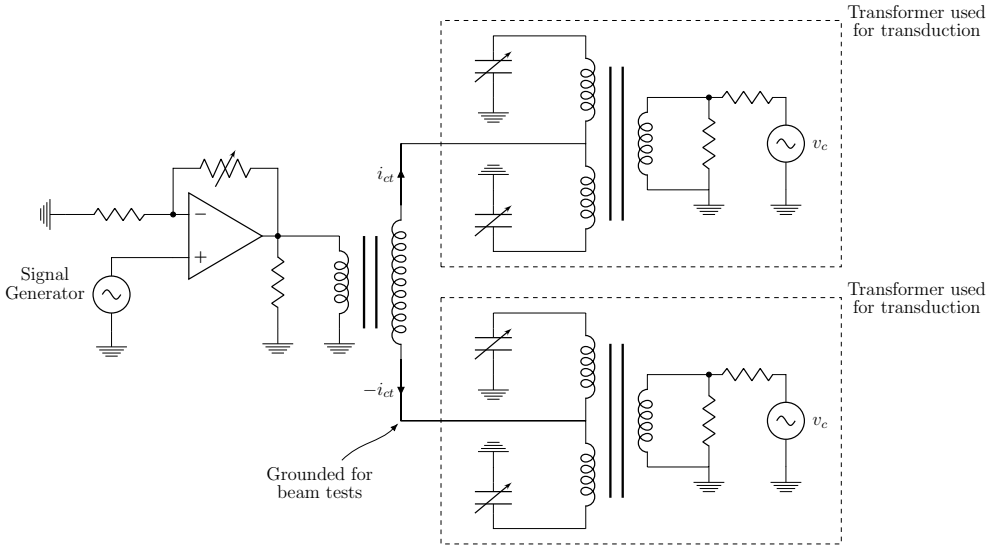

Figure 1.2: Circuit illustrating the supply of current to the transformer(s) performing the transduction.

The center tap is thus a sinusoidal current represented by,

$$i_{\mathrm{ct}}(t) = a_{\mathrm{ct}} \cos\left(2\pi\omega_0 t\right)$$

where a_{ct} is the (constant) amplitude and ω_0 is the carrier frequency. The inductances of the transformer primary windings are large enough so that the nominal inductor-capacitor resonant frequency is smaller than the carrier frequency so, to first order, the center tap

current is evenly split between the primary inductances in a given transformer independent of the capacitances. As such, it is generally assumed that the center tap current always generates nominally equal charges on the electrodes. Similarly, the large inductance on the primary of the auxiliary transformer ensures the current running to the center taps is effectively constant with respect to changes in the input impedance from the perspective of the center tap. Henceforth, the transformers on the right side of Fig. 1.2 will be referred to as "transduction" transformers whereas the transformer on the left will be referred to as the "supply" transformer.

Inclusion of the equipotential body may be included in the analysis by modeling the capacitance between the electrodes and the body. It is important to note here that the electrostatically controlled object must be maintained at ground potential. This can be accomplished by directly grounding the body or by controlling the net charge on the body. The circuit for biasing the transduction transformers in Fig. 1.2 accomplishes the latter. In this configuration, current flowing onto the body through one center tap is pulled off through the "adjacent" center tap. With charge and electric potential developed on the electrodes by the transformer center tap, the gap between the grounded body and electrodes can be modeled as a variable capacitor dependent on the body's orientation (denoted q). As such, an imbalance in the capacitances imposes a voltage drop, $v_{\mathrm{s}}(t) = a_{\mathrm{s}} \cos(\omega_0 t + \phi_y)$, across the secondary load. Thus, v_{s} represents a measurement of the physical gap between the electrode centroid and the projection of this point onto the object. In fact, this design has a natural "null" configuration. When the gaps are equal, and thus the capacitance in-between is as well, no voltage drop is measured on the transduction transformer's secondary. If the body were not grounded, this measurement would be biased in some manner related to the potential on the body. Furthermore, a non-zero net charge on the object would unnecessarily complicate the modeling of the electrostatic forces on the object.

In addition to operating as a displacement transducer, the transformer-electrode arrangement simultaneously provides a means of exerting controlled electrostatic forces on the object. By connecting resistor R_c in series with the transformer secondary, a potential

$v_{\rm c}(t) = a_{\rm c}\cos(\omega_0 t + \phi_u)$ induces a differential potential on each electrode. In other words, the electrode potentials invariably have a 180° phase difference due to the magnetic coupling between the transformer windings. As a result, if the phase of $v_{\rm c}$ is properly chosen, an imbalance in the electrostatic forces applied to the body creates a net moment about the body's center of mass that can be exploited for control of its orientation. In contrast, the $i_{\rm ct}$-induced potentials on both electrodes are in-phase with one another. The superposed effects of $i_{\rm ct}$ and $v_{\rm c}$ are sinusoidal with frequency ω_0 and so the control signal phase ϕ_u is selected so the $v_{\rm c}$-induced component one electrode is in-phase with the $i_{\rm ct}$-induced voltage and therefore the $v_{\rm c}$-induced component of the "adjacent" electrode is 180° out of phase with the $i_{\rm ct}$-induced component. When ϕ_u is chosen in this manner, changing $a_{\rm c}$ produces a differential change in the amplitudes of the sinusoidal potentials on the paired electrodes, and because the electrostatic forces are proportional to the square of the electrode voltages, this creates the largest differential electrostatic force for a given value of $a_{\rm c}$. This circuit configuration, however, creates "feedthrough" from $v_{\rm c}$ to $v_{\rm s}$, because application of $v_{\rm c}$ also develops a voltage drop across the secondary resistor.

Altogether, Fig. 1.1 illustrates the lumped parameter circuit model for the transformer performing the transduction, including various parasitics. The equations relating the currents and potentials in the transformer shown in Fig. 1.1 are

$$\begin{array}{lll}
L_1\dot{i}_{L_1} - M_p\dot{i}_{L_2} - M_s\dot{i}_3 = v_{\rm ct} - v_3 & i_{\rm ct} = i_{L_1} + i_{L_2} + i_d & C_{w_2}\left(\dot{v}_{\rm ct} - \dot{v}_2\right) = i_{w_2} \\
L_2\dot{i}_{L_2} - M_p\dot{i}_{L_1} + M_s\dot{i}_3 = v_{ct} - v_4 & i_c = -(i_3 + i_{C_1}) - i_4 & C_{i_1}\left(\dot{v}_3 - \dot{v}_5\right) = i_{C_1} \\
L_s\dot{i}_3 - M_s\dot{i}_{L_1} + M_s\dot{i}_{L_2} = v_6 - v_5 & i_{L_1} = i_1 + i_{C_1} & C_{i_2}\left(\dot{v}_4 - \dot{v}_6\right) = i_{C_2} \\
L_x(\dot{i}_3 + \dot{i}_{C_1}) = v_5 - v_{\rm s} & i_{L_2} = i_2 + i_{C_2} & v_{\rm ct} - v_{\rm s} = R_k i_c \\
C_1\dot{v}_1 = i_1 - i_p & v_{\rm ct} = R_d i_d & R_{22}(i_{C_2} - i_3) = v_6 \\
C_2\dot{v}_2 = i_2 + i_p & v_{\rm s} = -R_{21} i_4 & C_p\left(\dot{v}_1 - \dot{v}_2\right) = i_p \\
v_3 - v_1 = R_{11} i_1 & v_4 - v_2 = R_{12} i_2 & C_{w_1}\left(\dot{v}_{\rm ct} - \dot{v}_1\right) = i_{w_1}
\end{array} \tag{1.1}$$

where the inductances, resistances and capacitances are given in Table 1.1. Consideration

Transformer Parameters

Parameter	Value	Parameter	Value	Parameter	Value
L_1	2.1 H	C_1	variable	R_{11}	504 Ω
L_2	2.1 H	C_2	variable	R_{12}	504 Ω
L_s	1.53 mH	C_p	17 pF	R_{22}	0.54 Ω
L_x	2.47 μH	C_{i_1}	70 pF	R_{21}	100 Ω
M_p	2.1 H	C_{i_2}	70 pF	R_c	100 Ω
M_s	57.6 mH			R_d	1MΩ

Table 1.1: Table of transformer circuit parameter values as measured by an impedance analyzer.

of the parasitic C_{i_1} and C_{i_2} leads to an asymmetric flow of current in the nominal case when $C_1 = C_2$. Discussion of this asymmetry arises naturally from simulations. The currents and potentials in Eq. 1.1 can be gathered into the vector $w \in \mathbf{R}^{19}$, their ordering being unimportant. By treating v_{c} and i_{ct} at system inputs, analysis of equation Eq. 1.1 leads to a simple state-space formulation of the transformer circuit variables:

$$M(q)\dot{w} = Aw + B_1 i_{\mathrm{ct}} + B_2 v_{\mathrm{c}} \tag{1.2}$$

where $M(q) \in \mathbf{R}^{19\times 19}$ is a "mass" matrix dependent on the body's orientation and the matrices $A \in \mathbf{R}^{19\times 19}$, $B_1 \in \mathbf{R}^{19}$, and $B_2 \in \mathbf{R}^{19}$ represent the system matrix and two input matrices, respectively.

In the following applications to be discussed, the transformer model remains the same. Since the transformer leads are attached to an electrode pair, one simply augments the equations of motion describing the transformer transduction by the number of electrode pairs in the system. In the case to follow, the body is directly grounded and only one electrode pair is used. As such, one of the primary leads in the transformer producing the center tap current is ground as noted in Fig. 1.2.

Part I

Single Degree of Freedom Position Sensor

CHAPTER 2

Unstable "Pathfinder"

The plant for the unstable 1-DOF "pathfinder" is formed by considering a silicon beam that rests and rotates upon a 10 μm high fulcrum patterned on top of a glass substrate. A pair of electrodes are patterned on the glass substrate and symmetrically situated on either side of the fulcrum and below the beam. These electrodes serve to both apply electrostatic forces and provide a means for differential capacitance sensing. Indeed, any potential difference between the electrode and beam generates and electrostatic force which in turn creates a net moment on the beam. Furthermore, the electrodes and surrounding electronics are designed such that zero differential capacitance indicates there are uniform 10 μm gaps between the beam and electrodes (Figs 2.1, 2.3 show schematics of the 1-DOF system). This system has the advantage of presenting no unusual fabrication requirements, and is easy to assemble and test with different electrode configurations.

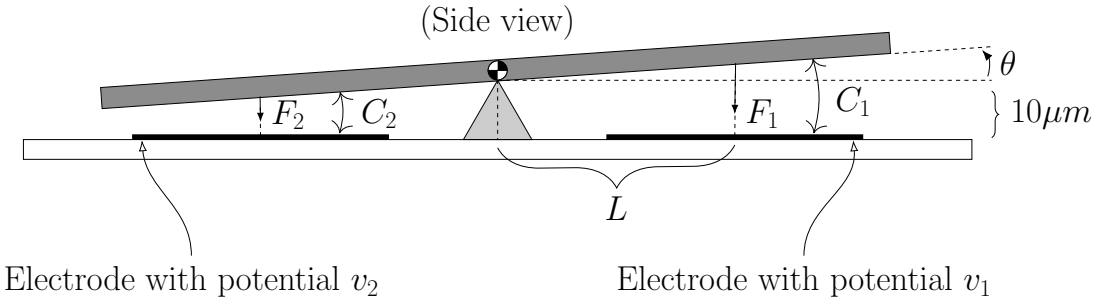

Figure 2.1: Side view of beam in relation to electrodes (not to scale).

The beam-substrate geometry permits only small beam deflection angles so a simple parallel plate capacitor model adequately describes the relation between the capacitance and

the beam-electrode gap. Specifically, this beam-electrode gap is the length of the normal vector that extends from the electrode geometric center to the beam undersurface. Due to the electrode symmetry about the fulcrum, any beam deflection results in a deviation from the nominal 10μm beam-electrode gap by $\pm L\theta$, where L is the moment arm defined from electrodes' geometric center to the fulcrum and θ represents the beam angle referenced to the substrate parallel (see Fig. 2.1).

2.1 Mechanical Fabrication

Curvature of the beam and substrate must be minimized in order to facilitate the creation of a uniform 10 μm gap between the approximately 4 cm $\times$ 2.5 cm beam and the substrate. These tolerances are satisfied by selecting a 1 mm thick glass substrate and a 500 μm thick silicon wafer with minimal bow and warpage measurements. Although the surfaces are flat it is necessary to establish a nominal gap between the substrate and silicon beam. The nominal gap, denoted d_0, is specified by creating a fulcrum on which the beam will rest. The fulcrum is fabricated by first spinning a 10μm thick layer of the epoxy-based photoresist SU-8 onto the glass substrate. SU-8 is selected for its ability to create a well-defined thickness across the wafer by simply adjusting the spin coater parameters. The SU-8 is subsequently patterned, developed, and cured to create a fulcrum that is 10μm in height, 100 μm in width and 30 mm in length. With the fulcrum in place, an image reversal process is conducted to pattern the glass for the electrodes and their wire bonding pads. A 0.5 μm thick layer of gold is evaporated over a 30 nm thick Cr adhesion layer to form the electrodes on the substrate. These steps are shown in Fig. 2.2.

The beam is diced out of a 500 μm thick, single-side polished silicon wafer. A layer of aluminum coats the beam, ensuring excellent conductivity and justifying the modeling of the beam an equipotential body. Lastly, a 500 nm thick layer Parylene-C is deposited onto the beam to increase the dielectric strength of the insulating layer between the beam and the electrodes. This effectively increases the maximum possible potential difference

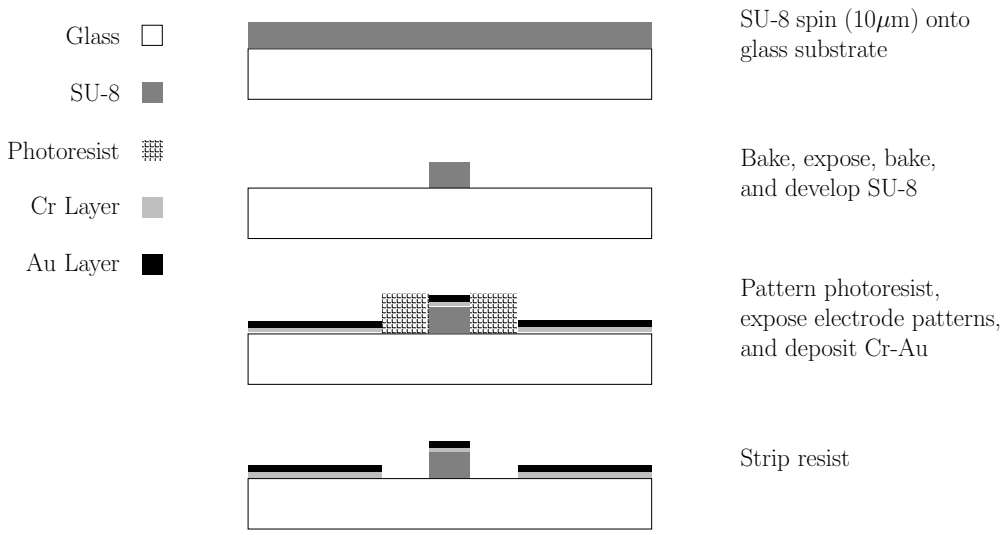

Figure 2.2: Processing steps for glass substrate.

between the electrodes and beam that may be applied before breakdown occurs. The electrodes are accessed via gold wire bond pads situated to the side of the beam. A wire bond is attached directly to the aluminum to maintain the beam at ground potential. Alignment markers on the glass simplify centering the silicon beam on the SU-8 fulcrum. The assembled system is shown in the top figure of Fig. 2.3 where the beam is rendered semi-transparent in order to reveal the electrodes in relation to the fulcrum. The relevant dimensions are given in Table 2.1. The substrate is fabricated with two pairs of electrodes, each pair possessing electrodes on opposite sides of the fulcrum. Only one pair is used in the present work as indicated in Fig. 2.3, however, operation of two pairs would enable maintaining the beam at ground potential without the physical ground used here.

2.2 Model and Analysis of Coupled Plant

The beam and transformer equations are linked because the potentials on the electrodes create electrostatic forces on the beam, and conversely, the beam angle changes the capacitances created between the electrodes and beam (see Fig. 2.3). In this section, analysis of the transformer-beam subsystem is performed. However, the full plant model also in-

Beam Parameters	
Parameter	**Value**
beam length	44 mm
beam width	25 mm
beam thickness	500 μm
electrode area, A	1.21 cm^2
dielectric constant, ϵ	8.85×10^{-12} F $\cdot$ m^{-1}
fulcrum/electrode distance, L	1.55 cm
nominal beam/electrode gap, z_0	10 μm
moment of inertia, J	0.207×10^{-6} kg $\cdot$ m^2

Table 2.1: Table of beam parameter values

cludes a DAC smoothing filter, an anti-alias filter, and a low-pass filter for recovering the baseband signal produced when the filtered v_s voltage is demodulated. The nonlinear equations of motion for the coupled transformer-beam system will be constructed and followed by a linear time variational model for the same system. An augmentation of this system will include the necessary filters to complete the plant model. Experimental results and comparisons to the full plant model will conclude this chapter.

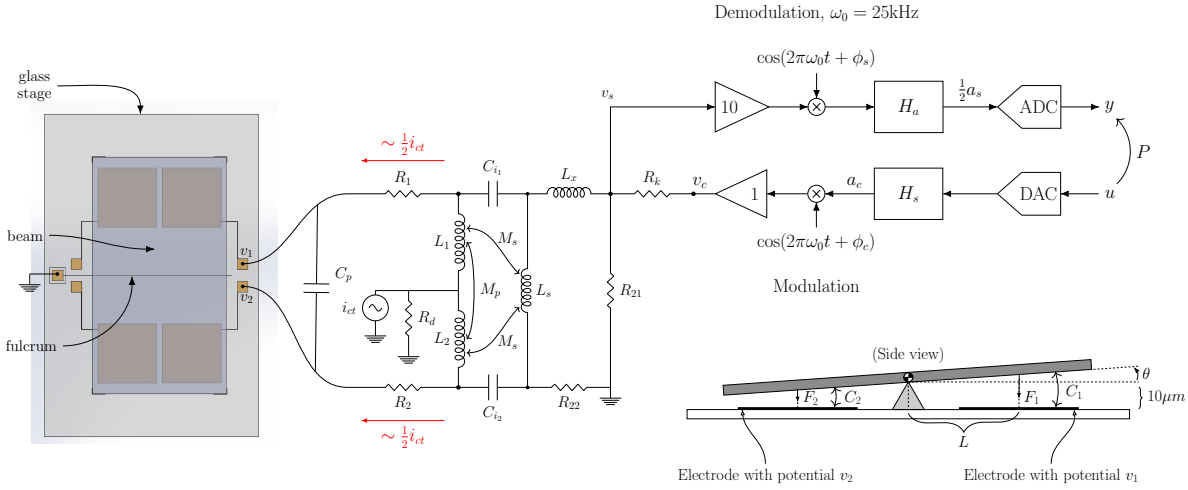

Figure 2.3: Schematic showing substrate, beam, fulcrum and electrodes in relation to the transformer used for differential capacitance transduction and electrostatic forcing.

2.2.1 Full Nonlinear Equations

The beam equations are represented as

$$\frac{d}{dt}\begin{bmatrix}\theta\\ \dot{\theta}\end{bmatrix} = \begin{bmatrix}\dot{\theta}\\ f(\theta; w)\end{bmatrix} \tag{2.1}$$

where w is the vector of circuit variable from Eq. 1.2 and f is the moment applied to the beam normalized by the moment of inertia

$$f(\theta; w) = \frac{L}{J}\left(-\underbrace{\frac{\epsilon A}{2}\frac{v_1^2}{(z_0 + L\theta)^2}}_{F_1} + \underbrace{\frac{\epsilon A}{2}\frac{v_2^2}{(z_0 - L\theta)^2}}_{F_2}\right). \tag{2.2}$$

Note that v_1 and v_2 are elements of the vector w, and F_1 and F_2 represent the electrostatic forces exerted on the beam from their respective electrodes (see Fig. 2.1). The beam moment of inertia is given by J and the area of each electrode is A. The values of the beam parameters are also given in Table 2.1. The transformer capacitances, denoted C_1 and C_2, depend on the beam angle ($\alpha = \theta$) and provides the link from the beam dynamics to the the transformer dynamics,

$$C_1 = \frac{\epsilon A}{z_0 + L\theta}, \quad C_2 = \frac{\epsilon A}{z_0 - L\theta} \tag{2.3}$$

The parallel plate capacitance formula is used for computing these capacitances (and computing the electrostatic forces in Eq. 2.2) even when beam is deflected. The gap for the deflected beam is computed as the product of the distance L from the fulcrum to the electrode centroid with the beam angle θ which is then summed with, or subtracted from, the nominal gap z_0. Since θ is very small even at full deflection it is not necessary to use trigonometric functions to express the gap. Equations 2.2 & 2.3 illustrate the nonlinear behavior of the system and may be inserted into Eq. 1.2 to couple the beam dynamics to the transformer variables.

Consider again the ODE describing the circuit variables in Eq. 1.2,

$$M(q)\dot{w} = Aw + B_1 i_{\text{ct}} + B_2 v_{\text{c}},$$

where, here, $q = \theta$. The transformer circuit equations represent an overdetermined set of equations. A singular value decomposition of $M(0)$ (the "nominal" case when $\theta = 0$) is used to reveal $\text{rank}(M) = 6$ and that this rank calculation is independent of θ. The algebraic constraints of the system of equations is resolved with an SVD. Consider a singular value decomposition of $M(0)$ expressed as

$$M(0) = \underbrace{\begin{bmatrix} U_1 & U_2 \end{bmatrix}}_{U} \begin{bmatrix} \Sigma_1 & 0 \\ 0 & 0 \end{bmatrix} \underbrace{\begin{bmatrix} V_1^T \\ V_2^T \end{bmatrix}}_{V^T} \tag{2.4}$$

where U and V are unitary, $U_1 \in \mathbf{R}^{19\times 6}$, $V_1 \in \mathbf{R}^{19\times 6}$, $\Sigma_1 \in \mathbf{R}^{6\times 6}$ is positive definite, and so forth. Standard results show that $\mathcal{N}(M(0)) = \mathcal{R}(V_2)$. By considering a range of plausible values for θ, $\|M(\theta)V_2\|$ is numerically computed and illustrates the nullspace of M is invariant under a capacitance (equivalently, θ) change. Therefore, $\text{rank}(M)$ is constant with respect to θ and it can be shown analytically that $\text{rank}(M(0)) = 6$. Fundamentally then, there are only 6 states required for describing the evolution of the transformer currents and voltages and the system, as it stands presently, is overdetermined. The following analysis presents a method for reducing the system to the primary states necessary to describe the evolution of the transformer voltages and currents under a specific coordinate transformation.

Under a coordinate transformation defined by $s = V^T w$, the equations of motion become

$$M(\theta) \cdot (Vs) = A(Vs) + B_1 i_{\text{ct}} + B_2 v_{\text{c}}. \tag{2.5}$$

As the nullspace of M is invariant under a capacitance change (as established), we have

$$M(\theta)V = M(\theta)\begin{bmatrix} V_1 & V_2 \end{bmatrix} = \begin{bmatrix} M(\theta)V_1 & 0 \end{bmatrix}$$

Now consider a SVD of the matrix $M(\theta)V_1$

$$M(\theta)V_1 = \underbrace{\begin{bmatrix} \hat{U}_1 & \hat{U}_2 \end{bmatrix}}_{\hat{U}} \begin{bmatrix} \hat{\Sigma} \\ 0 \end{bmatrix} \hat{V}^T \tag{2.6}$$

with $\hat{U} \in \mathbf{R}^{19\times 19}$ and $\hat{V} \in \mathbf{R}^{6\times 6}$ unitary, $\hat{U}_1 \in \mathbf{R}^{19\times 6}$ and $\Sigma \in \mathbf{R}^{6\times 6}$ positive definite. This SVD computation is dependent on the varying θ, an important fact to keep in mind. Returning to Eq. 2.5 and using these previous two results,

$$\begin{aligned} \begin{bmatrix} \hat{\Sigma}\hat{V}^T\dot{s}_1 \\ 0 \cdot \dot{s}_2 \end{bmatrix} &= \hat{U}^T AVs + \hat{U}B_1 i_{\mathrm{ct}} + B_2 v_{\mathrm{c}} \\ &= \begin{bmatrix} \hat{U}_1^T AV_1 & \hat{U}_1^T AV_2 \\ \hat{U}_2^T AV_1 & \hat{U}_2^T AV_2 \end{bmatrix} \begin{bmatrix} s_1 \\ s_2 \end{bmatrix} + \begin{bmatrix} \hat{U}_1^T \\ \hat{U}_2^T \end{bmatrix} B_1 i_{\mathrm{ct}} + \begin{bmatrix} \hat{U}_1^T \\ \hat{U}_2^T \end{bmatrix} B_2 v_{\mathrm{c}} \end{aligned} \tag{2.7}$$

where s_1 and s_2 are partitions of s with appropriate dimension. Equation 2.7 reveals an ODE and set of algebraic constraints corresponding the minimal transformer system:

$$\hat{\Sigma}\hat{V}^T\dot{s}_1 = \hat{U}_1^T AV_1 s_1 + \hat{U}_1^T AV_2 s_2 + \hat{U}_1^T B_1 i_{\mathrm{ct}} + \hat{U}_1^T B_2 v_{\mathrm{c}} \tag{2.8}$$

$$0 = \hat{U}_2^T AV_1 s_1 + \hat{U}_2^T AV_2 s_2 + \hat{U}_2^T B_1 i_{\mathrm{ct}} + \hat{U}_2^T B_2 v_{\mathrm{c}} \tag{2.9}$$

Similar brute-force analysis of the $\hat{U}_2^2 AV_2$ shows the matrix is invertible for the range of θ considered. This allows one to solve the algebraic constraint in Eq. 2.9:

$$s_2 = -\left(\hat{U}_2^2 A V_2\right)^{-1} \hat{U}_2^T \left(A V_1 s_1 + B_1 i_{\mathrm{ct}} + B_2 v_{\mathrm{c}}\right) \tag{2.10}$$

Defining $P = V_2 \left(\hat{U}_2^2 A V_2\right)^{-1} U_2^T \in \mathbf{R}^{19\times 19}$ substituting Eq. 2.10 into Eq. 2.8 yields the nonlinear differential equation for the transformer states,

$$\begin{aligned}
\dot{s}_1 =& \left(\hat{\Sigma}\hat{V}^T\right)^{-1} \Big[\hat{U}_1^T A V_1 s_1 + \hat{U}_1^T A V_2 \left\{ -\left(\hat{U}_2^2 A V_2\right)^{-1} \hat{U}_2^T \left(A V_1 s_1 + \ B_1 i_{\mathrm{ct}} + B_2 v_{\mathrm{c}}\right)\right\} \\
&+ \hat{U}_1^T B_1 i_{\mathrm{ct}} + \hat{U}_1^T B_2 v_{\mathrm{c}}\Big] \\
=& \hat{V}\hat{\Sigma}^{-1}\hat{U}_1^T \Big[A V_1 z_1 - A \underbrace{V_2 \left(\hat{U}_2^2 A V_2\right)^{-1} \hat{U}_2^T}_{P} \left(A V_1 s_1 + B_1 i_{\mathrm{ct}} + B_2 v_{\mathrm{c}}\right) + B_1 i_{\mathrm{ct}} + B_2 v_{\mathrm{c}}\Big] \\
=& \hat{V}\hat{\Sigma}^{-1}\hat{U}_1^T \left(I - AP\right)\left(A V_1 s_1 + B_1 i_{\mathrm{ct}} + B_2 v_{\mathrm{c}}\right)
\end{aligned} \tag{2.11}$$

From the solution of the nonlinear ODE presented in Eq. 2.11, s_1, one simply uses the algebraic constraint in Eq. 2.9 to find s_2 and then the original coordinate transformation $w = Vs$ to find the transformer currents and voltages. Collecting Equations 2.1, 2.2, and 2.11 into a state-space formulation, comprised of s_1, θ, and $\dot{\theta}$, the complete nonlinear differential equations describing the beam-transformer system is given:

$$\begin{aligned}
\dot{s}_1 &= \hat{V}\hat{\Sigma}^{-1}\hat{U}_1^T \left(I - AP\right)\left(A V_1 s_1 + B_1 i_{\mathrm{ct}} + B_2 v_{\mathrm{c}}\right) \\
\frac{d}{dt}\begin{bmatrix}\theta \\ \dot{\theta}\end{bmatrix} &= \begin{bmatrix}\dot{\theta} \\ f(\theta; Vs)\end{bmatrix}
\end{aligned} \tag{2.12}$$

The sinusoidal center tap current, $i_{\mathrm{ct}}(t) = a_{ct}\cos(2\pi\omega_0 t)$, is produced by a current source, where a_{ct} is the amplitude and ω_0 is the carrier frequency. When the beam orientation is $\theta = 0$, the capacitances created between the electrodes and beam are equal in the beam model, i.e. $C_1 = C_2$. In this case i_{ct} establishes steady-state sinusoids for all signals in the transformer as well as a master phase angle against which all steady-state signals are

referenced. The steady-state response of the currents and voltages in the transformer, denoted x_0, are computed from the frequency response of Eq. 1.2 with $v_c = 0$

$$w_0(t) \stackrel{r}{=} \left(j2\pi\omega_0 M(0) - A\right)^{-1} B_1 a_{ct} e^{j2\pi\omega_0 t}. \tag{2.13}$$

Despite the fact that $M(0)$ is not invertible, the matrix $j2\pi\omega_0 M(0) - A$ is invertible for any $\omega_0 \neq 0$. For this steady-state solution the electrode potentials are equal sinusoids, i.e. $v_1(t) = v_2(t)$, and so $f(0; w_0(t)) = 0$ for all t. Thus, x_0 along with $\theta(t) = 0$ and $\dot{\theta}(t) = 0$ represent a periodic solution for the coupled transformer-beam subsystem. The beam is in equilibrium because the net beam moment produced by the electrostatic forces is zero and the beam center of mass is assumed to be located at the fulcrum. The stability of this periodic solution can be studied by analyzing the linear variational equations of Eq. 2.1 and 1.2 –refer to [Hal63] for terminology.

2.2.2 Linear Variational and Time-Periodic Equations

The variational equations can be determined by introducing perturbation variables relative to their steady-state values: $w = w_0 + \delta_q$, $\theta = 0 + \delta_\theta$ and $\dot{\theta} = 0 + \delta_{\dot{\theta}}$. The effect of the control voltage v_c can also be included in the analysis by setting $v_c = 0 + \cos(2\pi\omega_0 t + \phi_{v_c})\delta_{v_c}$. Since i_{ct} and v_c have the same carrier frequency, v_1 and v_2 are sinusoidal with frequency ω_0, however, the i_{ct}-induced components create in-phase potentials on v_1 and v_2, while the v_c-induced components have a 180° phase relationship with each other. The phase of the control signal ϕ_{v_c}, however, is selected so that the v_c-induced component of v_1 is in-phase with the i_{ct}-induced sinusoid and, thus, the v_c-induced component of v_2 is 180° out of phase with the i_{ct}-induced component. Thus, when the center tap current is driving the transformer, changing the v_c amplitude, i.e. δ_{v_c}, will create a *differential* change in the *amplitudes* of v_1 and v_2, and because the electrostatic forces are proportional to the mean-square electrode voltages, this differential change in the amplitudes creates the largest

moment on the beam for a given value of δ_{v_c}.

The mass matrix is continuously differentiable in a neighborhood of $\theta = 0$ and so is represented as $M(\theta) = M(0) + M_\theta \delta_\theta + \cdots$, where $M_\theta := \frac{\partial M}{\partial \theta}|_{\theta=0}$. Substituting these expressions into Eq. 2.1 and 1.2 and retaining only linear terms yields the following variational equations,

$$\begin{aligned} M(0)\dot{\delta}_w &= A\delta_w - M_\theta \dot{w}_0 \delta_\theta + B_2 \cos(2\pi\omega_0 t + \phi_{v_c})\delta_{v_c} \\ \frac{d}{dt}\begin{bmatrix} \delta_\theta \\ \delta_{\dot{\theta}} \end{bmatrix} &= \begin{bmatrix} \delta_{\dot{\theta}} \\ f_\theta \delta_\theta + f_w \delta_w \end{bmatrix} \\ &= \begin{bmatrix} \delta_{\dot{\theta}} \\ \frac{L^2 \epsilon A}{J z_0^3}\left(v_{0,1}^2 + v_{0,2}^2\right)\delta_\theta + \frac{L\epsilon A}{J z_0^2}\left(-v_{0,1}\delta_{v_1} + v_{0,2}\delta_{v_2}\right) \end{bmatrix}, \end{aligned} \tag{2.14}$$

where $f_\theta := \frac{\partial f}{\partial \theta}(0; w_0)$ and $f_q := \nabla_q f(0; w_0)$ are the gradients of f with respect to θ and w evaluated on the periodic solution. These equations are time periodic with period $\tau_p = 1/\omega_0$. The algebraic constraints in Eq. 2.14 must be resolved and is so accomplished with the same coordinate change as before. Consider a singular value decomposition of $M(0)$ as before in Eq. 2.4:

$$M(0) = \underbrace{\begin{bmatrix} U_1 & U_2 \end{bmatrix}}_{U} \begin{bmatrix} \Sigma_1 & 0 \\ 0 & 0 \end{bmatrix} \underbrace{\begin{bmatrix} V_1^T \\ V_2^T \end{bmatrix}}_{V^T}.$$

New perturbation variables are defined according to

$$\delta_w = \begin{bmatrix} V_1 & V_2 \end{bmatrix} \begin{bmatrix} \delta_1 \\ \delta_2 \end{bmatrix}$$

where the dimensions of δ_1 and δ_2 are compatible with the partitioning of V. Substituting this relation into the first expression in Eq. 2.14 yields the differential equation and a set of explicit algebraic constraints,

$$\begin{aligned} \Sigma_1 \dot{\delta}_1 &= U_1^T A V_1 \delta_1 + U_1^T A V_2 \delta_2 - U_1^T M_\theta \dot{w}_0 \delta_\theta + U_1^T B_2 \cos(2\pi\omega_0 t + \phi_{v_c})\delta_{v_c} \\ 0 &= U_2^T A V_1 \delta_1 + U_2^T A V_2 \delta_2 - U_2^T M_\theta \dot{w}_0 \delta_\theta + U_2^T B_2 \cos(2\pi\omega_0 t + \phi_{v_c})\delta_{v_c} \end{aligned}.$$

As before, $U_2^T A V_2$ is invertible so,

$$\delta_2 = -\left(U_2^T A V_2\right)^{-1} U_2^T \left(A V_1 \delta_1 - M_\theta \dot{w}_0 \delta_\theta + B_2 \cos(2\pi\omega_0 t + \phi_{v_c})\delta_{v_c}\right).$$

With $P = V_2 \left(U_2^T A V_2\right)^{-1} U_2^T \in \mathbf{R}^{19\times 19}$ the linear time-periodic differential equations are derived by substituting this result for δ_2 into the ODE above,

$$\begin{aligned}
\dot{\delta}_1 &= \Sigma_1^{-1} U_1^T \left(I - AP\right)\left(A V_1 \delta_1 - M_\theta \dot{w}_0 \delta_\theta + B_2 \cos(2\pi\omega_0 + \phi_{v_c})\delta_{v_c}\right), \\
\dot{\delta}_\theta &= \delta_{\dot{\theta}}, \\
\dot{\delta}_{\dot{\theta}} &= f_\theta \delta_\theta + f_q \left(V_1 \delta_1 + V_2 \delta_2\right) \\
&= \left(f_\theta + f_q P M_\theta \dot{w}_0\right)\delta_\theta + f_q \left(I - PA\right) V_1 \delta_1 - f_q P B_2 \cos(2\pi\omega_0 t + \phi_{v_c})\delta_{v_c}.
\end{aligned}$$

Collecting the variables δ_1, δ_θ and $\delta_{\dot{\theta}}$ into a single 9-element state vector denoted δ, produces the following compact representation of the linear variational equations,

$$\begin{aligned}
\dot{\delta} = \underbrace{\begin{bmatrix} \Sigma_1^{-1} U_1^T \left(I - AP\right) A V_1 & -\Sigma_1^{-1} U_1^T \left(I - AP\right) M_\theta \dot{w}_0 & 0 \\ 0 & 0 & 1 \\ f_x \left(I - PA\right) V_1 & f_\theta + f_x P M_\theta \dot{w}_0 & 0 \end{bmatrix}}_{\tilde{A}(t)} \delta \\
+ \underbrace{\begin{bmatrix} \Sigma_1^{-1} U_1^T \left(I - AP\right) B_2 \cos(2\pi\omega_0 t + \phi_{v_c}) \\ 0 \\ -f_x P B_2 \cos(2\pi\omega_0 t + \phi_{v_c}) \end{bmatrix}}_{\tilde{B}(t)} \delta_{v_c},
\end{aligned} \tag{2.15}$$

where $\tilde{A}$ and $\tilde{B}$ both are time-periodic with period τ_p. Note the lack of dependency on the SVD for a given θ. In fact, this linearization coupled with the fact that the $\mathcal{N}(M)$ is invariant with respect to θ shows we need to only compute a single SVD. This makes the linearized approach significantly more computationally efficient compared to a full, nonlinear simulation.

A simulation of the full, nonlinear set of equations in Eq. 2.12 is compared to the linear, time-periodic variational equations in Fig 2.4. This simulation time record is over the course of $t \in [0, 15\tau_p]$,with a step input occurring at $t = 0.21$ms. In order to compare the results, the solution to Eq 2.15 is added to the periodic solution, $w_0(t)$. Since the system is unstable, these parasitics generate a torque on the beam and cause the gap estimate to grow before an input is applied (right figures). Although the differences are small, the linear model does agree more with the nonlinear model once the capacitances C_{i_1} and C_{i_2} are opened as seen by comparing the bottom figures to the top.

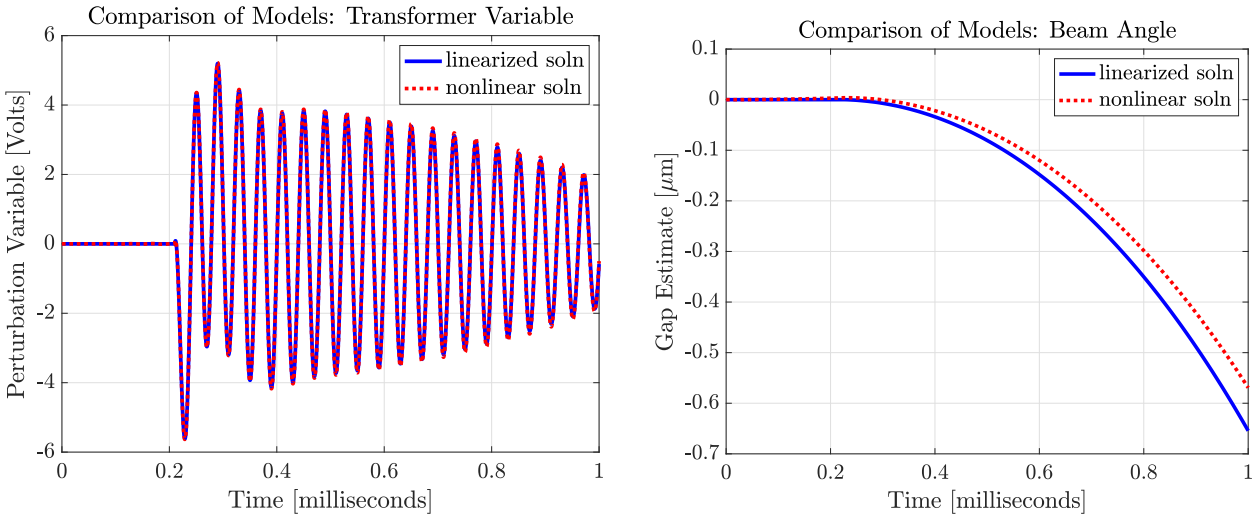

Figure 2.4: Comparison of the nonlinear and linear, variational EOM. Step input for v_c occurs at $t = 0.21$ms.(Left) Comparison of the simulated measurement signal v_s. (Right) Estimates of the gap $L\theta$ as indicated by Fig 2.1

An interesting feature of this system is the existence of two distinct "time-scales". Other than the frequency of operation, one must consider the time-scale under which the evolution of the beam dynamics (and thus its motion) develop. In fact, as to be suggested in the following section, the beam dynamics change at a rate much slower than that of the operation frequency ω_0. This realization allows us to consider the following discrete time approximation model of the linear, time-periodic variational equations.

2.2.3 Discrete Time Approximation

The state transition matrix $\Phi(t, t_0)$ for the periodic system in Eq 2.15 is numerically computed. The characteristic multipliers associated with Eq. 2.15, which are the eigenvalues of $\Phi(\tau_p, 0)$, determine the stability of the periodic solution derived earlier. Although the experimental results are reported in Sec. 2.3, the analysis in this section uses transformer parameter values obtained from tests performed with an impedance analyzer. The beam parameters, on the other hand, are simply estimated from the material properties and dimensions of the beam, electrodes and fulcrum. All parameters are reported in Table. 1.1. Using these parameters, the characteristic multipliers are shown in Fig. 2.5 for the case $\omega_0 = 25\,\text{kHz}$ and $a_{ct} = 4\,\text{mA}$. The period is $\tau_p = 1/\omega_0$. There is one unstable eigenvalue and one eigenvalue equal to 1. The eigenvalue at 1 corresponds to an integrator in the transformer. In fact, A in Eq. 1.2 has one eigenvalue equal to 0 which produces the characteristic multiplier equal to 1 in this analysis. The integrator corresponds to a non-zero charge which can exist in the system even when $i_{\text{ct}} = 0$ and $v_{\text{c}} = 0$. The charge creates constant potentials $v_1 = v_2 = v_3 = v_4 = v_{ct}$, with all other potentials and currents being zero. This mode can be ignored, however, because the current source suppling i_{ct} controls this charge and, furthermore, any parasitic resistance between the center tap and ground, which exists in practice, will drain off any DC charge and thereby perturb this characteristic multiplier to lie slightly inside the unit circle. The resistor R_d is placed into the circuit model (c.f. Fig. 1.1) to represent this current sink. When deriving a transfer function model, it will be shown that the integrator is practically uncontrollable from v_{c} and hence a zero will be located at 1. Of greater interest are the pair of real characteristic multipliers located near 1. Their continuous-time representation corresponds to real poles located at approximately $\pm 207\,\text{Hz}$. The beam dynamics in the absence of the electrode potentials is a double integrator so "connecting" the beam to the transformer with the specified center tap current bifurcates the poles to $\pm 207\,\text{Hz}$. Thus, wide bandwidth control is required to stabilize the system.

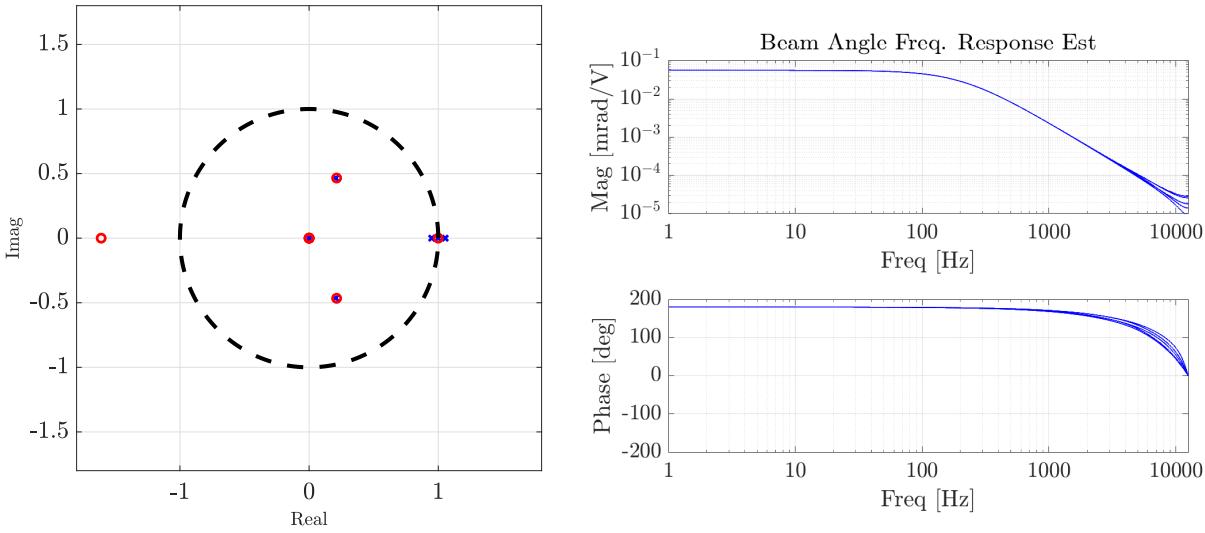

Figure 2.5: (Left) Characteristic multipliers of transformer-beam subsystem ($\times$) and zeros of the approximate transfer function ($\circ$) associated with the measurement of θ for $t_0 = 0$. (Right) Approximate transfer functions with beam angle θ output for $t_0/\tau_p = 0, 0.1, 0.2, \ldots, 0.8, 0.9$.

The loop shaping controller design in Sec. 2.3.1 requires frequency response plots from the control input to the pick-off signal. The full system dynamics are addressed later but the approach for deriving an approximate frequency response function is first demonstrated using Eq. 2.15. However, since Eq. 2.15 is time-varying, a frequency response function does not exist for this system in a strict sense. Nevertheless, the beam dynamics evolve on a slower time scale than the transformer states as suggested by the poles at $\pm 207\,\text{Hz}$ compared to the carrier frequency of $\omega_0 = 25\,\text{kHz}$ for the transformer currents and potentials. The solution to an initial value problem for Eq. 2.15 is

$$\delta(t) = \Phi(t, t_0)\delta(t_0) + \int_{t_0}^{t} \Phi(t, \tau)\tilde{B}(\tau)\delta_{v_c}(\tau)d\tau, \quad t \geq t_0,$$

where $\delta(t_0)$ is the initial condition represented in the perturbation variables and δ_{v_c} is the control voltage input. An approximate time-invariant system can be derived by assuming the control variable is slowly varying over one period of the carrier frequency. Under this

assumption, δ_{v_c} is pulled out of the integral so the state can be estimated one period later,

$$\delta(\tau_p + t_0) \approx \Phi(\tau_p + t_0, t_0)\delta(t_0) + \left(\int_{t_0}^{\tau_p + t_0} \Phi(\tau_p + t_0, \tau)\tilde{B}(\tau)d\tau \right) \delta_{v_c}(t_0).$$

Thus, the evolution of the states can be approximated by a discrete time equation

$$\delta[k+1] = \Phi\delta[k] + \Gamma\delta_{v_c}[k], \tag{2.16}$$

where

$$\Phi := \Phi(\tau_p + t_0, t_0), \quad \Gamma := \int_{t_0}^{\tau_p + t_0} \Phi(\tau_p + t_0, \tau)\tilde{B}(\tau)d\tau.$$

The notation $\delta[k]$ refers to the value of the state δ at the kth sample instant. Note that the sample instants are defined as integer multiples of τ_p relative to t_0. Thus, the approximate models are developed for different phases of the "master" reference signal $\cos(2\pi\omega_0 t)$. Figure 2.6 compares the three time domain models discussed thus far. In simulation shown, $t_0 = 0$ and the parasitic interwinding capacitances are removed.

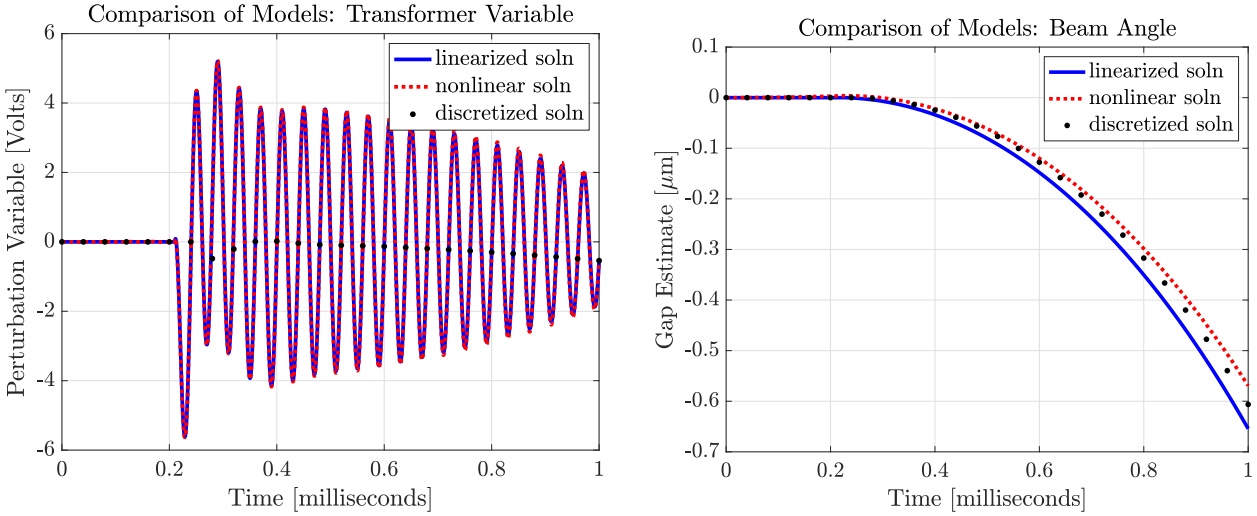

Figure 2.6: Time domain comparison of the models discussed. Step input for v_c occurs at $t = 0.21$ms. (Left) Comparison of the simulated measurement signal v_s. (Right) Estimates of the gap $L\theta$ as indicated by Fig 2.1

Although Φ and Γ depend on t_0 (which may be restricted to the interval $[0, \tau_p)$ without loss of generality) the eigenvalues of Φ are independent of t_0, thus, the poles of the

discrete-time system are the characteristic multipliers of the linear variational equations. The zeros, on the other hand, are dependent on the choice of t_0, however, their effect is most easily understood by comparing the frequency responses of the discrete-time systems obtained at different values of t_0 –this comparison is made in Figure 2.5 for a handful of t_0 when the output variable is selected as θ. The Nyquist frequency associated with these discrete-time models is 12.5 kHz so the frequency responses are computed up to this limit. The family of frequency responses demonstrates that the t_0 parameter only has an effect on the high-frequency aspects of the discrete-time models and for this reason the nominal model when $t_0 = 0$ will be used for the controller design. The pole-zero plot in Fig. 2.5 also shows that the mode with characteristic multiplier equal to 1 is cancelled by a zero. Further analysis of Φ and Γ confirms that this mode is uncontrollable from δ_{v_c}.

2.2.4 Electrical Measurement of Beam Orientation

The key aspects of the system have been analyzed in Sec. 2.2, however, the beam angle θ is not directly measured but instead inferred from measurements of v_s. Indeed, the transformer is configured as a differential capacitance transducer in which a change in the beam angle induces a differential change in the nominal electrode capacitances which in turn produces an amplitude modulated sinusoid with frequency ω_0 at v_s. Thus, a component missing from the analysis in Sec. 2.2 is the demodulation process for recovering the amplitude of v_s. Furthermore, the DSP controller implementation requires the insertion of a DAC analog smoothing filter and an anti-alias filter – the block diagram of the full plant model is shown in Fig. 2.7. The analysis method introduced in Sec. 2.2.2 can be applied here, too, because there also exists a periodic solution with $\theta(t) = 0$ and $\dot{\theta}(t) = 0$ about which linear variational equations can be developed. The DAC conversion process can be ignored in the analysis because the assumption of slow variation in u essentially introduces zero-order-hold dynamics into the discrete-time equations derived from the linear variational equations. Similarly, the band-limiting nature of the anti-alias filter ensures the spectrum of its analog output is equal to that of the sampled signal produced by the ADC.

Computing the models, though, requires specification of the modulation/demodulation phases ϕ_u and ϕ_y shown in Fig. 2.7. As described in Sec. 2.2.2, ϕ_u is specified so that v_c (generated by mixing u and $\cos(2\pi\omega_0 t + \phi_u)$ and filtering) produces amplitude modulated sinusoids at the electrodes that possess 0° or 180° phases with respect to the sinusoids produced by i_ct. Similarly, the demodulation phase ϕ_y is chosen so that the amplitude modulated voltage created at v_s due to $\theta \neq 0$ is in-phase with $\cos(2\pi\omega_0 t + \phi_y)$. This choice maximizes y, the sampled, demodulated v_s signal, for a given angle θ.

The full plant model is a 20-state system: 8 states are contributed by the coupled transformer-beam subsystem, 8 states are each contributed by the analog anti-alias filter, and 4 states are present in the DAC smoothing filter. The dynamics of the Butterworth filters H_s and H_a are respectively modeled by the linear systems $(A_s, B_s, C_s, 0)$ and $(A_a, B_a, C_a, 0)$ with the state vectors $\delta_s \in \mathbf{R}^4$ and $\delta_a \in \mathbf{R}^8$, the vector length corresponding to the order of the filter. Furthermore, the output of the smoothing filter is the amplitude of v_c and with respect to the control voltage perturbation, $\delta_{v_\mathrm{c}} = C_s\delta_s$. These filter states are decoupled from those governing the transformer-beam system and, consequently, are invariant to the coordinate transformation set forth by the SVD of $M(0)$. The linear time-periodic differential equations are augmented to

$$\begin{aligned}
\dot{\delta}_s &= A_s\delta_s + B_s u \\
\dot{\delta}_1 &= \Sigma_1^{-1}U_1^T\left(I - AP\right)\big[AV_1\delta_1 - M_\theta\dot{w}_0\delta_\theta \\
&\qquad + B_2\cos(2\pi\omega_0 t + \phi_u)C_s\delta_s\big], \\
\dot{\delta}_\theta &= \delta_{\dot{\theta}}, \\
\dot{\delta}_{\dot{\theta}} &= \left(f_\theta + f_x P M_\theta\dot{w}_0\right)\delta_\theta + f_x\left(I - PA\right)V_1\delta_1 \\
&\qquad - f_x P B_2\cos(2\pi\omega_0 t + \phi_u)C_s\delta_s \\
\dot{\delta}_a &= A_a\delta_a + B_a v_\mathrm{s}\cos(2\pi\omega_0 t + \phi_y) \\
y &= C_a\delta_a.
\end{aligned} \tag{2.17}$$

Note that v_s in the δ_a ODE can be expressed in terms of δ_1. These equations are consoli-

dated into the 20-state system in Eq. 2.15 via the state vector

$$\delta = [\delta_s,\ \delta_1,\ \delta_\theta,\ \delta_{\dot{\theta}},\ \delta_a]^T\,,$$

the input u, and forming $A_\delta(t)$, $B_\delta(t)$, and C_δ accordingly. Following this augmentation, the discrete time approximation of this linear, time-periodic variational system of equations is executed in the same manner presented in Sec.2.2.3.

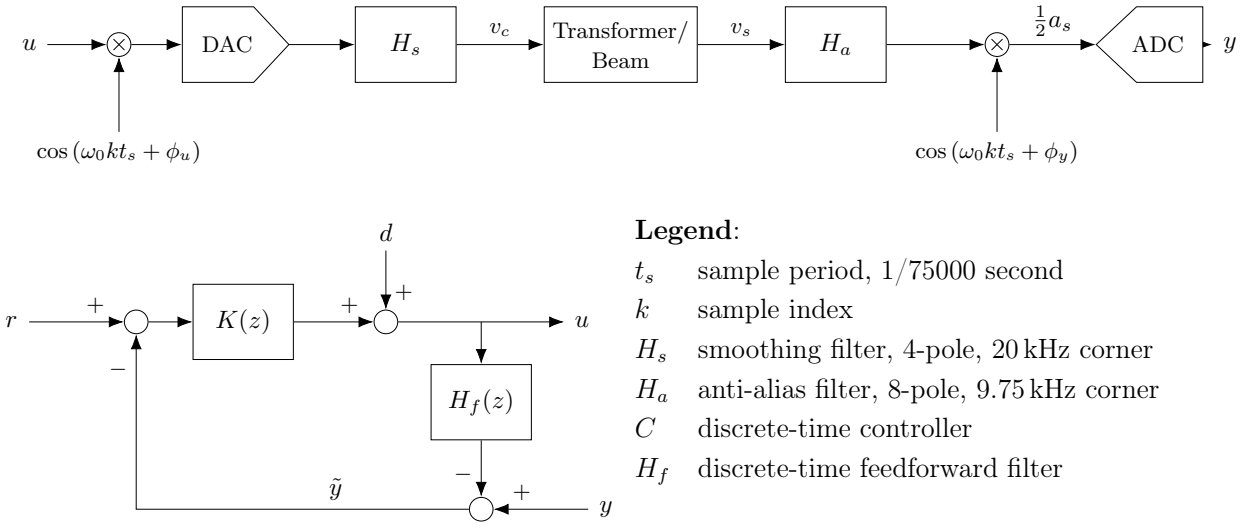

Figure 2.7: Block diagram of plant, controller and feedforward filter.

The characteristic multipliers, estimated zeros (for $t_0 = 0$), and transfer functions y/u are shown in Fig. 2.8 for the case $i_{\rm ct} = a_{ct}\cos(2\pi\omega_0 t)$, where $a_{ct} = 4\,\text{mA}$ and $\omega_0 = 25\,\text{kHz}$. One notable feature in the frequency response is the presence of a flat pass-band above 1 kHz due to the coupling of $v_{\rm c}$ to $v_{\rm s}$. This feedthrough coupling obscures the beam response at higher frequencies and biases the measurement of the beam deflection at low frequencies. It is also the source of the zeros near 1 in Fig. 2.8. Note that the unstable near pole-zero cancellation has implications for the achievable minimum peak sensitivity function [DFT91]. Fortunately, the feedthrough can be identified and mitigated with an appropriate feedforward filter as described in Sec. 2.3. For the model, however, the feedthrough can be determined from the full plant by constraining $\theta(t) = 0$ which removes the beam

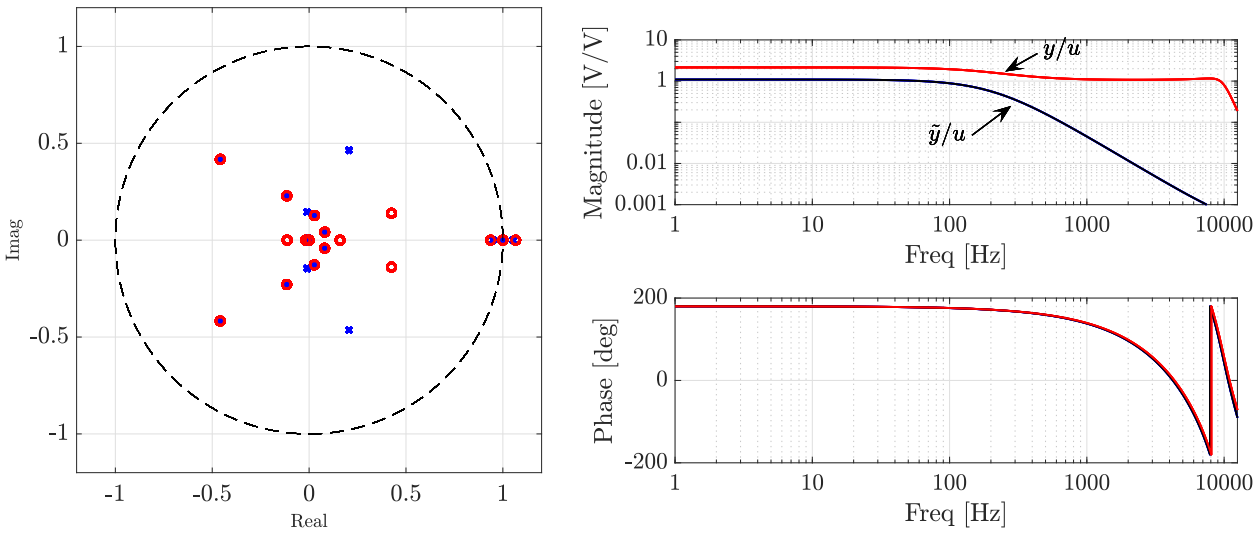

Figure 2.8: (Left) Poles, displayed as $\times$, and zeros, displayed as $\circ$, for the 20-state discrete-time plant in Fig. 2.7. The zeros are computed for $t_0 = 0$. (Right) Frequency responses of discrete-time models y/u, $\tilde{y}/u$ and the feedthrough when $t_0 = 0$. The "sample rate" for the models is the frequency ω_0.

dynamics from the analysis. The feedthrough frequency response is also shown in Fig. 2.8 along with the frequency response $\tilde{y}/u$ which reveals the anticipated -40db/decade roll-off, cf. Fig. 2.5. The additional filtering, however, also adds significant phase lag in the region where the loop gain is likely to cross over. The model also yields a scale factor that converts y into an equivalent gap change at the center of the electrodes (assuming parallel plate models for C_1 and C_2). The scale factor is estimated to be $10.9\,\mu$m/V. The corresponding scale factor for converting y into the beam angle is $0.706\,$mrad/V.

2.3 Experimental results and discussion

The beam and glass substrate are placed in a vacuum chamber which typically pumps down to less than $10\,\mu$Torr because when the beam is operated in air, the squeeze film damping between it and the substrate vastly attenuates the response of the beam above 1 Hz. Thus, high-bandwidth control of the beam angle and beam-electrode gap is only possible *in vacuo*. In fact, the beam equations ignore all damping and are only appropriate for

describing the beam in a vacuum. In any case, a levitated resonator would be operated in a high vacuum, too. The transformer, on the other hand, is located outside of the vacuum chamber and is interfaced to a DSP operating at a 75 kHz sample rate. The DSP generates the $\omega_0 = 25\,\text{kHz}$ reference sinusoid for the center tap current i_{ct} and modulated signal that specifies v_{c}. It is clear why the smoothing filter is required since there are only three samples in one period of the carrier sinusoids. Furthermore, the Nyquist frequency is only 12.5 kHz away from ω_0 so this determines the corner frequency of the anti-alias filter in Fig. 2.7.

2.3.1 Stabilized system

Based on the θ-output transfer function in Fig. 2.5, constant gain feedback of sufficient magnitude will stabilize the system, but because v_s, not θ, is used for feedback, feedthrough coupling is an impediment to stabilization due to its high gain at frequencies well beyond those at which the beam responds. Thus, the severity of the feedthrough must be reduced. This was accomplished in [Atk67, AB75] through the use of a "model transformer", which is an analog implementation of a feedforward cancellation filter. The model transformer, as the name suggests, requires additional hardware so the alternative approach used in this work employs a discrete-time feedforward cancellation filter, denoted H_f, that is implemented in the DSP as shown in Fig. 2.7. Although models of the feedthrough dynamics are available, the feedthrough is experimentally identified in practice because it produces much better matching. The beam is not perfectly balanced so in the absence of stabilizing feedback control it tilts to one side with one end resting on the glass substrate. With no applied center tap current, u produces a small disturbance torque that will not move the beam from its rest position. Thus, the resulting y signal is almost entirely produced by the feedthrough coupling. This permits the identification of an appropriate model of the feedthrough. A 6-state discrete-time model of the feedthrough is implemented as H_f in Fig. 2.7 and is effective in reducing the feedthrough by about an order of magnitude. The beam is modeled as a rigid structure, however, there are flexural modes that can be ex-

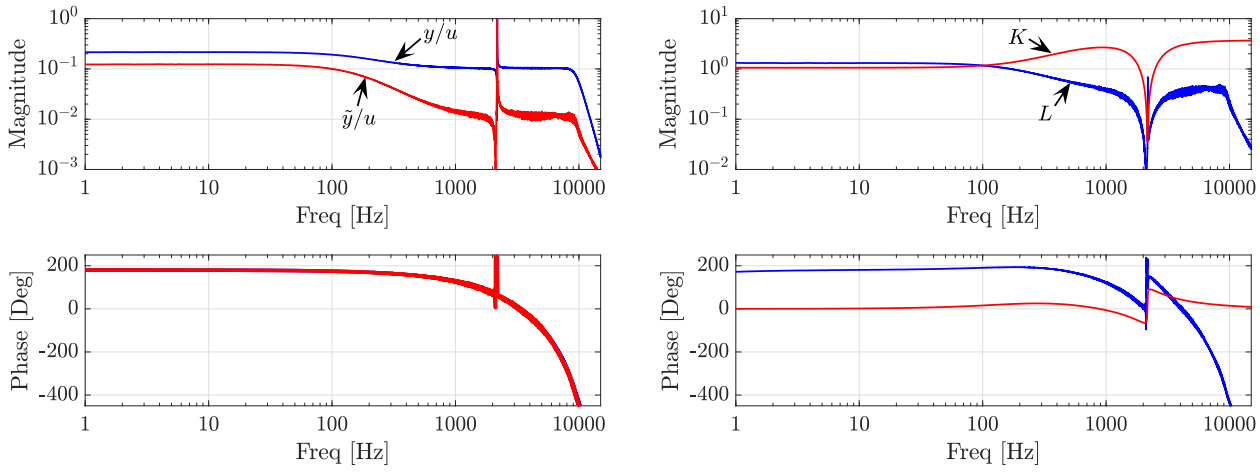

Figure 2.9: (Left) Open-loop empirical plant frequency responses extracted from closed-loop data. (Right) Empirical loop gain L and analytical controller frequency response (the controller magnitude is $10\times$ that shown).

cited and measured by the electrical interface, but since these modes tend to be somewhat symmetric about the fulcrum in mode shape, the differential sensing and forcing tends to weakly excite/sense these modes. Nevertheless, the presence of flexural modes creates a potential source of instability for any controller design since the flexural mode damping is extremely low in the vacuum.

The primary control design objective is stabilization of the unstable plant, and the analytical models developed in Sec. 2.2.4 are useful for guiding the initial design process. Classical loop shaping controller design is effective since the system is single-input/single-output. The plant has one unstable pole so the loop gain must have one net counter-clockwise encirclement of $-1+j0$ in the Nyquist plot. This is achieved with a mild phase-lead filter, however, a notch is also required to reduce the magnitude of a flexural mode that exists when the beam is balanced on the fulcrum. Once the experimental system is stabilized it is possible to identify improved models by testing the closed-loop system. The empirical open-loop plant frequency response is shown in Fig. 2.9. Both the y/u and $\tilde{y}/u$ frequency responses have excellent agreement with the analytical model frequency responses in Fig. 2.8. The feedthrough filter H_f cannot be expected to provide the degree of feedthrough cancellation at high frequencies as in the case of the analytical model and, indeed, an order of

magnitude reduction in the feedthrough appears to be practical as shown in Fig. 2.9 (compare the relative magnitudes at high frequencies). The closed-loop frequency responses are deduced from testing the asymptotically stable closed-loop system by injecting a broadband signal where d enters the loop and then computing the cross-spectra between d all signals of interest. Open-loop frequency responses are then algebraically computed from the closed-loop frequency responses.

The presence of the residual feedthrough limits the amount of phase lead that can be added to the loop by the controller because the low frequency gain of the loop must be large enough to achieve the requisite encirclement for closed-loop stability. Also note that a notch filter is required to reduce the gain of the flexural mode near 2 kHz. An integrator is also present in the controller but its closed-loop time constant is approximately 1 second. The frequency response of the controller is shown in Fig. 2.9 along with the empirically measured loop gain. The cross-over frequency is approximately 150 Hz. The Nyquist plot of the experimentally measured loop gain is shown in Fig. 2.10 and gives more insight into the achievable stability margin. Given the limits on the high-frequency gain in the controller, the phase lead cannot reduce the sensitivity function magnitude over a large frequency band. In fact, the residual feedthrough coupled with the significant phase lag introduced by the analog filtering, creates a scenario in which large sensitivity magnitude is unavoidable over a significant frequency interval as shown in Fig. 2.10. Nevertheless, based on the complementary sensitivity T, the beam can track reference commands up to 600 Hz. The disturbance rejection properties of the controller, however, do suffer from the relatively large sensitivity.

Careful contrast of the empirical frequency responses in Fig. 2.9 to the analytical model frequency responses in Fig. 2.8 show differences in the overall magnitudes by roughly a factor of two. This difference can be attributed to how the lumped circuit parameters of the analytical model are measured and modeled. Specifically, the numerical value of the parasitic winding-to-winding capacitance, C_{w_1} and C_{w_2}, substantially effect the model frequency response magnitude and adjusting these values can show improved agreement

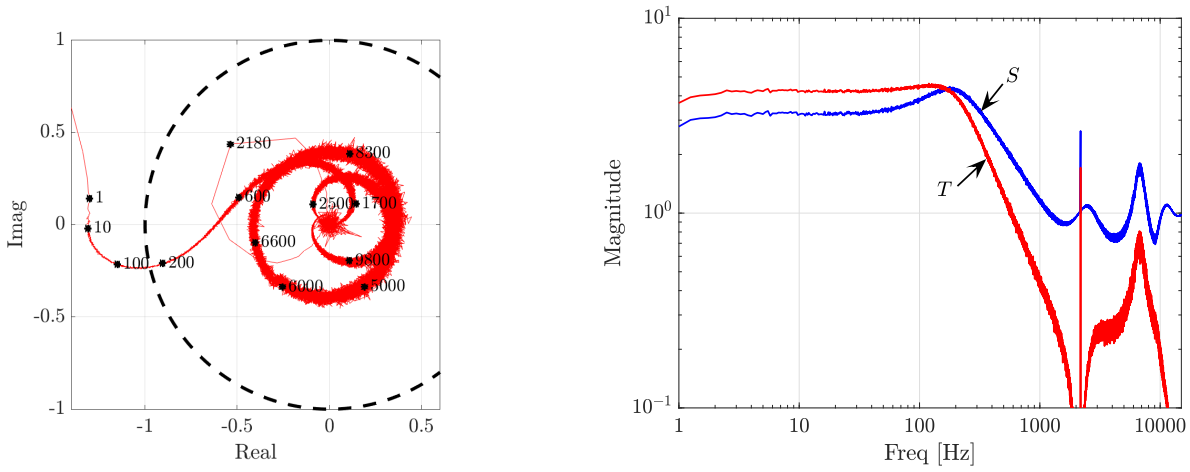

Figure 2.10: (Left) Nyquist plot of loop gain. (Right) Sensitivity function and complementary sensitivity function magnitudes.

between the two frequency responses.

2.3.2 Pick-off calibration and displacement noise spectrum

The voltage measurement of the beam displacement is calibrated with a laser vibrometer by placing the vibrometer spot at the center of an electrode. The vibrometer measures the velocity normal to the beam so the closed-loop frequency response from d to the vibrometer output provides a direct measurement of the time-rate-of-change of the beam-electrode gap at the electrode center. This frequency response is "integrated" into an equivalent displacement as a function of the voltage d as shown in Fig. 2.11. This is compared to the closed-loop frequency response from d to the electrical pick-off measurement of the beam displacement, i.e. $\tilde{y}/d$. As the input associated with both frequency responses is the same, the low-frequency ratio of the frequency response magnitudes provides the "scale factor" associated with the electrical pick-off. This scale factor is approximately 11.5 μm/V and is nearly equal to the value derived from the model and reported in Sec. 2.2.4. This conversion factor is accurate from DC to approximately 200 Hz, but beyond 200 Hz, the vibrometer frequency response must be normalized by the electrical pick-off frequency response, $\tilde{y}/d$. Despite the deviation from a simple gain conversion at higher frequencies,

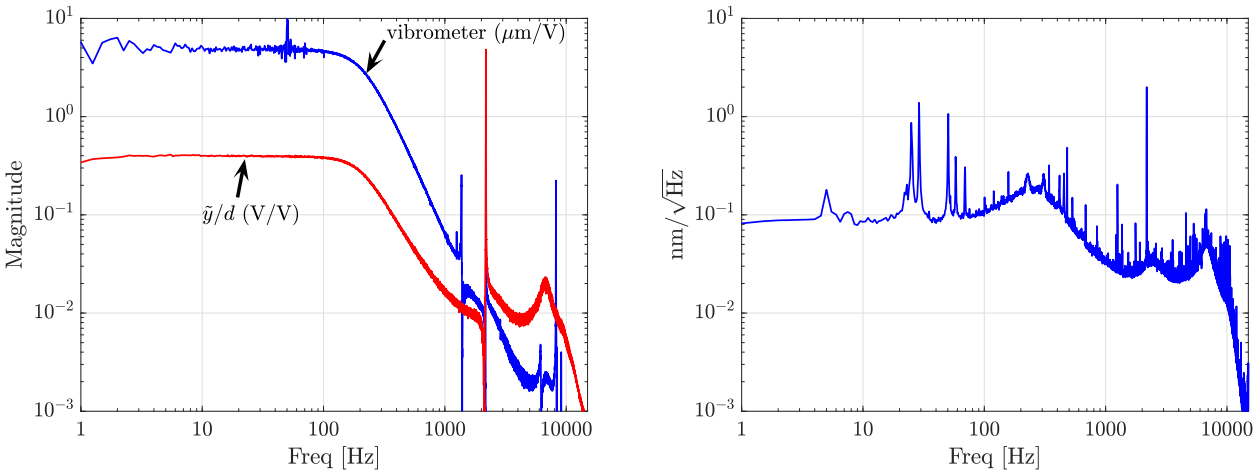

Figure 2.11: (Left) Vibrometer measurements for calibrating electrical pick-off. (Right) Displacement noise spectrum of $\tilde{y}$ using scale factor obtained from the vibrometer data.

the voltage noise spectrum of $\tilde{y}$ can be scaled into an equivalent displacement noise spectrum that will be accurate for frequencies below 200 Hz. The voltage noise spectrum of $\tilde{y}$ is measured when $d = 0$, however, as the feedback loop is closed, any electrical noise will be shaped by the sensitivity function. Furthermore, any mechanical disturbances to the beam, i.e. vibration transmitted through the vacuum chamber to the beam by pumps, floor motion, etc., will also be included in the noise spectrum. The measured spectral density is shown in Fig. 2.11 and reveals that the RMS displacement noise from DC to 100 Hz is approximately 7 nm. The largest contributions appear to be from line noise near 50-60 Hz, and subharmonics. Discounting these components reveals a noise floor near 0.1 nm/$\sqrt{\text{Hz}}$. Thus, the beam motion can be measured with a high precision over broad frequency band.

There are other interesting features in the vibrometer data. For example, the lightly damped flexural mode near 2 kHz is evident in the frequency and the noise spectrum, thus, as noted above, the displacement noise spectrum also includes acceleration disturbances to the beam in addition to electrical noise. The vibrometer also appears to detect additional flexural modes near 1.3 kHz and 9 kHz which are not detected by the electrical pick-off. This is of interest because the pick-off and forcing is collocated at the same electrode and so it should be possible to excite a flexural mode if only it can be sensed; the nature of these flexural modes and why they are excited but not sensed has not been resolved.

CHAPTER 3

Bootstrap Feedforward Compensation

The use of the electrode pair as both a capacitive pick-off and an electrostatic forcer naturally produces significant 'feedthrough' of the control signal into the measurement related to the beam angle. The appearance of the feedthrough was seen previously in Fig. 2.8. It is necessary to reduce the severity of the feedthrough for two reasons. First, an accurate indication of the beam pose is not possible if the feedthrough of the control signal is left uncompensated. Indeed, the frequency response of the feedthrough in Fig. 2.8 has approximately the same magnitude as the beam motional frequency response at low frequencies. Second, the beam-electrical interface forms an unstable system so feedback is necessary to stabilize the beam at a desired angle. If left uncompensated, the feedthrough prevents the development of adequate phase lead necessary for stabilizing the system. Thus, if the feedthrough is not cancelled to some degree, the system is not practically stabilizable. In the previous chapter, a feedforward filter identified from open-loop measurements reduced the feedthrough by about an order of magnitude (cf. Fig. 2.9). This level of reduction was adequate for implementing a stabilizing controller, however, the associated stability margins were quite low. Fig. 2.10 showed the magnitudes of the sensitivity and complementary sensitivity functions to be about 3–4 from DC to 300 Hz. Such high sensitivity is undesirable as it causes amplification of disturbances and noise over a broad frequency band. In order to reduce the closed-loop system's sensitivity, improved matching between the feedforward filter and feedthrough dynamics is necessary. Toward this end, the feedforward filter based on open-loop measurements is updated in closed-loop to account for subtle changes in the feedthrough due to stabilizing the beam about a different position

compared to the open-loop measurements. The relatively large gain of the controller in a neighborhood of the cross-over frequency requires the feedthrough be effectively cancelled in this region. Thus, an initial estimate of the feedthrough must be obtained prior to stabilizing the beam. Better matching between the feedforward filter and the actual feedthrough dynamics allows more phase lead within the controller since greater suppression of the feedthrough is achieved. Since an improved model of the feedthrough can only be determined from closed-loop tests after the initial stabilization of the beam, the procedure is referred to as bootstrap feedforward compensation. Fig. 3.1 provides a block diagram representation of the closed-loop system including the bootstrap feedforward filter and the measurements used to model the feedthrough in closed-loop

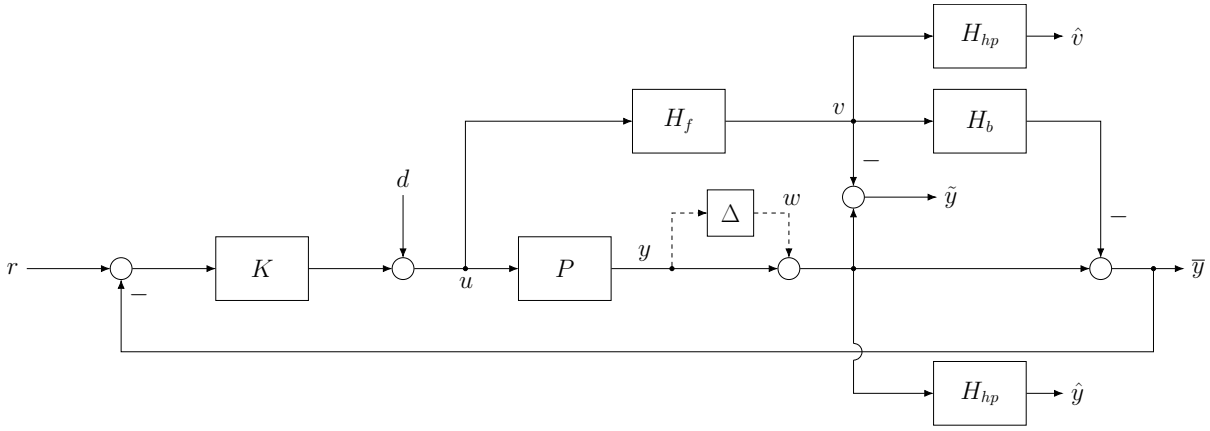

Figure 3.1: Block diagram of the closed-loop system including the feedforward compensation.

3.1 Initial feedforward filter

The initial feedforward filter is attained from open-loop feedthrough measurements. In open-loop, the beam rests at its maximum deflection angle on the fulcrum with one edge in contact with the glass substrate. An estimate of the feedthrough is simply determined by correlating y with u when the u is a white stationary sequence (constant power spectral density from DC to the Nyquist frequency). A lower threshold of the moment created by the electrostatic forces must be exceeded to lift the beam edge that rests on the substrate,

thus, the amplitude of the plant input u is limited so as to not induce beam motion. Furthermore, the controller is zero for this test, i.e. $K = 0$ in Fig. 3.1, so the test input is supplied by the signal d which is injected at the plant input ($u = d$ in open-loop). Consequently, measurement of the transfer function y/u represents the feedthrough due to the transformer dynamics established by the specific electrode capacitances created by the beam in this resting pose.

The feedforward filter is simply specified to be first 60 terms of the empirical impulse response derived from the aforementioned test. In other words, the feedforward filter is implemented as a finite impulse response (FIR) filter. The time-domain representation of the filter is denoted h_f and H_f denotes its corresponding frequency response. Fig. 3.2 shows the filter taps. The FIR form of the feedforward filter provided superior cancellation compared to other filter realizations. In fact, the efficacy of the filter in cancelling the feedthrough is evident in Fig. 3.3 which shows the empirical frequency responses obtained via open-loop testing of the system. The graph labeled y/u is simply the feedthrough existing in the system with the beam at its rest pose, and the graph labeled $\tilde{y}/u$ represents the *compensated* plant output with feedthrough "cancelled" by the feedforward filter h_f (also refer to Fig. 3.1). Fig. 3.3 demonstrates that feedthrough in the compensated output has been suppressed by a factor of 100 from DC to 10 kHz, and even above 10 kHz the suppression is at least a factor of 20. These results, however, are achieved in the open-loop system.

Stabilizing the beam about a reference angle with a feedback controller is only achievable with the initial feedforward filter h_f in place. With respect to the block diagram in Fig. 3.1, the signal $\overline{y}$ is used for feedback, however, since $H_b = 1$ at this point, $\overline{y} = \tilde{y}$ when the beam is initially stabilized. The controller for this task is indicated as K_1 in Fig. 3.4. It is indeed a phase-lead filter with a notch filter near 2 kHz. The notch filter was added to compensate a lightly damped beam flexural mode that is present when the beam is balanced on the fulcrum. Although it is clear that K_1 provides some phase lead, it is relatively weak because the magnitude of K_1 is limited at frequencies greater than

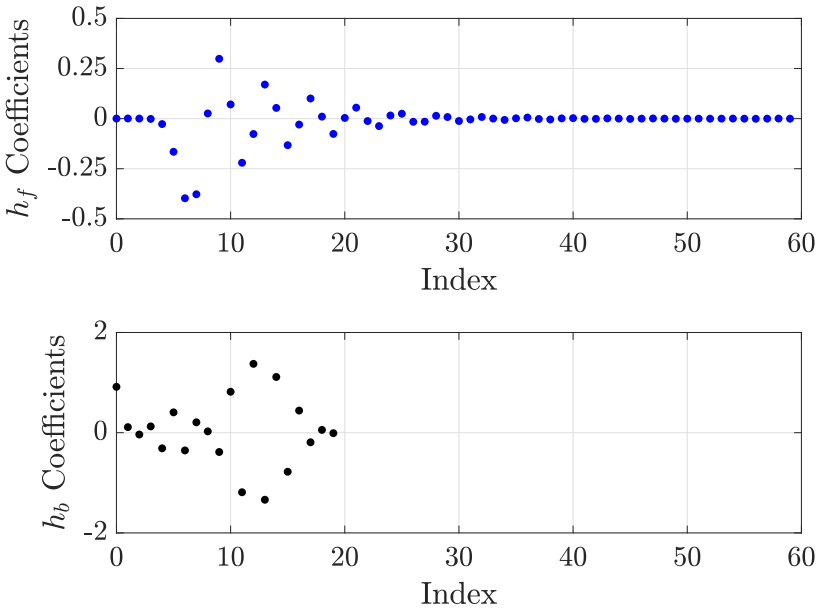

Figure 3.2: Filter coefficients for h_f (top) and h_b (bottom) where $\sum_k h_b[k] = 0.999$.

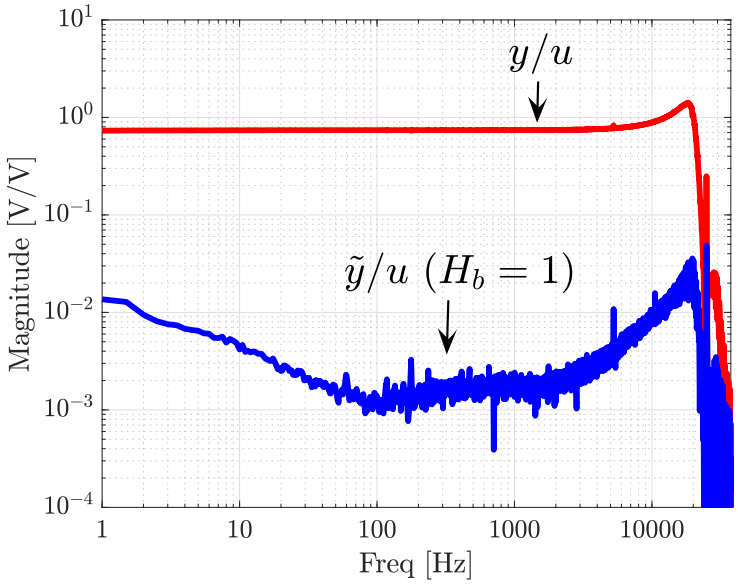

Figure 3.3: Open-loop empirical frequency responses y/u and $\tilde{y}/u$. The compensated frequency response $\tilde{y}/u$ is determined using the FIR feedforward filter h_f given in Fig. 3.2.

a few hundred hertz. This limited gain appears unjustified given the 40 dB reduction in feedthrough that was achieved in the open-loop system. The cause of the gain limitation is revealed in Fig. 3.5: when the beam is stabilized and the electrode capacitances are essentially equal, the feedthrough dynamics have changed from the open-loop case and its

cancellation is much poorer at higher frequencies thereby limiting the controller gain. An update of the open-loop plant about its nominal operating point are obtained by testing the *stabilized* system. In this case, the two closed-loop frequency responses y/d and u/d are measured relative to the external stimulus d, then, the open-loop frequency response is estimated as $y/u = (y/d)(u/d)^{-1}$.

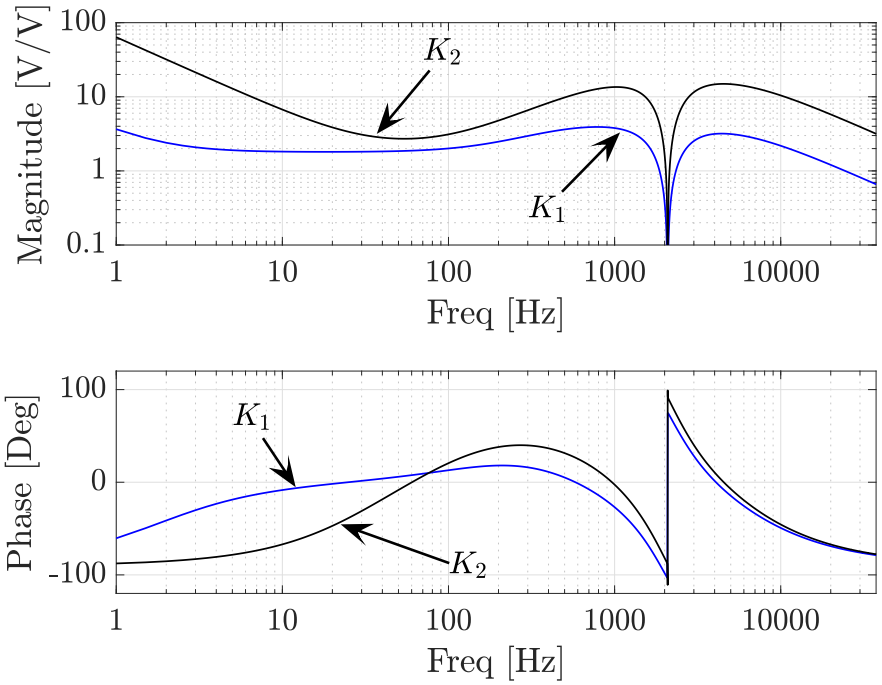

Figure 3.4: The controller K_1 stabilizes the system with either h_f or $h_b * h_f$ as the feedforward compensation filter, however, the stability margins are poor when only h_f is implemented. Improving the cancellation of the feedthrough by implementing $h_b * h_f$ will improve the stability margins, but the relatively low gain of K_1 means its disturbance rejection properties are modest. The controller K_2 has larger gains and provides superior disturbance rejection but can only be implemented when the high-frequency feedthrough is compensated by $h_b * h_f$.

Fig. 3.5 also clearly reveals the motional response of the beam in the frequency response of the compensated measurement, i.e. $\tilde{y}/u$. Also shown is an estimate of the uncompensated system, y/u. Agreement with the *model* frequency responses in Fig. 2.8 is excellent and lends further confidence to the approximate frequency response analysis discussed in Chapter 4. Despite the fact that the system is stabilized, the sensitivity function associated with the closed-loop system has undesirable properties. The sensitivity function

is denoted S_1 in Fig. 3.6. Note that the maximum value of $|S_1|$ is approximately 6 and that the closed-loop system is characterized by poor disturbance rejection and command tracking for frequencies above a few hertz.

3.2 Bootstrap Feedforward Filter

The impediment to decreasing the sensitivity is due to the limited controller gain which is a consequence of the incomplete cancellation of the feedthrough that manifested when the beam was stabilized. Thus, the issue is one of improving the feedthrough cancellation based on measurements of the stabilized system but because of the phase-lead nature of the controller, the cancellation need only be improved beyond 1 kHz. The motional response of the beam is greatly attenuated above 1 kHz, so by comparing y to v from closed-loop experiments for frequencies greater than 1 kHz, the deficiencies in the ability of h_f to model the feedthrough will be revealed. In practice, this is achieved by filtering the closed-loop signals v and y with identical high-pass filters, denoted H_{hp}, to produce the signals $\hat{v}$ and $\hat{y}$ (see Fig. 3.1). The outputs of the high-pass filters are correlated with the broadband stimulus d to produce the cross-correlation functions $R_{\hat{y}d}$ and $R_{\hat{v}d}$. Any difference between these cross-correlations is attributed to the imperfect modeling of the feedthrough by h_f since the corner frequency of H_{hp} is chosen so that any motional signals are filtered out. It is possible to determine a correction to the feedforward filter by searching for a causal filter, whose impulse response is given by h_b, such that $R_{\hat{y}d} = h_b * R_{\hat{v}d}$, where $*$ denotes convolution. The filter h_b is the *bootstrap feedforward filter*, which can be determined only after the system has been stabilized about its nominal operating point. The frequency response of h_b is denoted H_b and appears in series with the original feedforward filter H_f as shown in Fig. 3.1.

Since $R_{\hat{v}d}$ is not impulsive, h_b is determined from a least-squares problem. It is assumed

that h_b is also FIR with n taps. The least-squares problem is formulated as

$$\min_{\overrightarrow{h}_b} \ \| \overrightarrow{R}_{\hat{y}d} - \tilde{R}_{\hat{d}v} \overrightarrow{h}_b \|_2^2 + \gamma(1 - \mathbf{1} \overrightarrow{h}_b)^2, \tag{3.1}$$

where $\overrightarrow{h}_b$ is the vector of impulse response samples and $\overrightarrow{R}_{\hat{y}d}$ is the vector of cross-correlation values,

$$\overrightarrow{h}_b = \begin{bmatrix} h_b[0] \\ h_b[1] \\ \vdots \\ h_b[n-1] \end{bmatrix} \in \mathbf{R}^n, \quad \overrightarrow{R}_{\hat{y}d} = \begin{bmatrix} R_{\hat{y}d}[0] \\ R_{\hat{y}d}[1] \\ \vdots \\ R_{\hat{y}d}[p-1] \end{bmatrix} \in \mathbf{R}^p$$

and $\tilde{R}_{\hat{d}v} \in \mathbf{R}^{p \times n}$ is a Toeplitz matrix of cross-correlation values,

$$\tilde{R}_{\hat{d}v} = \begin{bmatrix} R_{\hat{d}v}[0] & 0 & \cdots & 0 \\ R_{\hat{d}v}[1] & R_{\hat{d}v}[0] & \cdots & 0 \\ \vdots & \vdots & \ddots & \vdots \\ R_{\hat{d}v}[n-1] & R_{\hat{d}v}[n-2] & \cdots & R_{\hat{d}v}[0] \\ \vdots & \vdots & \vdots & \vdots \\ R_{\hat{d}v}[p-1] & R_{\hat{d}v}[p-2] & \cdots & R_{\hat{d}v}[p-1-n] \end{bmatrix}$$

Furthermore, the elements of $\mathbf{1} \in \mathbf{R}^{1 \times n}$ are all 1 and $\gamma > 0$. The term with γ is a penalty to approximately enforce the constraint $\sum_k h_b[k] = 1$ which ensures that the DC gain of h_b is close to 1. This is important because h_b is in series with h_f and so it should preserve the magnitude and phase properties of h_f below the high-pass corner frequency: recall that h_b is designed so that only the high-frequency range of the feedthrough is modified with this filter –it is still necessary for h_f to provide effective feedthrough cancellation at lower frequencies, where the demarcation between high and low frequencies is the corner frequency of the high-pass filter H_{hp}.

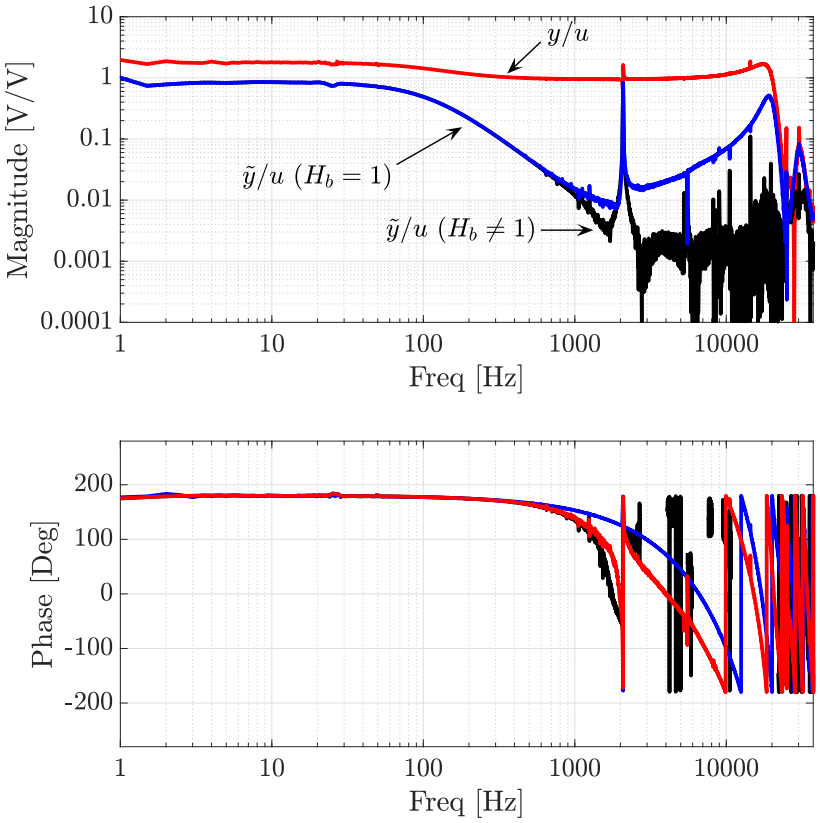

Figure 3.5: Comparison of open-loop frequency response estimates y/u, $\tilde{y}/u$, and $\overline{y}/u$ procured from closed-loop data. The compensated response $\tilde{y}/u$ is determined through the use of the fixed filter h_f whereas the improved high-frequency attenuation in $\overline{y}/u$ is achieved via implementation of $h_b * h_f$. A lightly damped flexural mode is evident near 2 kHz and is compensated for via a notch filter in the controller.

3.3 Experimental results

The experiments are performed with $i_{\text{ct}} \approx 2.65\,\text{mA}$, $\omega_0 = 25\,\text{kHz}$, sampling frequency $\omega_s = 75\,\text{kHz}$, H_s is a 4-pole low-pass Butterworth filter with 20 kHz corner frequency, and H_a is an 8-pole low-pass Butterworth filter with 20 kHz corner frequency. The experimental results are reported when $n = 20$ with the values of the taps of h_b determined from Eq. 3.1 shown in Fig. 3.2. The high-pass filters are 4-pole discrete-time filters with corner frequencies equal to 2.5kHz. Thus, the bootstrap feedforward filter attempts to match any residual feedthrough in $\tilde{y}$ beyond 2.5 kHz that is not captured by h_f.

The empirical frequency response when both feedforward filters are used is shown in

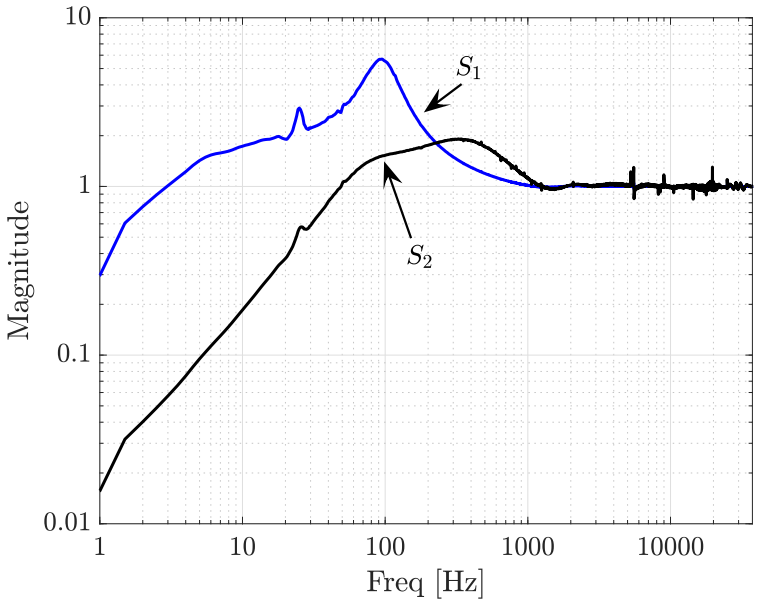

Figure 3.6: Measured sensitivity functions associated with the controllers.

Fig. 3.5 by the graph labeled $\overline{y}/u$ and illustrates that significant improvement in the high frequency suppression of the plant feedthrough is achieved. The feedforward compensated plant now allows for the implementation of a more aggressive controller possessing greater phase lead and larger low frequency gain. The updated controller is denoted K_2 in Fig. 3.4 and the corresponding sensitivity function is labeled S_2 in Fig. 3.6.

3.4 Sensitivity of the Feedforward Filter

A feedforward filter based on identifying a feedthrough model from open-loop testing is adequate for stabilizing the system, however, the closed-loop disturbance rejection properties are quite poor as evidenced by the sensitivity S_1 in Fig. 3.6. This is due to the high frequency limits placed on the controller gain due to imperfect cancellation in the stabilized system. Suppressing residual feedthrough at higher frequencies by adding additional low-pass filtering in the controller will erode the phase-lead that is necessary for stabilizing the plant and therefore is not a viable approach for dealing with the partial cancellation afforded by h_f. Indeed, the feedthrough is a function of the beam angle and so it is

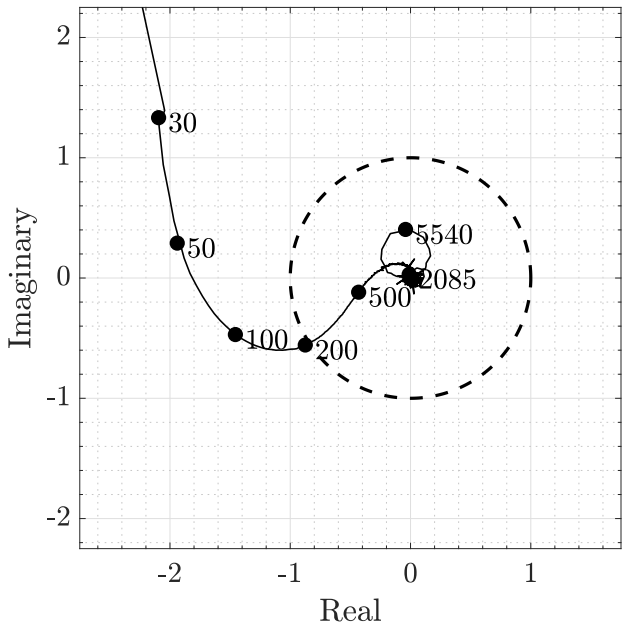

Figure 3.7: Nyquist plot of loop gain $(P - H_b H_f)C_2$. The closed-loop system is asymptotically stable. Frequency markers are given in Hertz.

necessary to identify the feedthrough about the nominal beam angle when the beam is stabilized. The bootstrap feedforward filter augments the initial feedforward filter to the improve high-frequency cancellation. Better matching of the feedthrough is obtained by testing the closed-loop system operating about the stabilized beam position and, once the correction to the initial feedthrough filter is determined and implemented as the filter h_b placed in series with h_f, a controller with greater phase lead is applied. The result is a large improvement in the sensitivity function (S_2 in Fig. 3.6). The Nyquist plot of the loop gain $(P - H_b H_f)C_2$ containing both feedforward filters is shown in Fig. 3.7. Since the plant is open-loop unstable with one unstable pole, the single necessary counterclockwise encirclement of $-1 + j0$ for closed-loop stability is evident in this figure. Removing the bootstrap feedforward filter (i.e., setting $H_b = 1$), however, produces an unstable closed-loop system as shown in the Nyquist plot of the modified loop gain $(P - H_f)C_2$ in Fig. 3.8.

The desirable sensitivity properties of S_2 in Fig. 3.6 only address uncertainty associated with the compensated plant $P - H_b H_f$. In order to determine the sensitivity to mismatch between the feedforward filters and the plant feedthrough, it is necessary to study another

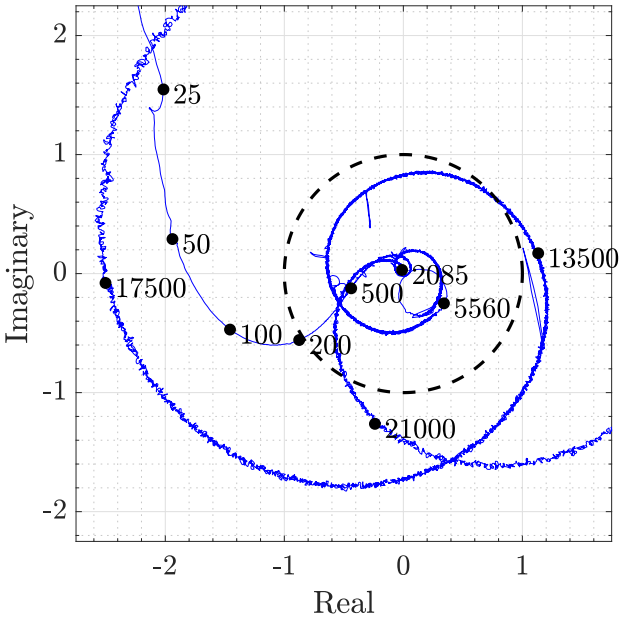

Figure 3.8: Nyquist plot of loop gain $(P - H_f)C_2$ without the bootstrap feedforward filter H_b indicating an unstable closed-loop system.

closed-loop transfer function. A perturbation at the output of P is shown as the block Δ in Fig. 3.1. This perturbation is in a feedback loop with the stable system given by y/w,

$$y/w = \frac{-PC_2}{1 + (P - H_b H_f)C_2},$$

where it is assumed the controller C_2 is used in the analysis. The magnitude of y/w is graphed in Fig. 3.9 and shows that the stability of the closed-loop system is quite sensitive to high-frequency uncertainty in the plant, which is governed by the plant feedthrough. In fact, if good feedthrough cancellation is achieved, then $|(P - H_b H_f)C_2| << 1$ at high frequencies so $y/w \approx -PC_2$ at high frequencies. Thus, better cancellation in principle permits high-gain controllers, however, the closed-loop system becomes more sensitive to deviations between the actual feedthrough and the feedforward filters that are intended to cancel the feedthrough. This trade-off appears to be unavoidable if a more "traditional" sensitivity function like S_2 is desired. The alternative is to implement a controller that does not provide much performance beyond stabilizing the system.

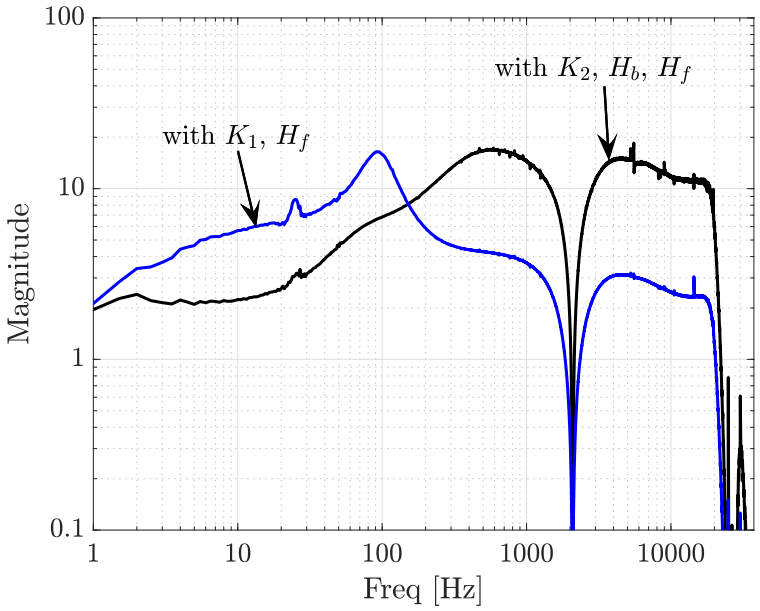

Figure 3.9: Frequency response of y/w illustrating the sensitivity of the closed-loop system to perturbations in the plant feedthrough.

It is reasonable to question whether using an electrode for both sensing and actuation is justified because of the complexity of identifying an accurate feedthrough model and then implementing an appropriate feedforward filter. The answer will depend on the application, but if the total electrode area is fixed, then segregating the sensing and actuation functions will lower the motional gain since less sensing area is available. This will reduce the signal-to-noise ratio of the measurement associated with the proof mass displacement. Furthermore, the actuation electrode potentials will increase for two reasons. First, the reduction in electrode area requires higher potentials to effect the same electrostatic forces, and, second, the electrostatic forces created by the sensing electrodes must now be overcome. These higher potentials are a real concern since dielectric breakdown is a risk with the small electrode-proof mass gaps. The sparking that can occur in the gaps can erode the electrodes and also damage the proof mass.

CHAPTER 4

Approximate Frequency Response

An approximate frequency response associated with Eq. 2.15 was derived through the discrete-time approximation in Eq. 2.16. The frequency responses associated with the electrical measurements of the beam angle were displayed in Fig. 2.8. However, these responses are effectively limited by the "sample-rate" of the discrete-time approximation determined by the carrier, ω_0. Regardless, it is possible to derive an approximate frequency response associated with a discrete-time system whose sample rate matches that of the controller. The key point is that the beam acts like a low-pass filter with regard to the rapidly varying electrostatic forces acting on it. The rapid variation is at twice the carrier frequency, i.e. $2\omega_0$. Thus, the beam essentially responds to the mean value of the forces. There is also additional band-limiting due to the smoothing and anti-alias filters. Under these conditions, an "improved" approximate frequency response is obtained which closely matches the motional and feedthrough measurements on the physical system reported in Section 3.3.

Consider the solution of Eq. 2.15

$$\delta(t) = \Phi(t, t_0)\delta(t_0) + \int_{t_0}^{t} \Phi(t, \tau) B_\delta(\tau) u(\tau) d\tau, \tag{4.1}$$

where $t \geq t_0$ and $\delta(t_0)$ is the initial condition. The controller sample rate is denoted ω_s (in hertz) and the corresponding sampling period is $t_s = 1/\omega_s$. The experiments in Section 3.3 employ a sample rate of $\omega_s = 3\omega_0$, so $t_s = \tau_p/3$. In other words, the controller sample rate is three times the carrier frequency. The analysis focuses on this case since it reflects the

experimental conditions. It is also assumed that $t_0 = 0$.

First, consider u to be constant, which may be taken to be 1 without loss of generality because of the linearity of the differential equations. It is possible to find periodic solutions for all state variables because $\Phi(\tau_p, 0)$ does not have an eigenvalue equal to one. The states are periodic with period τ_p (may not be the minimal period) because it is possible to solve for $\delta(t)$ by enforcing $\delta(t + \tau_p) = \delta(t)$ in Eq. 4.1,

$$\delta(t) = (I - \Phi(t + \tau_p, t))^{-1} \int_t^{t+\tau_p} \Phi(t + \tau_p, \tau) B_\delta(\tau) d\tau.$$

As t is varied over one period, say the interval $[0, \tau_p]$, the periodic solution of the state vector is obtained. When the beam angle deviation δ_θ is extracted from the state vector, it is discovered that the ratio of its peak-to-peak variation to its average value is less than 10^{-5} for the transformer-beam model in Fig. 2.3. In other words, for all practical purposes δ_θ can be taken to be constant. Nevertheless, further analysis shows that the beam angle is actually periodic with period $\tau_p/2$. This is not surprising because the electrostatic forces on the beam are proportional to the square of the electrode voltages, thus, with a constant control voltage, the time-varying portion of the electrostatic forces are sinusoids with twice the carrier frequency, i.e. $2\omega_0$. This demonstrates the beam acts like a low-pass filter as far as the amplitude modulated electrode voltages are concerned. This observation forms the basis of the approximate frequency response derivation proposed below.

The case when u is not constant is now analyzed. The DSP implements a zero-order-hold on the discrete-time control sequence so it is possible to integrate the equations of motion over one sample period t_s. Thus, define,

$$\begin{aligned} \Phi_k &= \Phi(kt_s, (k-1)t_s), \\ \Gamma_k &= \int_{(k-1)t_s}^{kt_s} \Phi(kt_s, t) B_\delta(t) dt, \end{aligned} \qquad k = 1, 2, 3.$$

Consider a sequence $\{u_n\}$, $n \in \mathbb{Z}$, issued by the discrete-time controller. Define the se-

quence $\{\delta_n\}$ where $\delta_n = \delta(nt_s)$. It is evident

$$\begin{aligned}
\delta_{n+1} &= \Phi_1\delta_n + \Gamma_1 u_n \\
\delta_{n+2} &= \Phi_2\delta_{n+1} + \Gamma_2 u_{n+1} \\
\delta_{n+3} &= \Phi_3\delta_{n+2} + \Gamma_3 u_{n+2} \qquad \text{when } n \equiv 0 \pmod 3 \\
\delta_{n+4} &= \Phi_1\delta_{n+3} + \Gamma_1 u_{n+3} \\
&\vdots
\end{aligned} \tag{4.2}$$

If $n \not\equiv 0 \pmod 3$ then there are permutations of Φ_k and Γ_k in the expressions for the samples of δ in Eq. 4.2 and this scenario corresponds to selecting $t_0 \in \{t_s, 2t_s\}$. The conclusions of the analysis do not change, though, for arbitrary t_0. Generally, sinusoidal solutions describing consecutive samples of δ_n do not exist for Eq. 4.2, however, because of the cyclic nature of the mappings, it is possible to relate every third sample with linear time-invariant expressions,

$$\begin{aligned}
\delta_{n+3} &= \Phi_3\Phi_2\Phi_1\delta_n + \Phi_3\Phi_2\Gamma_1 u_n \\
&\quad + \Phi_3\Gamma_2 u_{n+1} + \Gamma_3 u_{n+2} \\
\delta_{n+4} &= \Phi_1\Phi_3\Phi_2\delta_{n+1} + \Phi_1\Phi_3\Gamma_2 u_{n+1} \\
&\quad + \Phi_1\Gamma_3 u_{n+2} + \Gamma_1 u_{n+3} \qquad \text{when } n \equiv 0 \pmod 3 \\
\delta_{n+5} &= \Phi_2\Phi_1\Phi_3\delta_{n+2} + \Phi_2\Phi_1\Gamma_3 u_{n+2} \\
&\quad + \Phi_2\Gamma_1 u_{n+3} + \Gamma_2 u_{n+4}
\end{aligned} \tag{4.3}$$

The notion of a frequency response function is developed by assuming the input sequence is sinusoidal, in other words, $u_n = e^{j2\pi\omega nt_s}$, and that $\delta_n = \hat{\delta}_0 e^{j2\pi\omega nt_s}$, $\delta_{n+1} = \hat{\delta}_1 e^{j2\pi\omega(n+1)t_s}$, and $\delta_{n+2} = \hat{\delta}_2 e^{j2\pi\omega(n+2)t_s}$, where $\hat{\delta}_0$, $\hat{\delta}_1$, and $\hat{\delta}_2$ are to be determined. Substituting these sinusoids into Eq. 4.3 and noting $\delta_{n+3} = \hat{\delta}_0 e^{j2\pi\omega\tau_p} e^{j2\pi\omega nt_s}$, $\delta_{n+4} = \hat{\delta}_1 e^{j2\pi\omega\tau_p} e^{j2\pi\omega(n+1)t_s}$ and

$\delta_{n+5} = \hat{\delta}_2 e^{j2\pi\omega\tau_p} e^{j2\pi\omega(n+2)t_s}$ yields the following expressions,

$$\begin{aligned}
\hat{\delta}_0 &:= \left(e^{j2\pi\omega\tau_p} I - \Phi_3\Phi_2\Phi_1\right)^{-1} \tilde{\Gamma}_1 \\
\hat{\delta}_1 &:= \left(e^{j2\pi\omega\tau_p} I - \Phi_1\Phi_3\Phi_2\right)^{-1} \tilde{\Gamma}_2 \\
\hat{\delta}_2 &:= \left(e^{j2\pi\omega\tau_p} I - \Phi_2\Phi_1\Phi_3\right)^{-1} \tilde{\Gamma}_3,
\end{aligned} \tag{4.4}$$

where

$$\begin{aligned}
\tilde{\Gamma}_1 &:= \Phi_3\Phi_2\Gamma_1 + \Phi_3\Gamma_2 e^{j2\pi\omega t_s} + \Gamma_3 e^{j4\pi\omega t_s} \\
\tilde{\Gamma}_2 &:= \Phi_1\Phi_3\Gamma_2 + \Phi_1\Gamma_3 e^{j2\pi\omega t_s} + \Gamma_1 e^{j4\pi\omega t_s} \\
\tilde{\Gamma}_3 &:= \Phi_2\Phi_1\Gamma_3 + \Phi_2\Gamma_1 e^{j2\pi\omega t_s} + \Gamma_2 e^{j4\pi\omega t_s}
\end{aligned} \tag{4.5}$$

This reveals that every third sample can in fact be expressed in "frequency response" form, however, consecutive samples generally cannot be expressed in this manner. Despite this fact, any rapidly varying electrostatic forces on the beam over one period of the carrier can be assumed to produce an *average* effect due to the filtering by the beam inertia. Thus, the beam motion, and by extension the output voltage y which represents a superposition of the beam motion with the feedthrough, can be approximated by the *average* of Eq. 4.4. In other words, the "frequency response" of the system is taken to be

$$y/u = \frac{1}{3} C_\delta \left(\hat{\delta}_0 + \hat{\delta}_1 + \hat{\delta}_2\right). \tag{4.6}$$

This expression is used to compute an approximate frequency response for the transformer-beam system from the perspective of the discrete-time controller. The frequency range extends to the Nyquist frequency associated with the controller sample rate, i.e. 37.5 kHz. It is evident from Section 3.3 that the approximate frequency response analysis has excellent agreement with the measurement data. However, further analysis of this method needs to be considered to pose a well-defined mathematical framework for this representation.

Part II

Electrostatically Suspended Disk

CHAPTER 5

Analysis and Control of an Electrostatically Suspended Disk

In this chapter, the model of the electrostatically suspended disk and analysis thereof is presented. The plant for this unstable system consists of two glass plates, with the same electrode pattern, stacked with an aluminum-coated disk in-between. Precision spacers are manufactured to create a well-established gap between the glass plates. As before, the electrodes perform the task of both supplying the electrostatic forces and sensing gap changes between the disk and electrodes. The electrode pattern on one glass plate consists of eight electrodes, four pie-shaped "primary" electrodes for the task of providing the vast majority of electrostatic forces and torques and four outboard "lateral" electrodes to detect lateral translations. Each electrode is accessed via a lead connecting the electrode to a pad for wirebonding. This pattern was specifically designed so the upper electrode set overlays the lower set (save for the leads to the wirebond pads) and allow the wirebonds to be free of obstruction when the platform is assembled (see Fig. 5.1). The central electrodes are essentially quarters of a circle with a radius slightly smaller than that of the disk. When the platform is fully assembled, the disk circumference protrudes from the outer radius of the central electrodes and prevents the central electrodes on either glass from being exposed to the other. Of course, this is only the case for a range of perturbations from the disk being centered in the electrode pattern. The outboard electrodes are essentially quarters of an annulus, the inner radius being 1mm from the central electrode pattern and the outer radius 3mm larger than the disk radius. Ultimately, this pattern is used to

detect lateral translations of the disk. Regardless of the disk orientation and position, the electrostatic forces and torques are modeled to act on the disk at the projected location of the electrode geometric center to the disk.

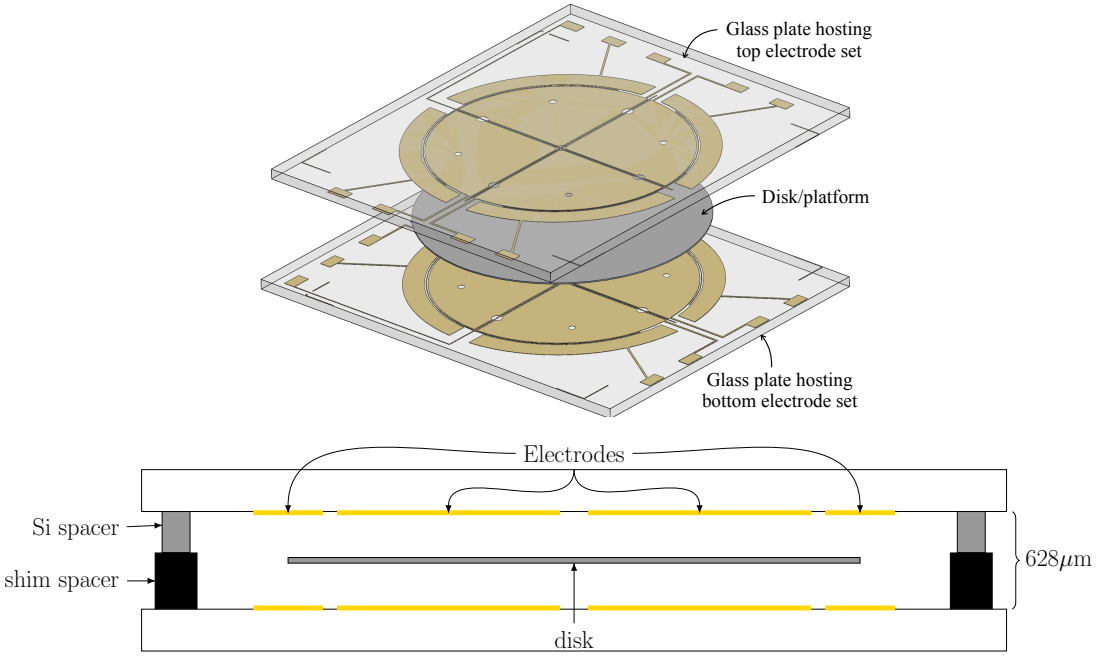

Figure 5.1: (Top) Isometric view of electrode configuration (Bottom) Side view of assembled system (not to scale)

The nominal position of the disk is considered to be when the disk is centered with respect to the electrode pattern and a uniform gap is present between the disk and both electrode sets. This is indicated through the electronics by a zero differential capacitance through each central electrode pair. Zero net charge develops on the disk as a result of the current sourced to the center taps.

5.1 Fabrication

Most of fabrication techniques used to produce the 1DOF beam system are used to create the platform for suspension of an aluminum-coated silicon disk. Two 3 mm thick glass substrates are patterned (via image reversal) to produce the electrodes and wirebond pads.

These patterns consist of a 10nm thick Ti adhesion layer directly on the glass covered by a 2-micron thick silver layer. A final 100 nm "cap" of gold covers the silver. The wire bond pads are situated outboard from the geometric center (see Fig. 5.1) of the electrode pattern and act as the means of connecting the transformer leads to the electrodes. To protect the electrodes (and the disk) from voltage breakdown, a 20 μm layer of photoresist is hard baked on top of the exposed electrodes. This protective layer significantly increases the dielectric strength between the disk and electrodes. The disk is etched out of a 400 μm thick, double-side polished silicon wafer. A layer of aluminum coats the disk to create an electrically conductive body and warrant the modeling of the disk as an equipotential body. To create the gap, smaller disks 1 mm in diameter are etched out of the same piece of silicon as the disk. Etching these "spacers" out of the same piece of silicon is a simple method for ensuring the precision of the electrode-disk gap. Additional spacers are machined out of precision shim stock via a wire-cut EDM. The thickness of these spacers define the electrode-disk gap (Fig. 5.1) when the platform is assembled as the silicon spacers accounts for the thickness of the disk. Alignment markers on both glass plates (patterned with the electrodes) assist with the assembly and ensure the projected electrode footprints onto one side of the disk are aligned with the corresponding footprint on the other side. The relevant dimensions are given in Table 5.1.

Assembly Parameters

Parameter	**Value**
disk diameter	82 mm
disk thickness	400 μm
disk mass, m	4.92×10^{-3} kg
primary electrode area, A_p	10.3 cm^2
lateral electrode area, A_l	1.65 cm^2
dielectric constant, ϵ	8.85×10^{-12} F $\cdot$ m^{-1}
radial distance to electrode geometric center, r_0	2.22 cm
nominal beam/electrode gap, z_0	134 μm
in-plane moment of inertia, J_z	4.13×10^{-6} kg $\cdot$ m^2
in-plane moment of inertia, J_{xy}	2.07×10^{-6} kg $\cdot$ m^2

Table 5.1: Table of disk parameter values

5.2 Plant Description

5.2.1 Electrode and Disk Geometry

The electrode patterns on the top and bottom glass plates are identical. The plates are assembled so that they are parallel and an electrode on the top plate is aligned with a mirror-image electrode on the bottom plate. The schematic in Fig. 5.2 identifies the electrodes and shows an exploded view of the assembly (the disk-electrode gaps are not to scale). When the disk is uniformly centered between the sets of electrodes there is a disk-

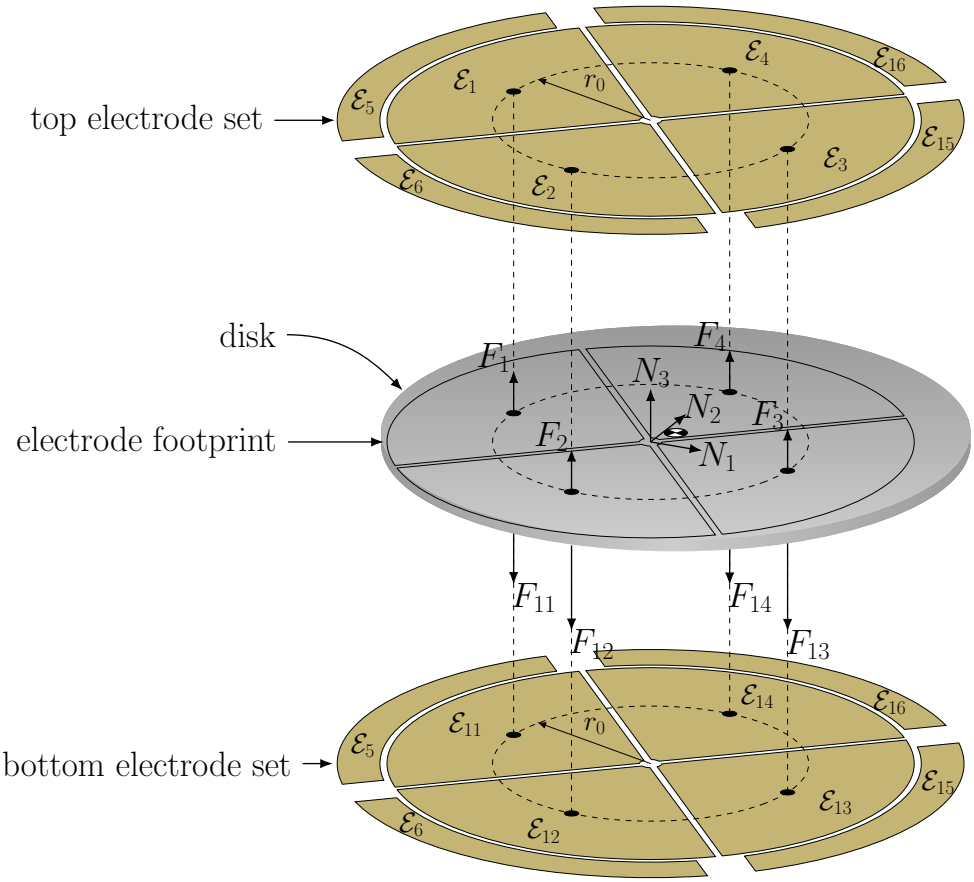

Figure 5.2: View of the electrode configuration and disk. The primary electrodes are labeled $\mathcal{E}_1$, $\mathcal{E}_2$, $\mathcal{E}_3$, and $\mathcal{E}_4$ for the top electrode set, and $\mathcal{E}_{11}$, $\mathcal{E}_{12}$, $\mathcal{E}_{13}$, and $\mathcal{E}_{14}$ for the bottom electrode set. The lateral electrodes are labeled $\mathcal{E}_5$, $\mathcal{E}_{15}$, $\mathcal{E}_6$, and $\mathcal{E}_{16}$. Note that a single lateral electrode has an element on both the top and bottom.

electrode gap of approximately 134μm between the top of the disk and top electrode set,

and a 134μm gap between the bottom of the disk and the bottom electrode set. The four pie-shaped primary electrodes are labeled $\mathcal{E}_1$ through $\mathcal{E}_4$ for the top set and $\mathcal{E}_{11}$ through $\mathcal{E}_{14}$ for the bottom set. The primary electrodes are grouped into four pairs: the electrodes immediately facing each other (with the disk between them) form one pair, e.g., $\mathcal{E}_1$ and $\mathcal{E}_{11}$ form one primary pair. Each primary pair exert controlled electrostatic forces on the disk and also measure differential electrode-disk capacitances. The capacitance measurements are related to the disk-electrode gaps associated with each primary pair and can be used to infer the disk's center of mass vertical position and the two tilt angles (treating the disk as a rigid body). It will be shown that the primary electrodes can stabilize the rigid body motion of the disk with the exception of "yaw" motion about the N_3–axis. Yaw is not observable using these measurements and so is not controlled. An important note to make is that lateral motion in the $N_1 - N_2$ plane is also stabilized using only the primary electrodes because the lateral and tilt degrees-of-freedom are coupled in the suspended disk. It is possible, in principle, to control the lateral position of the disk without lateral measurements, however, effective regulation requires direct measurement of these quantities due to uncertainty associated with the system. Lateral electrodes measure the disk's position in the $N_1 - N_2$ plane. In reality there are only for lateral electrodes because mirror image electrodes on the top and bottom plates actually form a single electrode (the top and bottom electrode sets both have lateral electrodes labeled $\mathcal{E}_5$, $\mathcal{E}_{15}$, $\mathcal{E}_6$, $\mathcal{E}_{16}$). The lateral electrodes are also grouped into (two) pairs with antipodal electrodes creating a pair, e.g., $\mathcal{E}_5$ and $\mathcal{E}_{15}$ form a lateral pair. A lateral pair provides a differential capacitance measurement that is proportional to the lateral position of the disk relative to the pair, e.g., $\mathcal{E}_5$ and $\mathcal{E}_{15}$ measure disk displacement in the N_1-coordinate direction. The lateral electrode configuration also largely rejects the disk's vertical and tilting rigid body motion. The differential capacitance measurements provide convenient null positions: if all differential capacitances of the primary pairs are zero then the disk is parallel to the electrodes with uniform and equal gaps between the disk and primary electrodes. Similarly, if the differential capacitances of the lateral pairs are zero then the disk is symmetrically centered relative to the lateral electrodes. Deviation from the null positions generate non-zero measurements that are

acted upon by the controller. The diameter spanned by the lateral electrodes is larger than the disk diameter and consequently when the disk is near its null position the net in-plane forces exerted on the disk by electrical fringe fields is essentially zero (Appendix A). It is possible to exert in-plane forces on the disk, however, this requires that the disk be tilted relative to the plane of the electrodes: the disk is an equipotential body so the field likes are normal to the disk's top and bottom surface. If the disk is titled to be non-parallel to the primary electrodes, the electrostatic forces exerted on the disk will have a non-zero in-plane component. It will be shown that this property can be exploited to control the disk's lateral position. As such, the system is regulated in all the degrees of freedom, translation in z, the angular rotations θ and φ, and two lateral translations x and y. Rotation about the B_3-axis (yaw) is not measured or tracked. Collectively, the suspension system is a 5-DOF unstable plant.

5.2.2 Electrical Interface

The pairing of primary electrodes is achieved with transformers as illustrated in Fig. 5.3. A given primary pair is connected to its transformer's primary leads. The transformer's primary windings have equal inductances connected at the center tap (ct). The center tap is driven with a sinusoidal current

$$i_{\mathrm{ct}}(t) = a_{\mathrm{ct}} \cos\left(2\pi\omega_0 t\right)$$

where a_{ct} is the (constant) amplitude and ω_0 is the carrier frequency. An auxiliary transformer is connected to the center taps of two transformers linked to two primary electrode pairs. In this configuration, current flowing onto the disk through one center tap is pulled off through the "adjacent" center tap as indicated in Fig. 5.3. Thus, if the disk is initially at ground potential, it is maintained at ground potential even when suspended. By maintaining the disk at ground, any difference between the capacitances in a pair of primary electrodes will produce a sinusoidal voltage drop across the transformer's secondary wind-

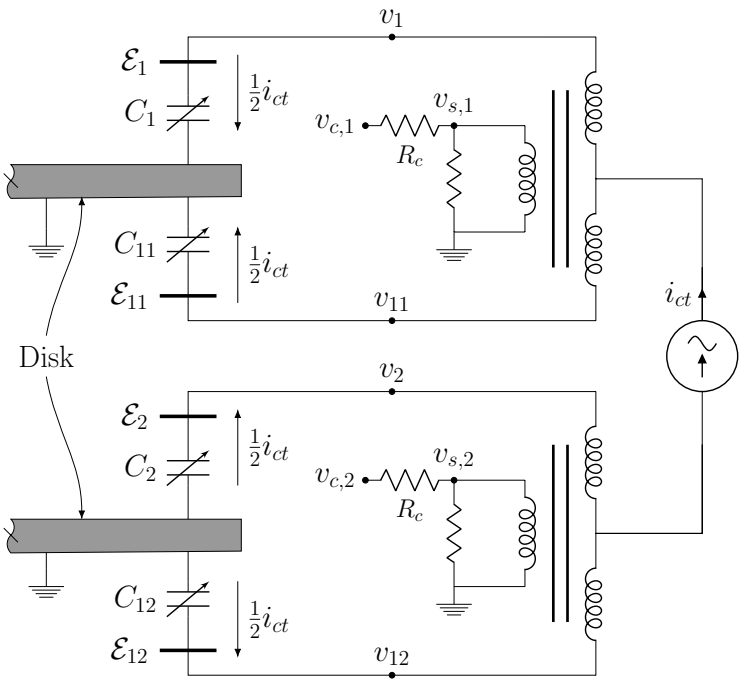

Figure 5.3: Circuit schematic illustrating the connection between the transformers and the $\mathcal{E}_1 - \mathcal{E}_{11}$ and $\mathcal{E}_2 - \mathcal{E}_{12}$ pairs of primary electrodes. The corresponding capacitances developed between the electrodes and disk are also shown. The disk is not physically grounded, however, the notation is used to convey that the disk is at ground potential due to the coordination of the center tap currents. The connection to $\mathcal{E}_3 - \mathcal{E}_{13}$ and $\mathcal{E}_4 - \mathcal{E}_{14}$ is identical. A comprehensive illustration of the disk-electronics interface is shown in Fig. 5.10

ings. For example, the primary pairs $\mathcal{E}_k$ and $\mathcal{E}_{1k}$, $k = 1, 2, 3, 4$, are associated with capacitances C_k and C_{1k}; if $C_k = C_{1k}$, indicating that the average gap between the disk and $\mathcal{E}_k$ is equal to the average gap between the disk and $\mathcal{E}_{1k}$, then $v_{\mathrm{s},k} = 0$, where $v_{\mathrm{s},k}$ is the "sense voltage" across the secondary winding associated with the kth set of paired electrodes. On the other hand, if the average gaps are not equal ($C_k \ = C_{1k}$) then $v_{\mathrm{s},k}$ is sinusoidal with frequency ω_0. Synchronous demodulation of $v_{\mathrm{s},k}$ yields a signal proportional to the imbalance in the disk-electrode gap associated with $\mathcal{E}_k$ and $\mathcal{E}_{1k}$. The phase of the demodulator is chosen to maximize the component of $v_{\mathrm{s},k}$ due to disk displacement from its null position. The center tap current provides the master phase against which all sinusoidal signals are referenced. Furthermore, the inductances of the transformer primary windings are large enough so that the nominal inductor-capacitor resonant frequency is smaller than the carrier frequency. So, to first order, the center tap current is evenly split between the primary

inductances in a given transformer independent of the disk-electrode capacitances.

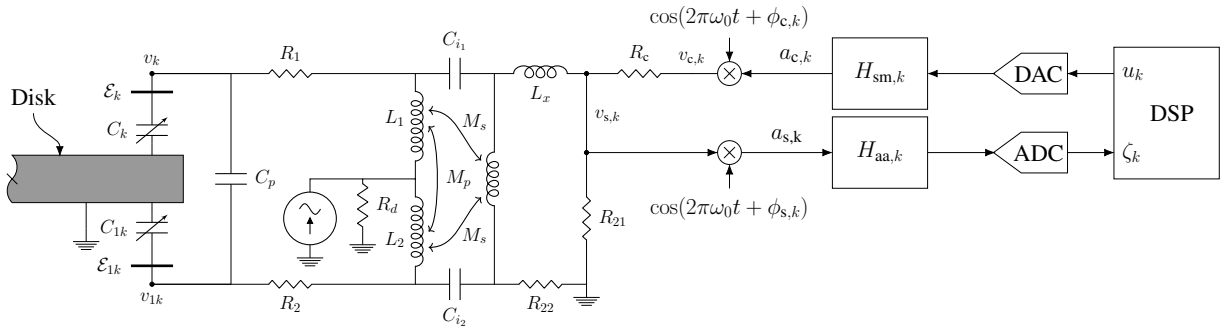

Figure 5.4: Interface between the DSP and transformer signals for the primary electrodes. The anti-alias and smoothing filters are denoted $H_{\rm aa}$ and $H_{\rm sm}$, respectively. The lateral electrodes use a similar demodulation scheme, however, since no control signals are associated with the lateral electrodes, the modulation path is not present for the lateral electrode signal conditioning.

The transformers are also used for exerting controlled electrostatic forces on the disk. The "control potential" $v_{{\rm c},k}(t) = a_{{\rm c},k}(t)\cos\left(2\pi\omega_0 t + \phi_{{\rm c},k}\right)$ is applied at resistor R_c that is in series with the transformer secondary load as shown in Fig. 5.4. This produces a differential sinusoidal potential on each electrode in a primary electrode pair, i.e., electrode potentials arising from $v_{{\rm c},k}$ invariably have a 180° phase difference due to the magnetic coupling within the transformer windings. In contrast, the $i_{\rm ct}$-induced potentials on both electrodes are in-phase with one another. The superposed effects of $i_{\rm ct}$ and $v_{{\rm c},k}$ are sinusoidal with frequency ω_0 and so the control signal phase $\phi_{{\rm c},k}$ is selected so the $v_{{\rm c},k}$-induced component on electrode $\mathcal{E}_k$ is in-phase with the $i_{\rm ct}$-induced voltage and therefore the $v_{{\rm c},k}$-induced component of $\mathcal{E}_{1k}$ is 180° out of phase with the $i_{\rm ct}$-induced component. When $\phi_{{\rm c},k}$ is chosen in this manner, changing $a_{{\rm c},k}$ produces a differential change in the amplitudes of the sinusoidal potentials on the paired electrodes, and because the electrostatic forces are proportional to the square of the electrode voltages, this creates the largest differential electrostatic force on the disk for a given value of $a_{{\rm c},k}$. In fact, as far as the disk is concerned, the mean square value of the electrode voltages over a certain bandwidth creates effective forces which can be used as a proxies for the exact electrostatic forces because the disk acts as a low-pass filter. This fact is exploited in deriving the approximate

frequency response functions. The amplitude-modulated sinusoids $v_{\mathrm{s},k}$ and $v_{\mathrm{c},k}$ are demodulated and modulated, respectively, to produce the baseband signals that are sampled and manipulated by the discrete-time controller. The block diagram showing the modulation/demodulation is shown in Fig. 5.4. The modulation/demodulation and filtering is accomplished with analog electronics, and a DSP is used to the implement feedforward filters, coordinate transformations, and the feedback compensation. The "baseband" signals $\{u_1, u_2, u_3, u_4\}$ (input) and $\{\zeta_1, \zeta_2, \zeta_3, \zeta_4\}$ (output) represent and electro-mechanical model of the suspended disk. The lateral electrodes, $\mathcal{E}_5$, $\mathcal{E}_{15}$, $\mathcal{E}_6$, and $\mathcal{E}_{16}$, measure lateral displacements of the disk and are connect to transformers according to Fig. 5.5. In this configuration, lateral translations of the disk change the overlapping areas between the disk and the paired lateral electrodes. The voltage drop across the transformer secondary is proportional to differential capacitance arising from the differential area change. These electrodes are not biased by a control voltage and therefore their potentials are dictated by the potential established by the center-tap current and lateral electrode-disk capacitances. Although the same symbol is used to denote the center-tap current for the lateral electrodes, it is typically 15% of the current supplied to the primary electrodes. The lateral electrodes provide the additional baseband measurements $\{\zeta_5, \zeta_6\}$.

5.2.3 Detecting Lateral Motion

Although not actively controlled, it is desirable to passively control the lateral motion of the disk in order to maintain the disk near the desired nominal configuration. As such, the outboard electrodes, $\mathcal{E}_5 - \mathcal{E}_{18}$, are used to detect a lateral displacement. The outboard electrodes are connected to transformers in a different fashion as compared to the primary electrode pairs. Each pair of electrodes on either side of the disk are shorted together to boost the measured capacitance since the representative electrode area is smaller than the primary electrodes. In order to perform the transduction due to a lateral motion, the differential capacitance is measured by connecting the antagonistic pairs along each principal axis defined by Fig. 5.2. Fig. 5.5 illustrates the connection of the electrodes to their

transformers. In this configuration, purely vertical motions and tilts of the disk induce a zero differential capacitance change between the transformer leads and therefore produce no voltage drop across the transformer secondary.

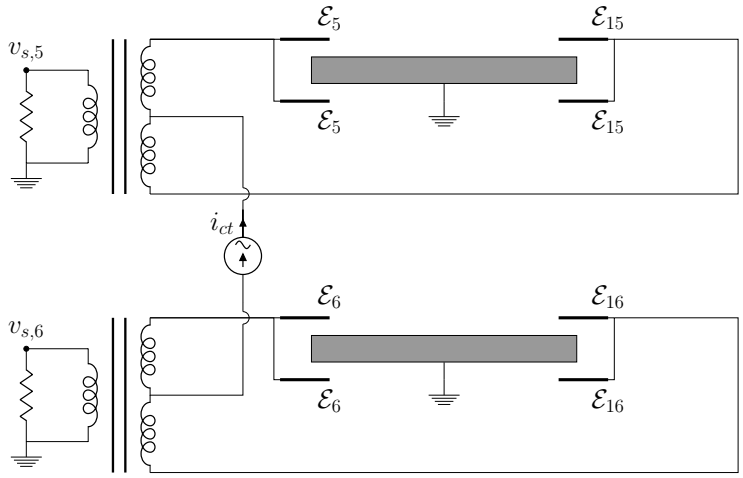

Figure 5.5: Pairing of lateral electrodes for sensing the position of the disk in the $N_1 - N_2$ plane. Note $\mathcal{E}_5$ is antipodal to $\mathcal{E}_{15}$, and $\mathcal{E}_6$ is antipodal to $\mathcal{E}_{16}$, as shown in Fig. 5.2.

Translational motion of the disk results in changes in the overlap between the disk and the outboard electrodes. It is therefore reasonable to investigate how the capacitance between the disk and outboard electrodes changes as the disk moves laterally with a fixed gap. Under the small angle assumption, the capacitance between the disk and any outboard electrode is described by a parallel plate model:

$$C_k(q) = \frac{\epsilon_0 \epsilon_r A_{l,k}(q)}{z_0 - z_k} \quad k = 5, \ldots, 8$$
$$C_{1k}(q) = \frac{\epsilon_0 \epsilon_r A_{l,1k}(q)}{z_0 + z_k} \quad k = 5, \ldots, 8$$

where $A_{l,k}(q)$ represents the overlapping area of the electrode projected onto the disk and z_k is the length of the normal vector from the geometric center of the overlapping area

between the outboard electrode to the disk (denoted r_1), given by

$$\begin{aligned} z_5 &= z + (r_1 + x)\,\varphi - y\theta \quad z_6 = z - (r_1 + y)\,\theta + x\varphi \\ z_7 &= z - (r_1 - x)\,\varphi - y\theta \quad z_8 = z + (r_1 - y)\,\theta + x\varphi \end{aligned} \tag{5.1}$$

Seeing as the capacitance between the disk and $\mathcal{E}_k$ and $\mathcal{E}_{1k}$ (for $k = 5, \ldots, 8$) are essentially in parallel (from the perspective of the transformer leads), the capacitance between the pair of outboard electrodes $\mathcal{E}_k$ and $\mathcal{E}_{1k}$ and the disk is expressed as the sum

$$C_k\,(q) = \epsilon_0 \epsilon_r \left(\frac{A_{l,k}\,(q)}{z_0 - z_k} + \frac{A_{l,1k}\,(q)}{z_0 + z_k} \right), \quad k = 5, \ldots, 8. \tag{5.2}$$

The projected area is determined by evaluating the geometry of the disk and electrodes. Angular deflections technically affect the area calculation, however, this effect is considered negligible and excluded from the analysis. The area computation in each capacitance model is therefore only determined by translations in x and y. As a result, $A_{l,k}(x, y) = A_{l,1k}(x, y)$ and Eq. 5.2 may be simplified further

$$C_k\,(q) = \epsilon_0 \epsilon_r A_{l,k}\,(x, y) \left(\frac{1}{z_0 - z_k} + \frac{1}{z_0 + z_k} \right), \quad k = 5, \ldots, 8. \tag{5.3}$$

Computation of the projected area on the disk is governed by the general equation of a circle,

$$(x_p - x)^2 + (y_p - y)^2 = r_d^2$$

where r_d is the disk radius and x_p and y_p represent the points on the disk edge (in the inertial frame coordinates). Allowing $x_p = r\cos\lambda$, $y_p = r\sin\lambda$, $x = \delta_r \cos\kappa$, and $y = \delta_r \sin\kappa$, the governing equation of the area may be expressed in polar coordinates,

$$r^2 - 2\delta_r \cos(\lambda - \kappa) r + \delta_r^2 = r_d^2$$

where the pair (r, λ) represent a point on the disk edge, and (δ_r, κ) represent the polar

coordinate for the disk center. Points on the disk edge are then given by

$$r = \delta_r \cos(\lambda - \kappa) + \sqrt{r_d^2 - \delta_r^2 \sin^2(\lambda - \kappa)} \tag{5.4}$$

for $-\pi \leq \lambda \leq \pi$. The area for any overlapping region is then

$$\begin{aligned} A_{l,k}(x,y) &= \int_{\Lambda_k} \frac{1}{2} r^2 d\lambda - \left(\frac{\pi}{4} r_i^2 + a_x\right) \\ &= \frac{1}{2} \int_{\Lambda_k} r_d^2 + \delta_r^2 \left(\cos^2(\lambda - \kappa) - \sin^2(\lambda - \kappa)\right) \\ &\qquad + 2\delta_r \cos(\lambda - \kappa) \sqrt{r_d^2 - \delta_r^2 \sin^2(\lambda - \kappa)}\, d\lambda - \left(\frac{\pi}{4} r_i^2 + a_x\right) \end{aligned} \tag{5.5}$$

where r_i is the radius of the inner annulus formed from the outboard electrodes and a_x is the area of the annular segment absent in the electrode pattern. The integral bounds are

$$\Lambda_k = \left[\frac{3\pi}{4}, \frac{5\pi}{4}\right] + \frac{\pi}{2}(k-5), \quad k = 5, \ldots, 8.$$

Evaluating the integral in 5.5

$$\begin{aligned} A_{l,k}(x,y) &= \frac{1}{2} \int_{\Lambda_k} r_d^2 + \delta_r^2 \left(\cos^2(\lambda - \kappa) - \sin^2(\lambda - \kappa)\right) \\ &\qquad + 2\delta_r \cos(\lambda - \kappa) \sqrt{r_d^2 - \delta_r^2 \sin^2(\lambda - \kappa)}\, d\lambda - \left(\frac{\pi}{4} r_i^2 + a_x\right) \\ &= \frac{\pi}{4} r_d^2 + \frac{1}{4} \delta_r^2 \left(\sin 2\left(\frac{5\pi}{4} + \frac{\pi}{2}(k-5) - \kappa\right) - \sin 2\left(\frac{3\pi}{4} + \frac{\pi}{2}(k-5) - \kappa\right)\right) \\ &\quad + \delta_r \int_{\Lambda_k} \cos(\lambda - \kappa) \sqrt{r_d^2 - \delta_r^2 \sin^2(\lambda - \kappa)}\, d\lambda - \left(\frac{\pi}{4} r_i^2 + a_x\right) \end{aligned} \tag{5.6}$$

Depending on the perturbation in either x or y, the area calculation may be simplified even further. In fact, for perturbations perpendicular to the axis of symmetry for a given electrode have a negligible influence on the change in area. To illustrate, consider Eq. 5.6 for $k = 5$ with a perturbation solely in y with $y << r_d$. In which case, $\kappa = \frac{\pi}{2}$ and $\delta_r = y$.

Eq. 5.6 becomes

$$A_{l,5}(x,y) = \frac{\pi}{4}r_d^2 + \frac{1}{4}y^2\left(\sin\frac{3\pi}{2} - \sin\frac{\pi}{2}\right) + y\int_{\Lambda_5}\cos\left(\lambda - \frac{\pi}{2}\right)\sqrt{r_d^2 - y^2\sin^2\left(\lambda - \frac{\pi}{2}\right)}\,d\lambda - \left(\frac{\pi}{4}r_i^2 + a_x\right) \tag{5.7}$$

$$= \frac{\pi}{4}r_d^2 - \frac{1}{2}y^2 + y\int_{\Lambda_5}\sin\lambda\sqrt{r_d^2 - y^2\cos^2\lambda}\,d\lambda - \left(\frac{\pi}{4}r_i^2 + a_x\right). \tag{5.8}$$

For the integral in Eq. 5.8,

$$y\int_{\Lambda_5}\sin\lambda\sqrt{r_d^2 + y^2\cos^2\lambda}\,d\lambda = -\left(\frac{y}{2}\cos\lambda\sqrt{r_d^2 - y^2\cos^2\lambda} + \cdots \frac{r_d^2}{2}\tan^{-1}\left(\frac{y\cos\lambda}{\sqrt{r_d^2 - y^2\cos^2\lambda}}\right)\right)\Bigg|_{\frac{3\pi}{4}}^{\frac{5\pi}{4}}$$

$$= 0$$

since $\cos\frac{5\pi}{4} = \cos\frac{3\pi}{4}$. Since $y << r_d$, y^2 may be regarded as approximately zero, reducing Eq. 5.8 to

$$A_{l,5}(x,y) = \frac{\pi}{4}r_d^2 - \left(\frac{\pi}{4}r_i^2 + a_x\right). \tag{5.9}$$

Fig. 5.6 shows a comparison of the capacitance in C_5, resulting from a displacement in y, produced by the exact area computation in Eq. 5.8 versus the estimate in Eq. 5.9. From this figure, it is quite evident small displacements in the y-direction have an insignificant affect on the overall capacitance.

A similar argument can be made for $k = 7$, implying the area calculations for C_5 and C_7 are affected by small changes in y in a negligible fashion. An analogous approximation can be made for $A_{l,6}(x,y)$ and $A_{l,8}(x,y)$ under perturbations in x due to the symmetry of the electrodes. Therefore, the $A_{l,5}(x,y) = A_{l,5}(x)$, $A_{l,6}(x,y) = A_{l,6}(y)$, $A_{l,7}(x,y) = A_{l,7}(x)$, and $A_{l,8}(x,y) = A_{l,8}(y)$. In the cases $k = 5, 7$, $\kappa = 0$ (making $\delta_r = x$) and, after discarding

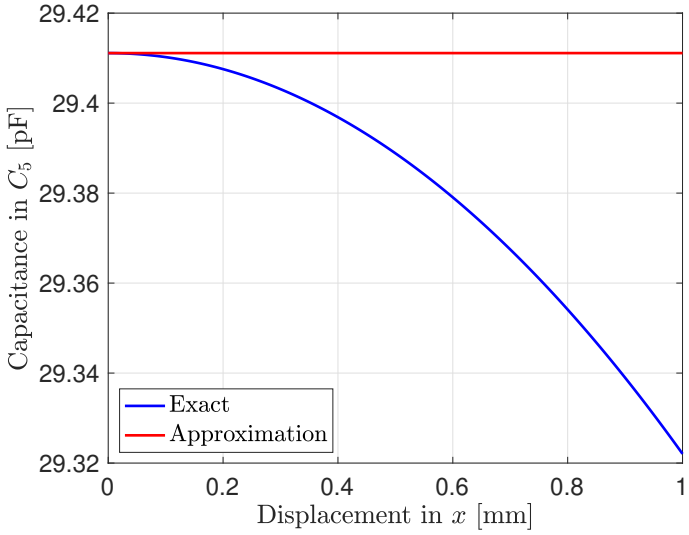

Figure 5.6: Comparison of the capacitance of C_5 when the disk is displaced in the y-direction by up to 1mm. The difference in the exact capacitance versus the approximation is roughly 0.3% when the disk is displaced by 1mm.

$\delta_r^2 = x^2$ under the context of small perturbations in x, Eq. 5.6 becomes

$$\begin{aligned} A_{l,k}(x) &\approx \frac{\pi}{4} r_d^2 - \left(\frac{\pi}{4} r_i^2 + a_x\right) + x r_d \int_{\Lambda_k} \cos\lambda \, d\lambda \\ &= \frac{\pi}{4} r_d^2 - \left(\frac{\pi}{4} r_i^2 + a_x\right) + x r_d \sin\lambda \Big|_{\Lambda_k} \\ &= \frac{\pi}{4} r_d^2 - \left(\frac{\pi}{4} r_i^2 + a_x\right) + (-1)^{\frac{k-5}{2}} x r_d \sqrt{2} \end{aligned} \tag{5.10}$$

An expression for the other two cases can be found similarly. For $k = 6, 8$ and $\kappa = \frac{\pi}{2}$, $\delta_r = y$ and Eq. 5.6 is used to compute

$$\begin{aligned} A_{l,k}(y) &\approx \frac{\pi}{4} r_d^2 - \left(\frac{\pi}{4} r_i^2 + a_x\right) + y r_d \int_{\Lambda_k} \sin\lambda \, d\lambda \\ &= \frac{\pi}{4} r_d^2 - \left(\frac{\pi}{4} r_i^2 + a_x\right) - y r_d \cos\lambda \Big|_{\Lambda_k} \\ &= \frac{\pi}{4} r_d^2 - \left(\frac{\pi}{4} r_i^2 + a_x\right) - (-1)^{\frac{k-6}{2}} y r_d \sqrt{2} \end{aligned} \tag{5.11}$$

Figure 5.7 illustrates the magnitude of the voltage drop across the secondary of the transformer used to detect lateral motions. In this figure, the capacitance is computed on the

basis of Eq. 5.3 ($k = 5, 7$) over a range of perturbation values for z and y in Eq. 5.1 with $x = \varphi = \theta = 0$. The center tap current is fixed and sets the threshold of values the secondary will exhibit. A bias persists in the measurement due to non-idealities present in the transformers and is removed. This figure shows the dominance of the measured signal due to perturbations in y over those due to z. The results for $r_0\varphi$ for the same range of perturbations is the same as that for z. Since the area in the capacitance equation is the primary modified by changes in y, this figure illustrates how the differential capacitance change resulting in such perturbations is presented through the transformer secondary. These signals can ultimately be used to drive the disk laterally back to the nominal position.

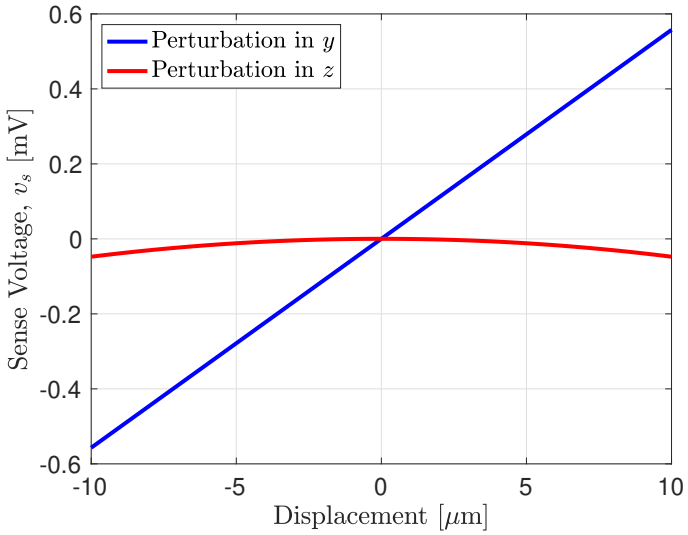

Figure 5.7: Comparison of voltage drop across the secondary of transformers used to detect lateral motion. Vertical translations in z from a range of -10μm to 10μm produce no more than $50\mu V$ on the secondary due to any developed differential capacitance. By comparison, perturbations in y over the same range are detected by about $58mV$/mm. Bias due to parasitics have been removed.

Regarding the electrostatic forces developed by the outboard electrodes, their configuration and magnitude have a negligible affect on the disk's dynamics near the equilibrium condition. As mentioned, these electrodes are not biased by any form of a control voltage and therefore their potential is only dictated by the potential established by the center-tap current and capacitance. The capacitance between any outboard electrode and the disk

(in the equilibrium configuration) is roughly 29.41pF as compared to 91.78pF of capacitance between any of the primary electrodes and the disk. Further, the center-tap current is set to a level much lower than that of the transformers connected to the primary electrode pairs. These two facts lead to a voltage produced on the outboard electrodes that is roughly 15% that of the primary electrodes. In addition, the outboard electrodes $\mathcal{E}_k$ and $\mathcal{E}_{1k}$ are tied together (for $k = 5, \ldots, 8$). This fact means that, again, near the equilibrium condition, the net electrostatic forces and torques originating from the outboard electrodes $\mathcal{E}_k$ and $\mathcal{E}_{1k}$ cancel each other capacitances are the same and the voltages would be nearly equal, the presence of parasitics in the transformer preventing this ideal condition. In fact, with the measured parasitics included in the model, the force produced by $\mathcal{E}_k$ differs from that of $\mathcal{E}_{1k}$ by about 2.5%. For the equilibrium condition in Eq. 5.33, the force magnitude from a given outboard electrode (with a potential set to be 20% of the potentials of the primary electrodes) is about 1% of the force magnitude of any given primary electrode underneath the disk (which has a smaller potential due to the control voltage bias). Due to these circumstances, the forces and torques produced by the outboard electrodes is not included in any of the analysis.

5.3 Plant Model and Analysis

The suspended disk dynamics and the circuit equations are coupled by the electrode-disk capacitances and corresponding electrostatic forces. The following are assumed in deriving the equations of motion:

1. The electrostatic forces exerted on the disk by the lateral electrodes are neglected. These electrodes are significantly smaller than the primary electrodes and are operated at lower potentials.

2. The disk is assumed to be *thin* in the sense that the top and bottom surfaces of the disk coincide with the center-plane of the disk. Thus, calculation of electrode-disk

gaps is determined by the deflection of disk center plane.

3. The electrode-disk capacitances are defined using a simple parallel plate model in which the plate separation is taken to be the electrode-disk distance measured normally from the centroid of the electrode to the disk surface.

4. The electrostatic forces exerted on the plate are computed using the same parallel plate model as the capacitances.

5. Small-angle approximates are applied in the conclusion of deriving the generalized force components. The expressions for the generalized forces are difficult to parse and any insight to the physical system is lost without this simplification.

These assumptions are quite reasonable since the disk is constrained to very small rotations and is indeed a thin body. The disk dynamics are linearized once an equilibrium point for the disk and electrode equations is established so that a linear, time-invariant model is available for analysis and control design.

5.3.1 Disk Kinematic Relations

The disk kinematics are parameterized by $\{x, y, z\}$ and the Euler angles $\{\varphi, \theta\}$. Yaw motion is ignored. Fig. 5.2 shows the arrangement of the electrodes, the location of the electrostatic forces on the disk from the primary electrodes, and defines the coordinate system. The figure is reproduced for convenience. In Fig. 5.2, the origin of the inertial reference frame (denoted with N_1, N_2, and N_3) is fixed at the nominal location of the disk geometric center (which is assumed to coincide with the disk center of mass). At the nominal location, the disks' faces are in parallel with the electrodes and centered in-between the two sets (thus the gap is uniform and equal on either side of the disk). The N_3-axis extends normal to the surface of the disk where as the N_1-axis extends (positively) along the axis of symmetry for electrode $\mathcal{E}_3$ and, similarly, the N_2-axis along the axis of symmetry of $\mathcal{E}_4$. Due to the configuration of the electrodes, the planar axes N_1 and N_2 are orthogonal. A

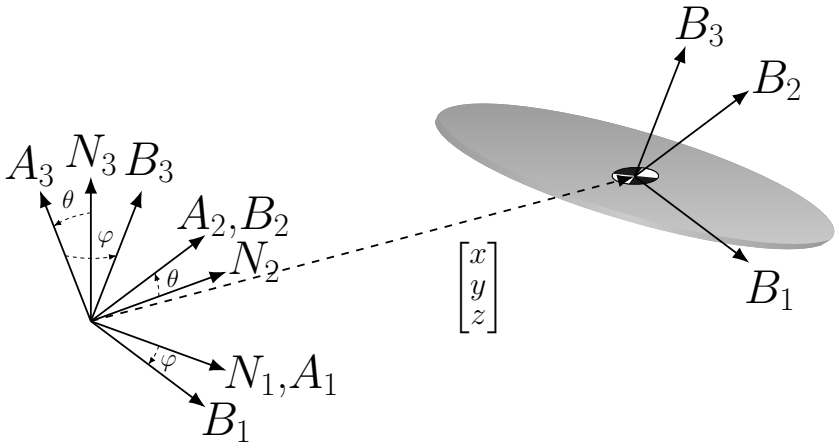

Figure 5.8: Coordinate system use to define the kinematic relationships.

body-fixed frame (denoted B_1, B_2, and B_3) also has its origin fixed at the disk center of mass and is coincident with the inertial frame when the disk is in the nominal configuration, –see Fig. 5.8. Unit vectors in the inertial frame are expressed as $\underline{n}_1$, $\underline{n}_2$, and $\underline{n}_3$ to correspond with the principal axes N_1, N_2, and N_3, respectively. Similarly, body frame unit vectors $\underline{b}_1$, $\underline{b}_2$, and $\underline{b}_3$ correspond to the principal axes B_1, B_2, and B_3, respectively. An Euler angle sequence is used to describe the disk's orientation and relationship between the frames' unit vectors. Under the assumption the sequence first rotates about θ (in the inertial frame) followed by φ (in the body frame), the transformation matrix from the body orientation to the inertial frame is

$$\begin{bmatrix} \underline{n}_1 \\ \underline{n}_2 \\ \underline{n}_3 \end{bmatrix} = \begin{bmatrix} \cos\varphi & 0 & \sin\varphi \\ \sin\varphi\sin\theta & \cos\theta & -\cos\varphi\sin\theta \\ -\sin\varphi\cos\theta & \sin\theta & \cos\varphi\cos\theta \end{bmatrix} \begin{bmatrix} \underline{b}_1 \\ \underline{b}_2 \\ \underline{b}_3 \end{bmatrix}. \tag{5.12}$$

Using the unit vector notation, any point on the disk in the inertial frame may then be described by

$$\underline{r}_p = (x\,\underline{n}_1 + y\,\underline{n}_2 + z\,\underline{n}_3) + x_b\,\underline{b}_1 + y_b\,\underline{b}_2 + z_b\,\underline{b}_3 = \underline{r}_{\rm cm} + x_b\,\underline{b}_1 + y_b\,\underline{b}_2 + z_b\,\underline{b}_3$$

where x, y, and z are scalar values associated with the location of the disk center of mass in the inertial frame, indicated by $\underline{n}_1$, $\underline{n}_2$, and $\underline{n}_3$, and x_p, y_p, z_p are scalars indicative of a point on the disk in the body-frame, as indicated by the unit vectors $\underline{b}_1$, $\underline{b}_2$, and $\underline{b}_3$. To compute capacitances and electrostatic forces, electrode-disk gaps must be defined. The *change* in an electrode-disk gap when the disk is not in its equilibrium configuration is determined by computing the $\underline{n}_3$-displacement of the disk plane (defined by the B_1-B_2 plane) from the N_1-N_2 plane along the line through the centroids of paired electrodes –see Fig. 5.9. A positive change in gap is defined when the electrode centroid projected onto the B_1-B_2 plane is displaced in a positive $\underline{n}_3$ sense relative to the N_1-N_2 plane. There is only one gap change defined for a given set of paired electrodes In the body frame, the geometric centers of each electrode projected on to the disk (including translations of the center of mass) are

$$\begin{aligned} \underline{r}_1 &= \underline{r}_{\text{cm}} - \frac{(r_0+x)}{\cos\varphi}\underline{b}_1 - \frac{y}{\cos\theta}\underline{b}_2 \quad \underline{r}_3 = \underline{r}_{\text{cm}} + \frac{(r_0-x)}{\cos\varphi}\underline{b}_1 - \frac{y}{\cos\theta}\underline{b}_2 \\ \underline{r}_2 &= \underline{r}_{\text{cm}} - \frac{x}{\cos\varphi}\underline{b}_1 - \frac{(r_0+y)}{\cos\theta}\underline{b}_2 \quad \underline{r}_4 = \underline{r}_{\text{cm}} - \frac{x}{\cos\varphi}\underline{b}_1 + \frac{(r_0-y)}{\cos\theta}\underline{b}_2 \end{aligned} \tag{5.13}$$

where r_0 represents the radius of a circle in the electrode plane that interpolates the primary electrodes' centroids. Using the transformation between frames in Eq. 5.12, these vectors can be expressed in the inertial frame as

$$\begin{aligned} \underline{r}_1 &= -r_0\,\underline{n}_1 - (r_0+x)\tan\varphi\sin\theta\,\underline{n}_2 + (z+(r_0+x)\tan\varphi\cos\theta - y\tan\theta)\;\underline{n}_3 \\ \underline{r}_2 &= -(r_0 + x\tan\varphi\sin\theta)\;\underline{n}_2 + (z + x\tan\varphi\cos\theta - (r_0+y)\tan\theta)\;\underline{n}_3 \\ \underline{r}_3 &= \quad r_0\,\underline{n}_1 + (r_0-x)\tan\varphi\sin\theta\,\underline{n}_2 + (z-(r_0-x)\tan\varphi\cos\theta - y\tan\theta)\;\underline{n}_3 \\ \underline{r}_4 &= \quad (r_0 - x\tan\varphi\sin\theta)\;\underline{n}_2 + (z + x\tan\varphi\cos\theta + (r_0-y)\tan\theta)\;\underline{n}_3. \end{aligned} \tag{5.14}$$

The changes in the electrode-disk gap due to a change in the disk's position and orientation are then computed as

$$\begin{aligned} z_1 &= \underline{r}_1 \cdot \underline{n}_3 = z + (r_0 + x)\tan\varphi\cos\theta - y\tan\theta \\ z_2 &= \underline{r}_2 \cdot \underline{n}_3 = z - (r_0 + y)\tan\theta + x\tan\varphi\cos\theta \\ z_3 &= \underline{r}_3 \cdot \underline{n}_3 = z - (r_0 - x)\tan\varphi\cos\theta - y\tan\theta \\ z_4 &= \underline{r}_4 \cdot \underline{n}_3 = z + (r_0 - y)\tan\theta + x\tan\varphi\cos\theta. \end{aligned} \tag{5.15}$$

When the disk is in its nominal configuration (the inertial and body frame are coincident and the gap is uniform between the disk and electrode sets), the electrode-disk gap is $z_0 = 134\,\mu$m. Thus, the $\mathcal{E}_1$-disk gap is given by $z_0 - z_1$, the $\mathcal{E}_{11}$-disk gap is given by $z_0 + z_1$, the $\mathcal{E}_2$-disk gap is given by $z_0 - z_2$, and so forth. The kinematic variables describing the disk orientation are gather in the vector

$$q = [x, y, z, \theta, \varphi]^T .$$

5.3.2 Nonlinear Equations of Motion

The dynamics of the suspended disk and the circuit equations are coupled by the capacitance which develops between the disk and the surrounding electrodes. As the disk translates vertically, the gaps between the primary electrodes and the disk creates a differential capacitance change between all of the electrode pairs. Similarly, angular rotations (roll and pitch) about a principal axis causes a capacitance change in the primary electrodes aligned with the complementary orthogonal axis. Lateral translation can be detected through a capacitance change in the outboard electrodes. Conversely, any potential supplied on the electrodes generates an electrostatic force on the disk.

The geometry of this system prescribes very small angular deflections and, therefore, representing the capacitance via a parallel plate model is adequate. The capacitance between a

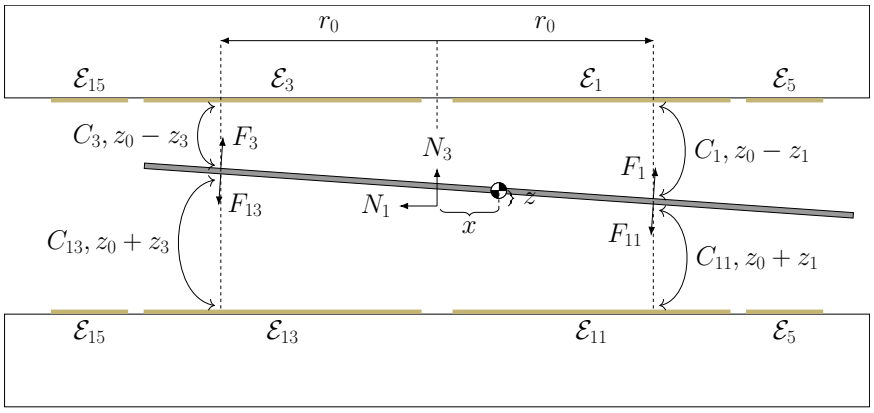

View down N_2-axis

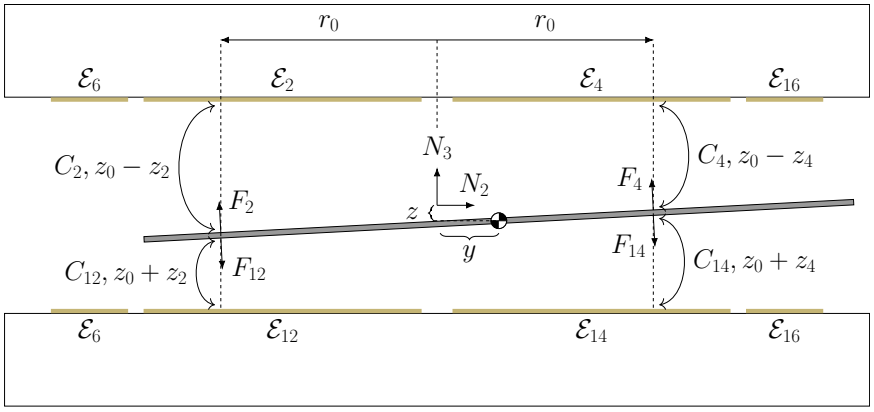

View down N_1-axis

Figure 5.9: Side views of the disk in relation to the electrode configuration (not to scale).

primary electrode and the disk is given by

$$C_k(q) = \frac{\epsilon_0 \epsilon_r A_p}{z_0 - z_k} \quad k = 1, \ldots, 4 \tag{5.16}$$

$$C_{1k}(q) = \frac{\epsilon_0 \epsilon_r A_p}{z_0 + z_k} \quad k = 1, \ldots, 4 \tag{5.17}$$

where A_p represents the projected electrode area on to the disk, $z_0 = 134\mu$m is the nominal gap, z_k is N_3 coordinate derived in Eq. 5.15. The area is fixed since it is assumed the disk is always interposed between the electrodes, i.e. the electrodes in a primary pair are never exposed to each other. The electrostatic forces are replaced with point forces denoted $\{\underline{F}_1, \ldots, \underline{F}_4\}$ for the top electrode set and $\{\underline{F}_{11}, \ldots, \underline{F}_{14}\}$ for the bottom electrode set (refer to Figs. 5.2 and 5.9). The magnitude of these forces are indicated in the same

manner, however, the vector notation is dropped, eg., F_1 represents the magnitude of $\underline{F}_1$. Despite the fact that a parallel plate model is used to determine the magnitude of the electrostatic forces, the point forces act normal to disk surface since the disk is assumed to be an equipotential body. Thus, when the B_1-B_2 is not coplanar with N_1-N_2, forces in the $\underline{n}_1$ and $\underline{n}_2$ directions are developed from the electrostatic forces.

The magnitudes of the electrostatic forces associated with a given primary electrode pair $\mathcal{E}_k$ and $\mathcal{E}_{1k}$ are computed assuming a parallel plate capacitance model using the principle of virtual work with respect to a perturbation in z_k. The total energy in any given electrode is

$$W_k = \frac{1}{2} C_k(q) v_k^2 = \frac{1}{2} \frac{\mathfrak{q}_k^2}{C_k(q)}$$

where v_k is the voltage on electrode $\mathcal{E}_k$ and $\mathfrak{q}_k = C_k v_k$ is the charge. Assuming $\mathfrak{q}_k$ is constant with respect to z_k, the electrostatic force for a given electrode pair may be computed as

$$\begin{aligned} F_k &= -\frac{\partial}{\partial z_k}\left(\frac{1}{2}\frac{\mathfrak{q}_k^2}{C_k(q)}\right) & F_{1k} &= -\frac{\partial}{\partial z_k}\left(\frac{1}{2}\frac{\mathfrak{q}_{1k}^2}{C_{1k}(q)}\right) \\ &= \frac{1}{2}\frac{\mathfrak{q}_k^2}{C_k^2(q)}\frac{\partial}{\partial z_k}C_k(q) & &= \frac{1}{2}\frac{\mathfrak{q}_{1k}^2}{C_{1k}^2(q)}\frac{\partial}{\partial z_k}C_{1k}(q) \\ &= \frac{1}{2}v_k^2\frac{\partial}{\partial z_k}C_k(q) & &= \frac{1}{2}v_{1k}^2\frac{\partial}{\partial z_k}C_{1k}(q) \\ &= \frac{\epsilon_0\epsilon_r A_p}{2(z_0 - z_k)^2}v_k^2 & &= -\frac{\epsilon_0\epsilon_r A_p}{2(z_0 + z_k)^2}v_{1k}^2. \end{aligned} \tag{5.18}$$

For further simplification, the outboard electrodes, which are used to detect and lateral translation, are ignored in the force calculations due to the fact that their relative capacitance and arrangement have a negligible effect on the forces. As a vector, the electrostatic forces are defined to be

$$\begin{aligned} \underline{F}_k &= F_k \underline{b}_3 = F_k\left(\sin\varphi\,\underline{n}_1 - \cos\varphi\sin\theta\,\underline{n}_2 + \cos\varphi\cos\theta\,\underline{n}_3\right) \\ \underline{F}_{1k} &= F_{1k}\underline{b}_3 = F_{1k}\left(\sin\varphi\,\underline{n}_1 - \cos\varphi\sin\theta\,\underline{n}_2 + \cos\varphi\cos\theta\,\underline{n}_3\right). \end{aligned} \tag{5.19}$$

Deriving the equations of motion for the disk may easily be formulated via Lagrange's

equations

$$\frac{d}{dt}\left(\frac{\partial L}{\partial \dot{q}_j}\right) - \frac{\partial L}{\partial q_j} = Q_j \tag{5.20}$$

where $L = T - V$, with T and V representing the kinetic and potential energy, respectively, of the disk and Q_j represents the generalized force for the element $q_j \in q$. From the prescribed Euler angle sequence, the angular velocity of the disk is found as

$$\Omega = \left[\dot{\theta}\cos\varphi,\ \dot{\varphi},\ \dot{\theta}\sin\varphi\right]^T. \tag{5.21}$$

The kinetic energy of the disk is described by

$$T = \frac{1}{2}m(\dot{x}^2 + \dot{y}^2 + \dot{z}^2) + \frac{1}{2}\Omega^T J \Omega \tag{5.22}$$

where $J = \mathrm{diag}(J_{xy}, J_{xy}, J_z)$ is the inertia matrix. Lastly, the potential energy of disk is simply the gravitational potential

$$V = mgz. \tag{5.23}$$

From Eqs. 5.21–5.23, the Lagrangian, L, in Eq. 5.20 becomes

$$L = \frac{1}{2}m(\dot{x}^2 + \dot{y}^2 + \dot{z}^2) + \frac{1}{2}\left(J_{xy}\dot{\theta}^2\cos^2\varphi + J_{xy}\dot{\varphi}^2 + J_z\dot{\theta}^2\sin^2\varphi\right) - mgz. \tag{5.24}$$

Application of Eq. 5.20 using Eq. 5.24 yields the equations of motion for the disk

$$\begin{aligned}
&m\ddot{x} = Q_x \\
&m\ddot{y} = Q_y \\
&m\ddot{z} + mg = Q_z - c_z\dot{z} \\
&(J_{xy}\cos^2\varphi + J_z\sin^2\varphi)\ddot{\theta} + \dot{\varphi}\sin(2\varphi)(J_z - J_{xy})\dot{\theta} = Q_\theta - c_\theta\dot{\theta} \\
&J_{xy}\ddot{\varphi} + \frac{1}{2}\sin(2\varphi)(J_{xy} - J_z)\dot{\theta}^2 = Q_\varphi - c_\varphi\dot{\varphi}
\end{aligned} \tag{5.25}$$

where the generalized force Q_j constitute the electrostatic forces. Squeeze-film damping between the disk and the electrodes is included as a non-conservative force. These estimation

for these parameters are taken from [BY07].

The generalized forces Q_j are defined by

$$Q_j = \sum_{k=1}^{4} (\underline{F}_k + \underline{F}_{1k}) \cdot \frac{\partial \underline{e}_k}{\partial q_j}.$$

It is crucial to note that this calculation must be done in the inertial frame. From Eqs. 5.14 and 5.19, the generalized forces as defined by above are

$$\begin{aligned}
Q_x =& \tan\varphi \cos\varphi \frac{\epsilon_0 \epsilon_r A_p}{2} \sum_{k=1}^{4} \left\{ \frac{v_k^2}{(z_0 - z_k)^2} - \frac{v_{1k}^2}{(z_0 + z_k)^2} \right\} \\
Q_y =& -\sin\theta \cos\varphi \frac{\epsilon_0 \epsilon_r A_p}{2} \sum_{k=1}^{4} \left\{ \frac{v_k^2}{(z_0 - z_k)^2} - \frac{v_{1k}^2}{(z_0 + z_k)^2} \right\} \\
Q_z =& \cos\varphi \cos\theta \frac{\epsilon_0 \epsilon_r A_p}{2} \sum_{k=1}^{4} \left\{ \frac{v_k^2}{(z_0 - z_k)^2} - \frac{v_{1k}^2}{(z_0 + z_k)^2} \right\} \\
Q_\theta =& \frac{\epsilon_0 \epsilon_r A_p}{2} \Bigg[-y \sec\theta \cos\varphi \sum_{k=1,3} \left\{ \frac{v_k^2}{(z_0 - z_k)^2} - \frac{v_{1k}^2}{(z_0 + z_k)^2} \right\} \\
&+ \sum_{k=2,4} \left\{ \left(-y + (-1)^{\frac{k}{2}} r_0 \right) \sec\theta \cos\varphi \right\} \left\{ \frac{v_k^2}{(z_0 - z_k)^2} - \frac{v_{1k}^2}{(z_0 + z_k)^2} \right\} \Bigg] \\
Q_\varphi =& \frac{\epsilon_0 \epsilon_r A_p}{2} \Bigg[\sum_{k=1,3} (x + (-1)^{\frac{k-1}{2}} r_0) \sec\varphi \left\{ \frac{v_k^2}{(z_0 - z_k)^2} - \frac{v_{1k}^2}{(z_0 + z_k)^2} \right\} \\
&+ x \sec\varphi \sum_{k=2,4} \left\{ \frac{v_k^2}{(z_0 - z_k)^2} - \frac{v_{1k}^2}{(z_0 + z_k)^2} \right\} \Bigg].
\end{aligned} \tag{5.26}$$

Not much can be readily drawn from Eq. 5.26. However, by invoking the assumption that the angular deflections are small, this set of equations can be greatly simplified,

$$
\begin{aligned}
Q_x &= \varphi \frac{\epsilon_0 \epsilon_r A_p}{2} \sum_{k=1}^{4} \left\{ \frac{v_k^2}{(z_0 - z_k)^2} - \frac{v_{1k}^2}{(z_0 + z_k)^2} \right\} \\
Q_y &= -\theta \frac{\epsilon_0 \epsilon_r A_p}{2} \sum_{k=1}^{4} \left\{ \frac{v_k^2}{(z_0 - z_k)^2} - \frac{v_{1k}^2}{(z_0 + z_k)^2} \right\} \\
Q_z &= \frac{\epsilon_0 \epsilon_r A_p}{2} \sum_{k=1}^{4} \left\{ \frac{v_k^2}{(z_0 - z_k)^2} - \frac{v_{1k}^2}{(z_0 + z_k)^2} \right\} \\
Q_\theta &= \frac{\epsilon_0 \epsilon_r A_p}{2} \left[-y \sum_{k=1,3} \left\{ \frac{v_k^2}{(z_0 - z_k)^2} - \frac{v_{1k}^2}{(z_0 + z_k)^2} \right\} \right. \\
&\quad \left. + \sum_{k=2,4} \left(-y + (-1)^{\frac{k}{2}} r_0 \right) \left\{ \frac{v_k^2}{(z_0 - z_k)^2} - \frac{v_{1k}^2}{(z_0 + z_k)^2} \right\} \right] \\
Q_\varphi &= \frac{\epsilon_0 \epsilon_r A_p}{2} \left[\sum_{k=1,3} \left(x + (-1)^{\frac{k-1}{2}} r_0 \right) \left\{ \frac{v_k^2}{(z_0 - z_k)^2} - \frac{v_{1k}^2}{(z_0 + z_k)^2} \right\} \right. \\
&\quad \left. + x \sum_{k=2,4} \left\{ \frac{v_k^2}{(z_0 - z_k)^2} - \frac{v_{1k}^2}{(z_0 + z_k)^2} \right\} \right].
\end{aligned}
\tag{5.27}
$$

The equations in Eq. 5.27 reflect a number of simple physical principles. First, the vertical force is composed entirely of the net sum of the standard electrostatic force developed for a parallel plate model. Second, the moments are directly moments one could compute using the parallel plate electrostatic force times the corresponding moment arm. This is as simple as computing the moments given a free-body diagram of Fig. 5.2. Lastly, and most significantly, the lateral forces which develop are directly shown to be dependent on the tilts in θ and φ. The fact that motion in x and y is coupled exclusively to motion in θ and φ, respectively, is a consequence of decoupling the rotations using the small angle linearization, making the Euler-angle sequence commutable. One major implication of this realization is that the lateral motion of the disk may be regulated through intentional manipulation of the electrostatic forces responsible for tilting the disk. This realization will be exploited later to actively control the lateral motion of the disk. The disk equations

in Eq. 5.25 and 5.27 can be represented as first-order ODEs in the form

$$\frac{d}{dt}\begin{bmatrix} q \\ \dot{q} \end{bmatrix} = \begin{bmatrix} \dot{q} \\ f_q(q, \dot{q}, w) \end{bmatrix} \tag{5.28}$$

where $f_q(q, \dot{q}, w) \in \mathbf{R}^5$ represent the accelerations when solving for each $\ddot{q}_k$ in Eq. 5.25.

5.3.3 Electrical Subsystem Equations

The dynamics of the suspended disk and the transformers are coupled by the capacitance which develops between the disk and the surrounding electrodes. For the 5-DOF system seen in Fig. 5.2, there are total of four pairs of electrodes used for sensing and actively controlling the disk motion. These electrodes are paired based on the masking of the upper electrode set over the lower set (Fig. 5.1). The enumeration of the electrodes lend intuition to this notion. As seen in Fig. 5.2, the upper electrode set is enumerated 1–8 while the lower set is enumerated 11–18. The electrode labeled $\mathcal{E}_k$ overlays $\mathcal{E}_{1k}$ when the system is assembled and the two are consequently paired via the transformer leads. Figure 5.10 shows a schematic to clarify how the transduction transformers are connected to the electrodes in Fig. 5.2. The equations of motion for the transformer performing the

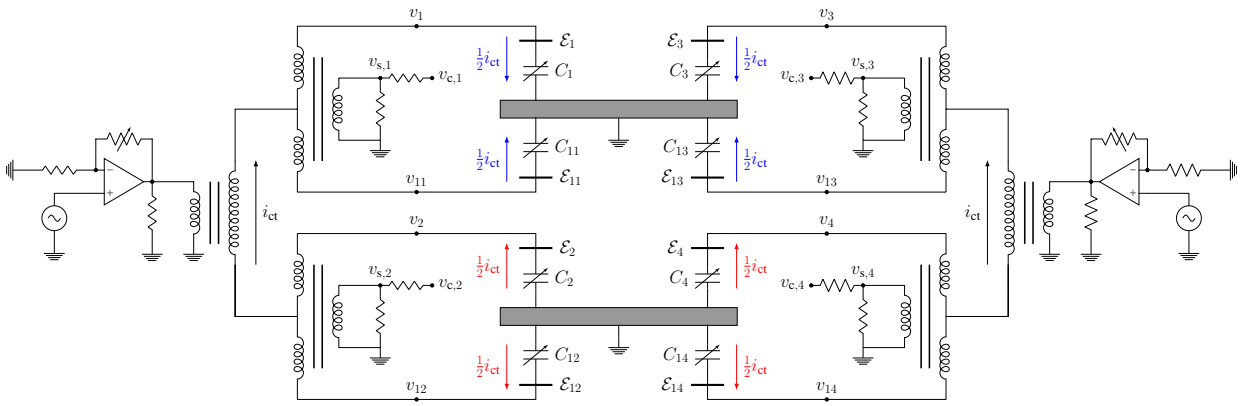

Figure 5.10: Circuit schematic illustrating the connection of the transformers to the electrodes and the corresponding capacitances which develop between the electrodes and disk as a result. Directions of the center tap current illustrate how the disk is neutrally charged.

transduction was previously (1.2) consolidated into the state-space formulation

$$M(q)\dot{w} = Aw + B_1 i_{\mathrm{ct}} + B_2 v_{\mathrm{c}} \tag{5.29}$$

where $q = [x, y, z, \theta, \varphi]^T$. Within this model, a pair of electrodes constitutes the capacitances wrapped in the mass matrix M. Each of these transformer-electrode groupings may be modeled with Eq. 5.29. Since the center taps of the transduction transformers are connected via the supply transformer, feedthrough from a control voltage on one transduction transformer to the voltage drop across the secondary of the adjacent transduction transformer also exists in addition to the more direct feedthrough addressed in previous chapters. By supplying a control voltage on one transduction transformer, current is pumped into the secondary which in turn produces a change in the current on the primary side. Such a change in the transduction transformer's primary side current would make its way to the second transduction transformer through the supply transformer. This would have a tendency to produce a voltage drop on the adjacent transduction transformer's secondary, thereby obscuring voltage measurements due to disk motion. A rudimentary analysis of this feedthrough, however, shows the center taps are relatively unaffected by the addition of a control voltage. As such, the transformer subsystems are considered to be decoupled and are represented by the set of equations

$$\begin{aligned} M_k(q)\,\dot{w}_k(t) &= A_k w_k(t) + B_{1j} i_{\mathrm{ct},k}(t) + B_{2j} v_{\mathrm{c},k}(t), \quad k = 1,2,3,4 \\ M_k(q)\,\dot{w}_k(t) &= A_k w_k(t) + B_{1j} i_{\mathrm{ct},k}(t), \qquad\qquad k = 5,6 \\ v_{\mathrm{s},k}(t) &= J_k w_k(t), \qquad\qquad \forall k \end{aligned} \tag{5.30}$$

where the subscript k in the equations coincides with the electrode pair $\mathcal{E}_k/\mathcal{E}_{1k}$, $M_k \in \boldsymbol{R}^{19\times 19}$, $A_k \in \boldsymbol{R}^{19\times 19}$, $B_{1k} \in \boldsymbol{R}^{19}$, $B_{2k} \in \boldsymbol{R}^{19}$, and $J_k \in \boldsymbol{R}^{1\times 19}$ is the vector which picks off the element of w_k corresponding to the sense voltage $v_{\mathrm{s},k}$. Essentially, each J_k is a vector of zeros with a single entry equal to one, its entry location corresponding the the location of $v_{\mathrm{s},k}$ in w_k. As a consequence of the model assumptions, $i_{\mathrm{ct},j} = -i_{\mathrm{ct},j-1}$ for $j = 2, 4$. The

subsystems in Eq. 5.30 may be synthesized into a single state-space representation:

$$\begin{aligned} M(q)\dot{w} &= Aw + B_1 i_{\mathrm{ct}} + B_2 v_{\mathrm{c}} \\ v_{\mathrm{s}} &= Jw \end{aligned} \tag{5.31}$$

where w, i_{ct}, the vector of amplitude-modulated voltages v_{c}, and the vector of pick-off voltages v_{s} are defined as

$$w = \begin{bmatrix} w_1 \\ \vdots \\ w_6 \end{bmatrix} \quad i_{\mathrm{ct}} = \begin{bmatrix} i_{\mathrm{ct},1} \\ \vdots \\ i_{\mathrm{ct},6} \end{bmatrix} \quad v_{\mathrm{c}} = \begin{bmatrix} v_{\mathrm{c},1} \\ \vdots \\ v_{\mathrm{c},4} \end{bmatrix} \quad v_{\mathrm{s}} = \begin{bmatrix} v_{\mathrm{s},1} \\ \vdots \\ v_{\mathrm{s},6} \end{bmatrix}$$

Further,

$$M(q) = \begin{bmatrix} M_1 & & \\ & \ddots & \\ & & M_6 \end{bmatrix} \in \boldsymbol{R}^{114\times 114} \qquad A = \begin{bmatrix} A_1 & & \\ & \ddots & \\ & & A_6 \end{bmatrix} \in \boldsymbol{R}^{114\times 114}$$

$$B_1 = \begin{bmatrix} B_{11} \\ B_{12} \\ B_{13} \\ B_{14} \\ B_{15} \\ B_{16} \end{bmatrix} \in \boldsymbol{R}^{114\times 6} \qquad B_2 = \left[\begin{array}{cccc} B_{21} & 0 & 0 & 0 \\ 0 & B_{22} & 0 & 0 \\ 0 & 0 & B_{23} & 0 \\ 0 & 0 & 0 & B_{24} \\ \hline & & 0 & \end{array}\right] \in \boldsymbol{R}^{114\times 4}.$$

$$J = \begin{bmatrix} J_1 & & \\ & \ddots & \\ & & J_6 \end{bmatrix} \in \boldsymbol{R}^{6\times 114}.$$

The full plant model used in experiments includes states contributed by the analog anti-alias filters and DAC smoothing filters. Figure 5.4 originally illustrated the signal mixing

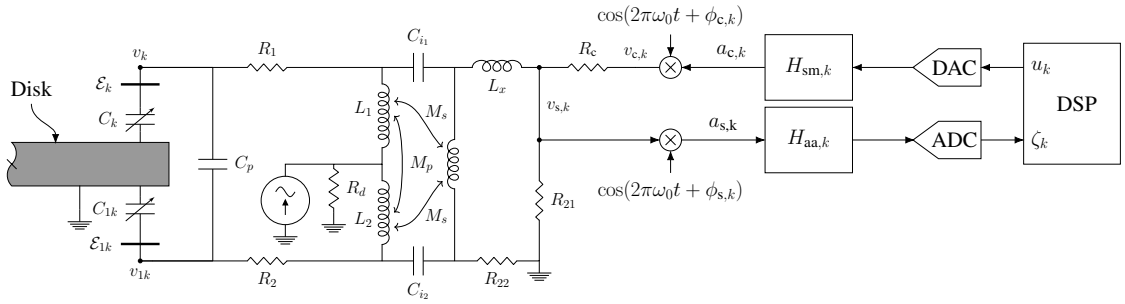

Figure 5.11: Interface between the DSP and transformer signals for the primary electrodes. The anti-alias and smoothing filters are denoted $H_{\rm aa}$ and $H_{\rm sm}$, respectively. The lateral electrodes use a similar demodulation scheme, however, since no control signals are associated with the lateral electrodes, the modulation path is not present for the lateral electrode signal conditioning.

described subsequently, and is reproduced here in Fig. 5.11. The DAC smoothing filter transfer function is denoted $H_{{\rm sm},k}$, $k = 1, \ldots, 4$ and outputs the signal $a_{{\rm c},k}$. The $v_{{\rm c},k}$ signals are generated by modulating $a_{{\rm c},k}$ with a phase-shifted sinusoid,

$$v_{{\rm c},k} = a_{{\rm c},k} \cos(2\pi\omega_0 t + \phi_{u_k}),\ k = 1, \ldots, 4$$

where the phases are selected to achieve the maximum amplitude differential on the $\{\mathcal{E}_k, \mathcal{E}_{1k}\}$ electrode potentials. A gain of 10 simply amplifies the voltage amplitude and is absorbed into the matrix B_{2k}. Each smoothing filter can be modeled by continuous-time state-space matrices. There are four, identical smoothing filters and since there is no coupling of signals between the filter states, the collection of these filters can be modeled by a single, decoupled state-space system $(A_{\rm sm}, B_{\rm sm}, C_{\rm sm}, 0)$ with the state vector denoted $q_{\rm sm}$, input u_c (the baseband control voltage), and output $a_{\rm c} = [a_{{\rm c},1}, a_{{\rm c},2}, a_{{\rm c},3}, a_{{\rm c},4}]^T$. Let $\mathcal{D}_{\rm c}(t)$ be defined as the diagonal matrix of modulating sinusoids

$$\mathcal{D}_{\rm c}(t) = \begin{bmatrix} \cos(\omega_0 t + \phi_{u,1}) & & \\ & \ddots & \\ & & \cos(\omega_0 t + \phi_{u,4}) \end{bmatrix}$$

so $v_{\rm c} = \mathcal{D}_{\rm c} a_{\rm c} = \mathcal{D}_{\rm c} C_{\rm sm} q_{\rm sm}$.

Demodulating and filtering $v_{\mathrm{s},k}$ removes the $2\omega_0$ harmonic components. These signals are filtered by anti-alias filters with transfer functions denoted $H_{\mathrm{aa},k}$, $k = 1, \ldots, 6$. Each filter has the input

$$a_{\mathrm{s},k} = v_{\mathrm{s},k} \cos(2\pi\omega_0 t + \phi_{s_k}),\ k = 1, \ldots, 6$$

and outputs the baseband signal ζ_k which is subsequently sampled. This filtering process is also consolidated into a single, decoupled state-space representation $(A_{\mathrm{aa}}, B_{\mathrm{aa}}, C_{\mathrm{aa}}, 0)$ with the state vector q_{aa}, input $a_{\mathrm{s}} = [a_{\mathrm{s},1}, \ldots, a_{\mathrm{s},6}]^T$, and output $\zeta = [\zeta_1, \ldots, \zeta_6]^T$. Let $\mathcal{D}_{\mathrm{s}}(t)$ be defined as the diagonal matrix of sinusoids which demodulate v_{s}

$$\mathcal{D}_{\mathrm{s}}(t) = \begin{bmatrix} 2\cos(\omega_0 t + \phi_{s,1}) & & \\ & \ddots & \\ & & 2\cos(\omega_0 t + \phi_{s,6}) \end{bmatrix}$$

so $a_{\mathrm{s}} = \mathcal{D}_{\mathrm{s}} v_{\mathrm{s}}$ Gathering Eqs. 5.31, 5.25, Eq. 5.27, and the results of the signal conditioning, the full nonlinear equations of motion for the suspension system are

$$\begin{aligned} \dot{q}_{\mathrm{sm}} &= A_{\mathrm{sm}} q_{\mathrm{sm}} + B_{\mathrm{sm}} u_c \\ v_{\mathrm{c}} &= \mathcal{D}_{\mathrm{c}} C_{\mathrm{sm}} q_{\mathrm{sm}} \\ M(q)\dot{w} &= Aw + B_1 i_{\mathrm{ct}} + B_2 v_{\mathrm{c}} \\ v_{\mathrm{s}} &= Jw \\ \dot{q}_{\mathrm{aa}} &= A_{\mathrm{aa}} q_{\mathrm{aa}} + B_{\mathrm{aa}} \mathcal{D}_{\mathrm{s}} v_{\mathrm{s}} \\ \zeta &= C_{\mathrm{aa}} q_{\mathrm{aa}} \\ \frac{d}{dt}\begin{bmatrix} q \\ \dot{q} \end{bmatrix} &= \begin{bmatrix} \dot{q} \\ f(q, \dot{q}, w) \end{bmatrix}. \end{aligned} \tag{5.32}$$

5.3.4 Linear Time-Periodic Variational Equations

The governing equations are overdetermined and nonlinear, however, a periodic solution exists in which mean-value of the electrostatic forces and gravitational force sum to zero

in the Z-direction and exert zero net moment on the disk. Such a solution can be found when the disk's kinematic parameters are zero, i.e. $q = 0$. In this case, the capacitances between each electrode pair and the disk are equal as are the corresponding potentials, i.e. $C_k(0) = C_{1k}(0)$ and $v_k = v_{1k}$ for $k = 1, \ldots, 8$. With a nonzero $i_{\rm ct}(t)$, steady-state sinusoids for all the voltages and currents in the transformers are established. Further, $i_{\rm ct}$ instates the master phase for referencing all signals. In this configuration, the elements of u_c are adjusted such that electrostatic forces balance the force due to gravity. The offset of u_c at this condition is denoted $\bar{u}$. Thus, the sinusoidal steady-state response of the transformer variables, denoted w_0, is computed from

$$M(0)\dot{w}_0 = Aw_0 + B_1 i_{\rm ct} - B_2 \mathcal{D}_{\rm c} C_{\rm sm} A_{\rm sm}^{-1} B_{\rm sm} \bar{u} \tag{5.33}$$

where $i_{\rm ct} = a_{\rm ct} \cos 2\pi\omega_0 t$. The disk is considered at equilibrium because the mean values of the elements of $f(0, 0, w_0)$ are equal to zero. In this analysis the $2\omega_0$ components of the electrostatic forces are ignored because as far as the kinematic variables are concerned, the disk acts like low pass filter. Further, $q = 0$ and $\dot{q} = 0$ as a result of the zero mean force. The steady-state solution of the anti-alias filter equations at equilibrium is denoted $\bar{q}_{\rm aa}$ and satisfies

$$\dot{\bar{q}}_{\rm aa} = A_{\rm aa}\bar{q}_{\rm aa} + B_{\rm aa}\mathcal{D}_{\rm s} J w_0.$$

The filter output $\zeta = C_{\rm aa}\bar{q}_{\rm aa}$ is essentially constant because the $2\omega_0$ terms are severely attenuated. Perturbation variables, relative to the steady-state values, are introduced to

compute the linear variational equations,

$$\begin{aligned} u_c &= \bar{u} + u \\ q_{\text{sm}} &= -A_{\text{sm}}^{-1} B_{\text{sm}} \bar{u} + \delta_{\text{sm}} \\ w &= w_0 + \delta_w, \\ q &= 0 + \delta_q \\ \dot{q} &= 0 + \delta_{\dot{q}} \\ q_{\text{aa}} &= \bar{q}_{\text{aa}} + \delta_{\text{aa}}, \end{aligned} \tag{5.34}$$

where $\delta_q := [\delta_x,\ \delta_y,\ \delta_z,\ \delta_\theta,\ \delta_\varphi]^T$. The mass matrix, M, is continuously differentiable in a neighborhood of q and so is represented (following elimination of higher order terms) as

$$M(q) = M(0) + \underbrace{\frac{\partial M}{\partial x}\Big|_{q=0}}_{M_x} \delta_x + \underbrace{\frac{\partial M}{\partial y}\Big|_{q=0}}_{M_y} \delta_y + \underbrace{\frac{\partial M}{\partial z}\Big|_{q=0}}_{M_z} \delta_z + \underbrace{\frac{\partial M}{\partial \theta}\Big|_{q=0}}_{M_\theta} \delta_\theta + \underbrace{\frac{\partial M}{\partial \varphi}\Big|_{q=0}}_{M_\varphi} \delta_\varphi$$

where M_x, M_y, M_z, M_θ, and M_φ are each block diagonal, comprised of the matrices $\frac{\partial M_k}{\partial x}$, $\frac{\partial M_k}{\partial y}$, $\frac{\partial M_k}{\partial z}$, $\frac{\partial M_k}{\partial \theta}$, and $\frac{\partial M_k}{\partial \varphi}$, respectively, evaluated at $q = 0$, down the diagonal. The matrix M_k refers to the mass matrix for a specific transformer (e.g. Eq. 5.30). Each matrix M_k has entries that depend on the capacitances $C_k(q)$ and $C_{1k}(q)$. These are the only entries which are dependent on the elements of q and as such, all of the partials of M are quite sparse, with nonzero entries only corresponding to the row and column where the coordinate-dependent capacitance is located. Let the entry (m_1, n_1) represent the entry of M_k such that $M_k(m_1, n_1) = C_k(q)$ and, similarly, let $M_k(m_2, n_2) = C_{1k}(q)$. These entries

evaluated at $q = 0$ are

$$\begin{aligned}
\frac{\partial}{\partial x} M_k(m_j, n_j) &= (-1)^j \frac{2r_d\sqrt{2}\varepsilon_r\varepsilon_0}{z0} \quad k = 5 \\
\frac{\partial}{\partial y} M_k(m_j, n_j) &= (-1)^j \frac{2r_d\sqrt{2}\varepsilon_r\varepsilon_0}{z0} \quad k = 6 \\
\frac{\partial}{\partial z} M_k(m_j, n_j) &= (-1)^{j-1} \frac{C_{k,0}}{z_0} \quad \forall k \\
\frac{\partial}{\partial \theta} M_k(m_j, n_j) &= (-1)^{\frac{k}{2}+j-1} r_0 \frac{C_{k,0}}{z_0} \quad k = 2, 4 \\
\frac{\partial}{\partial \varphi} M_k(m_j, n_j) &= (-1)^{\frac{k-1}{2}+j-1} r_0 \frac{C_{k,0}}{z_0} \quad k = 1, 3
\end{aligned}$$

with $j = 1, 2$ and all other entries being zero. Substituting the perturbation variables in Eq. 5.34 and linearized mass matrix into (5.32) and retaining only the linear terms produced yields:

$$\begin{aligned}
\dot{\delta}_{\text{sm}} &= A_{\text{sm}}\delta_{\text{sm}} + B_{\text{sm}}u \\
M(0)\dot{\delta}_w &= A\delta_w + B_2\mathcal{D}_{\text{c}}C_{\text{sm}}\delta_{\text{sm}} \\
&\quad - \left(M_x\delta_x + M_y\delta_y + M_z\delta_z + M_\theta\delta_\theta + M_\varphi\delta_\varphi\right)\dot{w}_0 \\
\dot{\delta}_q &= \delta_{\dot{q}} \\
\dot{\delta}_{\dot{q}} &= \nabla_w f(0,0,w_0)\delta_w + \nabla_q f(0,0,w_0)\delta_q \\
&\quad + \nabla_{\dot{q}} f(0,0,w_0)\delta_{\dot{q}} \\
\dot{\delta}_{\text{aa}} &= A_{\text{aa}}\delta_{\text{aa}} + B_{\text{aa}}\mathcal{D}_{\text{s}}J\delta_w \\
\zeta &= C_{\text{aa}}\bar{q}_{\text{aa}} + C_{\text{aa}}\delta_{\text{aa}}
\end{aligned} \tag{5.35}$$

where $\nabla_w f(0,0,w_0)$, $\nabla_q f(0,0,w_0)$, $\nabla_{\dot{q}} f0,0,w_0)$ are the gradients of the forces and toques with respect the variables w, q, and $\dot{q}$, respectively. The mass matrix $M(0)$ is not full rank and overdetermined. As such, the algebraic constraints in Eq. 5.35 are resolved with a

coordinate change using an SVD. An SVD of $M(0)$ may be expressed as

$$M(0) = \underbrace{\begin{bmatrix} U_1 & U_2 \end{bmatrix}}_{U} \begin{bmatrix} \Sigma_1 & 0 \\ 0 & 0 \end{bmatrix} \underbrace{\begin{bmatrix} V_1^T \\ V_2^T \end{bmatrix}}_{V}.$$

The perturbation variables are defined by

$$\delta_w = \begin{bmatrix} V_1 & V_2 \end{bmatrix} \begin{bmatrix} \delta_1 \\ \delta_2 \end{bmatrix}$$

and pre-multiplication of (5.35) by U^T yields

$$\begin{aligned} \begin{bmatrix} \Sigma\dot{\delta}_1 \\ 0 \end{bmatrix} &= \begin{bmatrix} U_1^T A V_1 & U_1^T A V_2 \\ U_2^T A V_1 & U_2^T A V_2 \end{bmatrix} \begin{bmatrix} \delta_1 \\ \delta_2 \end{bmatrix} \\ &\quad - \begin{bmatrix} U_1^T \\ U_2^T \end{bmatrix} \left(\left(M_x \delta_x + M_y \delta_y + M_z \delta_z + M_\theta \delta_\theta + M_\varphi \delta_\varphi \right) \dot{w}_0 + B_2 \mathcal{D}_\mathrm{c} C_\mathrm{sm} \delta_\mathrm{sm} \right). \end{aligned} \tag{5.36}$$

The lower half of (5.36) represents a set of algebraic constraints, the solution of which is

$$\begin{aligned} \delta_2 = &- \left(U_2^T A V_2 \right)^{-1} U_2^T \big[A V_1 \delta_1 \\ &- \left(M_x \delta_x + M_y \delta_y + M_z \delta_z + M_\theta \delta_\theta + M_\varphi \delta_\varphi \right) \dot{w}_0 + B_2 \mathcal{D}_\mathrm{c} C_\mathrm{sm} \delta_\mathrm{sm} \big]. \end{aligned} \tag{5.37}$$

Using Eq. 5.37, δ_w can be expressed explicitly as a function of the essential states,

$$\begin{aligned} \delta_w &= V_1 \delta_1 + V_2 \delta_2 \\ &= V_1 \delta_1 - V_2 \left(U_2^T A V_2 \right)^{-1} U_2^T \big[A V_1 \delta_1 \\ &\quad - \left(M_x \delta_x + M_y \delta_y + M_z \delta_z + M_\theta \delta_\theta + M_\varphi \delta_\varphi \right) \dot{w}_0 + B_2 \mathcal{D}_\mathrm{c} C_\mathrm{sm} \delta_\mathrm{sm} \big] \\ &= \left(I - PA \right) V_1 \delta_1 + P \left(M_x \delta_x + M_y \delta_y + M_z \delta_z + M_\theta \delta_\theta + M_\varphi \delta_\varphi \right) \dot{w}_0 \\ &\quad - W B_2 \mathcal{D}_\mathrm{c} C_\mathrm{sm} \delta_\mathrm{sm} \end{aligned} \tag{5.38}$$

where $W = V_2 \left(U_2^T A V_2\right)^{-1} U_2^T$. Substitution of (5.37) into the top half of (5.36) yields

$$\begin{aligned}\dot{\delta}_1 = \Sigma_1^{-1} U_1^T \left(I - AW\right) \Big[& AV_1\delta_1 \\ & - \left(M_x\delta_x + M_y\delta_y + M_z\delta_z + M_\theta\delta_\theta + M_\varphi\delta_\varphi\right)\dot{w}_0 + B_2\mathcal{D}_{\mathrm{c}}C_{\mathrm{sm}}\delta_{\mathrm{sm}}\Big].\end{aligned} \tag{5.39}$$

With Eq. 5.39, the equations of motion for the entire disk-electronics system represented in Fig. 5.4 are

$$\begin{aligned}\dot{\delta}_{\mathrm{sm}} &= A_{\mathrm{sm}}\delta_{\mathrm{sm}} + B_{\mathrm{sm}}u \\ \dot{\delta}_1 &= \Sigma_1^{-1} U_1^T \left(I - AW\right) \Big[AV_1\delta_1 + B_2\mathcal{D}_{\mathrm{c}}C_{\mathrm{sm}}\delta_{\mathrm{sm}} \\ &\qquad - \left(M_x\delta_x + M_y\delta_y + M_z\delta_z + M_\theta\delta_\theta + M_\varphi\delta_\varphi\right)\dot{w}_0\Big] \\ \dot{\delta}_q &= \delta_{\dot{q}} \\ \dot{\delta}_{\dot{q}} &= \nabla_w f(0,0,w_0)\delta_w + \nabla_q f(0,0,w_0)\delta_q \\ &\qquad + \nabla_{\dot{q}} f(0,0,w_0)\delta_{\dot{q}} \\ \dot{\delta}_{\mathrm{aa}} &= A_{\mathrm{aa}}\delta_{\mathrm{aa}} + B_{\mathrm{aa}}\mathcal{D}_{\mathrm{s}}J\delta_w \\ \zeta &= C_{\mathrm{aa}}\bar{q}_{\mathrm{aa}} + C_{\mathrm{aa}}\delta_{\mathrm{aa}}\end{aligned} \tag{5.40}$$

where $u \in \mathbf{R}^4$ consists of the desired amplitudes for each v_{c_i} and the output $\zeta \in \mathbf{R}^6$ is comprised of the demodulated voltages $v_{s,k}$. Elaboration of the gradient components is tedious and the specifics are found in Appendix B. Expanding the gradient pieces, Eqs. 5.38, 5.40, B.15–B.19, B.27–B.31, B.41–B.45, B.69–B.73, and B.55–B.59 (most of which are zero) give the following linear, time-periodic variational equations describing the states of the transformer-disk suspension system,

$$
\begin{aligned}
\dot{\delta}_{\mathrm{sm}} &= A_{\mathrm{sm}}\delta_{\mathrm{sm}} + B_{\mathrm{sm}}u \\
\dot{\delta}_1 &= \Sigma_1^{-1}U_1^T\left(I - AP\right)\Big[AV_1\delta_1 + B_2\mathcal{D}_{\mathrm{c}}C_{\mathrm{sm}}\delta_{\mathrm{sm}} \\
&\quad - \left(M_x\delta_x + M_y\delta_y + M_z\delta_z + M_\theta\delta_\theta + M_\varphi\delta_\varphi\right)\dot{w}_0\Big] \\
\dot{\delta}_x &= \delta_{\dot{x}} \\
\dot{\delta}_{\dot{x}} &= f_{x,\theta}\delta_\theta \\
\dot{\delta}_y &= \delta_{\dot{y}} \\
\dot{\delta}_{\dot{y}} &= f_{y,\varphi}\delta_\varphi \\
\dot{\delta}_z &= \delta_{\dot{z}} \\
\dot{\delta}_{\dot{z}} &= f_{z,w}(I - WA)V_1\delta_1 + (f_{z,z} + f_{z,w}WM_z\dot{w}_0)\delta_z - \frac{c_z}{m}\delta_{\dot{z}} \\
&\quad + f_{z,w}PM_\varphi\dot{w}_0\delta_\varphi + f_{z,w}WM_\theta\dot{w}_0\delta_\theta - f_{z,w}WB_2\mathcal{D}_{\mathrm{c}}C_{\mathrm{sm}}\delta_{\mathrm{sm}} \\
\dot{\delta}_\theta &= \delta_{\dot{\theta}} \\
\dot{\delta}_{\dot{\theta}} &= f_{\theta,w}(I - WA)V_1\delta_1 + f_{\theta,y}\delta_y + f_{\theta,w}WM_z\dot{w}_0\delta_z - \frac{c_\theta}{J_{xy}}\delta_{\dot{\theta}} \\
&\quad + (f_{\theta,\theta} + f_{\theta,w}WM_\theta\dot{w}_0)\delta_\theta + f_{\theta,w}WM_\varphi\dot{w}_0\delta_\varphi - f_{\theta,w}WB_2\mathcal{D}_{\mathrm{c}}C_{\mathrm{sm}}\delta_{\mathrm{sm}} \\
\dot{\delta}_\varphi &= \delta_{\dot{\varphi}} \\
\dot{\delta}_{\dot{\varphi}} &= f_{\varphi,w}(I - WA)V_1\delta_1 + f_{\varphi,x}\delta_x + f_{\varphi,w}WM_z\dot{w}_0\delta_z - \frac{c_\varphi}{J_{xy}}\delta_{\dot{\varphi}} \\
&\quad + f_{\varphi,w}WM_\theta\dot{w}_0\delta_\theta + (f_{\varphi,\varphi} + f_{\varphi,w}WM_\varphi\dot{w}_0)\delta_\varphi - f_{\varphi,w}WB_2\mathcal{D}_{\mathrm{c}}C_{\mathrm{sm}}\delta_{\mathrm{sm}} \\
\dot{\delta}_{\mathrm{aa}} &= A_{\mathrm{aa}}\delta_{\mathrm{aa}} + B_{\mathrm{aa}}\mathcal{D}_{\mathrm{s}}J\Big[\left(I - WA\right)V_1\delta_1 - WB_2\mathcal{D}_{\mathrm{c}}C_{\mathrm{sm}}\delta_{\mathrm{sm}} \\
&\quad + W\left(M_x\delta_x + M_y\delta_y + M_z\delta_z + M_\theta\delta_\theta + M_\varphi\delta_\varphi\right)\dot{w}_0\Big] \\
\zeta &= C_{\mathrm{aa}}\delta_{\mathrm{aa}}
\end{aligned}
\tag{5.41}
$$

where $C_{\mathrm{aa}}\bar{q}_{\mathrm{aa}}$ is a feedthrough offset which is dropped since it is removed in practice. The smoothing and anti-aliasing filters are all selected to be identical 4-pole Butterworth filters with a 1kHz corner, thus contributing 40 states to the system of equations. Coupled with 10 states from the disk dynamics and 36 states from the reduced electrical model, these

equations are merged into a 86-state system via the state vector

$$\delta = [\delta_{\text{sm}},\, \delta_1,\, \delta_x,\, \delta_y,\, \delta_z,\, \delta_\varphi,\, \delta_\theta,\, \delta_{\text{aa}}]^T,$$

the input u, and output ζ to form $A_\delta(t)$, $B_\delta(t)$, and C_δ, accordingly, yielding a more compact representation of Eq. 5.41

$$\begin{aligned} \dot{\delta} &= A_\delta(t)\delta + B_\delta(t)u \\ \zeta &= C_\delta\delta. \end{aligned} \tag{5.42}$$

5.3.5 Discrete Time Approximation and Frequency Response

Both $A_\delta(t)$ and $B_\delta(t)$ in Eq.5.42 are time-periodic with period $1/\omega_0$. Stability of Eq. 5.42 (which corresponds to the system in equilibrium) is analyzed using the disk and electrical subsystem parameters given previously in Tables 1.1 and 5.1. An approximate time-invariant model can be derived as follows. Note that the applied electrostatic forces and torques vary at twice the carrier frequency (50 kHz). Essentially, the disk responds to the mean value of the electrostatic forces, so z, x, y, θ, and φ evolve on slow time scales compared to the currents and voltages associated with the electrical subsystem as suggested by the poles of the system. In essence, the disk effectively low-pass filters the effect of the forces and, in essence, responds to the mean value of the forces and torques. Since the measurements are electrical proxies of the disk's kinematic variables (as will be demonstrated), and because there is additional band-limiting due to the smoothing and anti-alias filters, it is possible to derive an approximate discrete-time model of the system. An approximate frequency response function may therefore be derived for Eq. 5.42 through the discretization method used previously. The solution to an initial value problem for (5.42) is

$$\delta(t) = \Theta(t, t_0)\delta(t_0) + \int_{t_0}^{t} \Theta(t, \tau)B_\delta(\tau)u(\tau)d\tau, \quad t \geq t_0,$$

where $\delta(t_0)$ is the initial condition represented in the perturbation variables, $\Theta(t, t_0)$ denotes the state transition matrix of the periodic system in Eq. 5.42, and u is the control

voltage input. The start time t_0 specifies the phase of the time-periodic steady-state solution about which the linearization is computed. As was shown in Chapter 2.2.3, choice of t_0 has no practical impact on the subsequent model, thus, it is assumed $t_0 = 0$ for the remainder of the analysis. Since experiments are sampled through the DSP, consider relate successive samples of δ at a DSP sample rate $t_s = n/\omega_0$, for some integer $n > 1$,

$$\delta((k+1)t_s) = \Theta((k+1)t_s, kt_s)\delta(kt_s) + \int_{k_t s}^{(k+1)t_s} \Theta((k+1)t_s, \tau)B_\delta(\tau)u(\tau)d\tau.$$

Due to the periodicity of Eq. 5.42, the state transition matrix satisfies $\Theta(p/\omega_0, m/\omega_0) = \Theta^{p-m}(1/\omega_0, 0)$ for any integers p, m so $\Theta((k+1)t_s, kt_s) = \Theta(t_s, 0) = \Theta^n(1/\omega_0, 0)$, where $\Theta(1/\omega, 0)$ is the monodromy matrix associated with the time periodic system. An approximate time-invariant system is again derived by assuming the control variable is slowly varying over $[(k+1)t_s, kt_s]$. This assumption introduces zero-order-hold dynamics representative of the DAC conversion process. Under this assumption, u is effectively constant with respect to the integral and the state is estimated one period later as,

$$\delta((k+1)t_s) \approx \Theta((k+1)t_s, kt_s)\delta(kt_s) + \left(\int_{k_t s}^{(k+1)t_s} \Theta((k+1)t_s, \tau)B_\delta(\tau)d\tau\right) u(k).$$

The propagation of Eq. 5.42 is approximated by the discrete time equation

$$\begin{aligned} \delta[k+1] &= \Phi\delta[k] + \Gamma u[k] \\ \zeta[k] &= C_\delta \delta[k] \end{aligned} \tag{5.43}$$

where

$$\Phi := \Theta(\tau_p + t_0, t_0), \quad \Gamma := \int_{t_0}^{\tau_p + t_0} \Theta(\tau_p + t_0, \tau)B_\delta(\tau)d\tau.$$

From the discrete time representation, the frequency responses from u to the each demodulated voltage reference of the electrode-disk gap ζ_j (see Fig. 5.4) may be computed. Numerical integration is used to compute Φ and Γ.

A frequency response estimate of the input/output from u_1 to ζ_1 is shown in Fig. 5.12. An

obvious feature is the presence of a flat pass-band above 10 Hz due to the colocation of the pick-off and control point through the transformer. This feedthrough coupling obscures the voltage measurements of the gap above 1 Hz and biases the motional components associated with the disk at low frequencies. Due to prior assumptions regarding the decoupling of transformer center tap currents, there is virtually no "cross-channel"' feedthrough. As such, the "cross-channels" are left uncompensated. In practice, this is not generally the case. Fortunately, the feedthrough can be identified and mitigated with an appropriate feedforward filter. For the model, however, the feedthrough can be determined from the full plant by constraining $q = 0$ which removes the disk dynamics from the analysis. The feedthrough frequency response is also shown in Fig. 5.12. With the feedthrough removed, the frequency response estimate of u_1 to ζ_1 is also given in Fig. 5.12 and represents the voltage measurement proxy of the gap solely due to disk motion. This must be done for all the four input/output u_k to ζ_k channels. There is no feedthrough for u_1–u_4 to ζ_5 or ζ_6 as these output channels are used for detecting lateral motion only and no input is applied to these transformer networks. Given the four input, six output nature of the system, there are 24 total frequency responses. These frequency responses are shown in Figs. 5.13– 5.14.

The eigenvalues of Φ are investigated to assess the system's open-loop characteristics. Fig. 5.15 shows the system is inherently unstable due to several eigenvalues outside the unit disk. There are three poles decidedly outside of the unit disk which will be shown to correspond to the instability in the modes associated with the dynamics governing z, φ, and θ. The three eigenvalues outside the unit disk are

$$\{1.00128, 1.00140, 1.00140\}$$

with real pole approximations 1.02 and 1.11 Hz. This confirms that the disk dynamics evolve on a much slower time scale than the carrier frequency. There are also two pairs of stable lightly-damped eigenvalues that correspond two resonant modes with natural frequencies near 0.2 Hz.

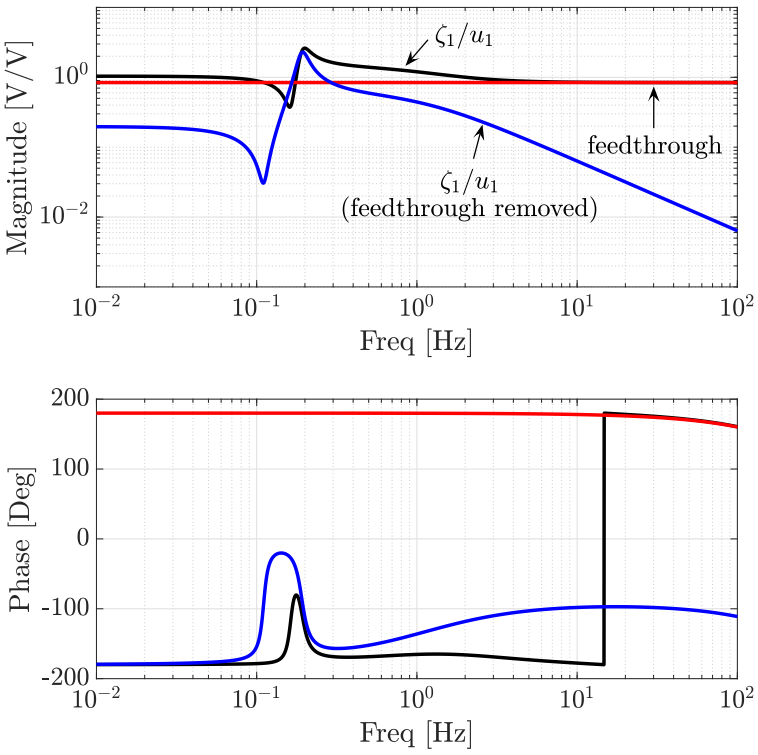

Figure 5.12: Frequency responses of discrete-time models ζ_1/u_1, ζ_1/u_1 with feedthrough removed, and the feedthrough when $t_0 = 0$. The "sample rate" for the models is the frequency $\omega_0/5$

5.3.6 Decoupled Plant

Although these approximate frequency responses represent the input/output dynamics of the system, a more intuitive approach, based on the kinematic equations in Eq. 5.15, the transformer-electrode arrangement, and the relative isolation of the lateral electrodes from the z, θ, and φ degrees-of-freedom is procured. Each control voltage $u_k \in u$ induces a torque on the disk. For the choice of $\phi_{c,k}$ previously described, when $u_k > 0$, the voltages on $\mathcal{E}_k$ rise whereas the voltages on $\mathcal{E}_{1k}$ drop. As a result, the electrostatic forces from the upper electrodes rise and decrease for the bottom set. Naturally, the opposite is true for $u_k < 0$. In this fashion, specifying $u_k > 0 \; \forall k$ will lift the disk in the $+z$-direction. By specifying $u_1 = u_3 = 0$, $u_2 < 0$, and $u_4 > 0$, a pure counterclockwise tilt about the x-axis ($\theta > 0$) will be realized. Similarly, a pure counterclockwise tilt about the y-axis ($\varphi > 0$) is accomplished by setting $u_1 > 0$, $u_3 < 0$, and $u_2 = u_4 = 0$. These relationships are described

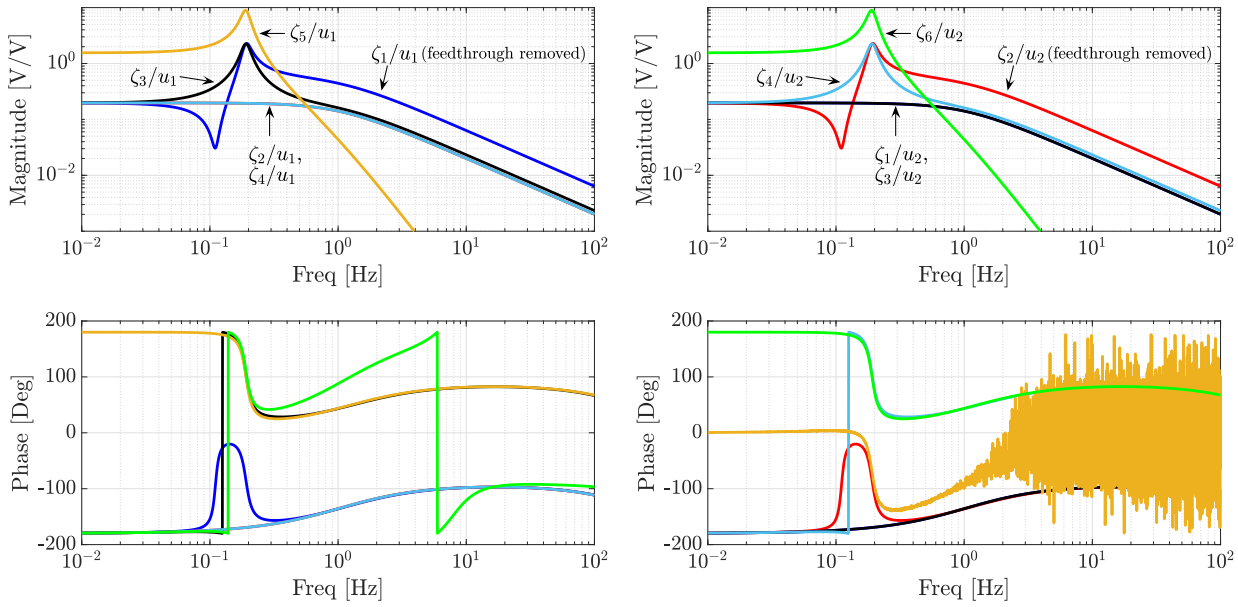

Figure 5.13: (Left) Frequency response approximations of the input u_1 to the compensated demodulated voltages ζ_1 and remaining "cross-channels" in ζ. (Right) Frequency response approximations of the input u_2 to the compensated demodulated voltages ζ_2 and remaining uncompensated "cross-channels" in ζ.

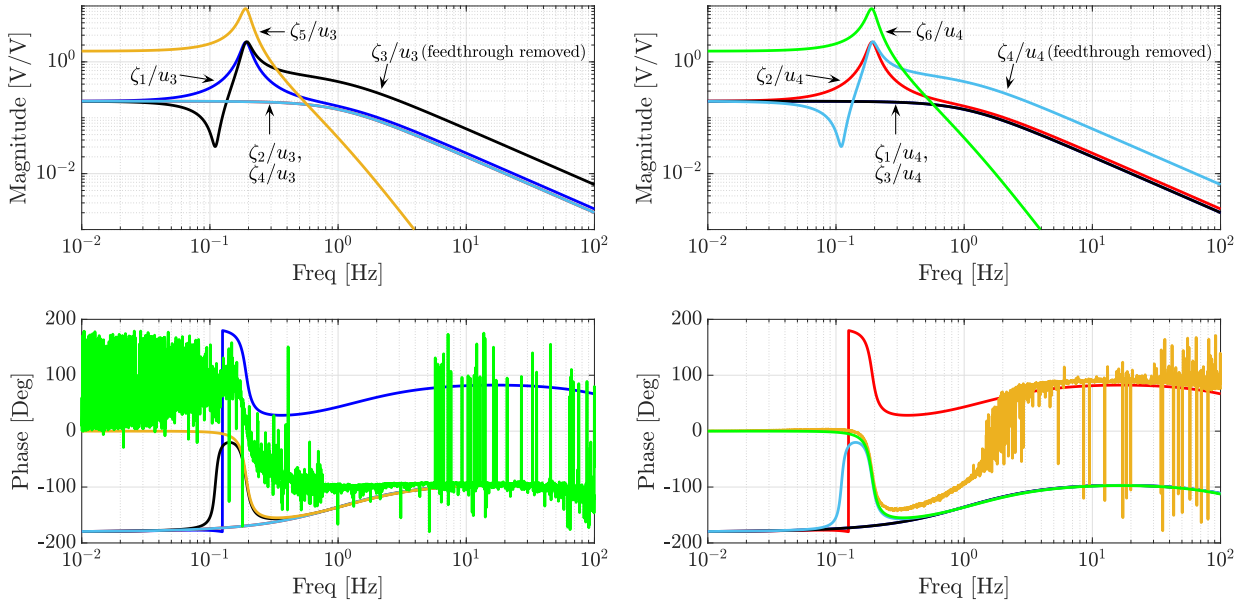

Figure 5.14: (Left) Frequency response approximations of the input u_3 to the compensated demodulated voltages $\tilde{\zeta}_3$ and remaining uncompensated "cross-channels" in ζ. (Right) Frequency response approximations of the input u_4 to the compensated demodulated voltages $\tilde{\zeta}_4$ and remaining uncompensated "cross-channels" in ζ.

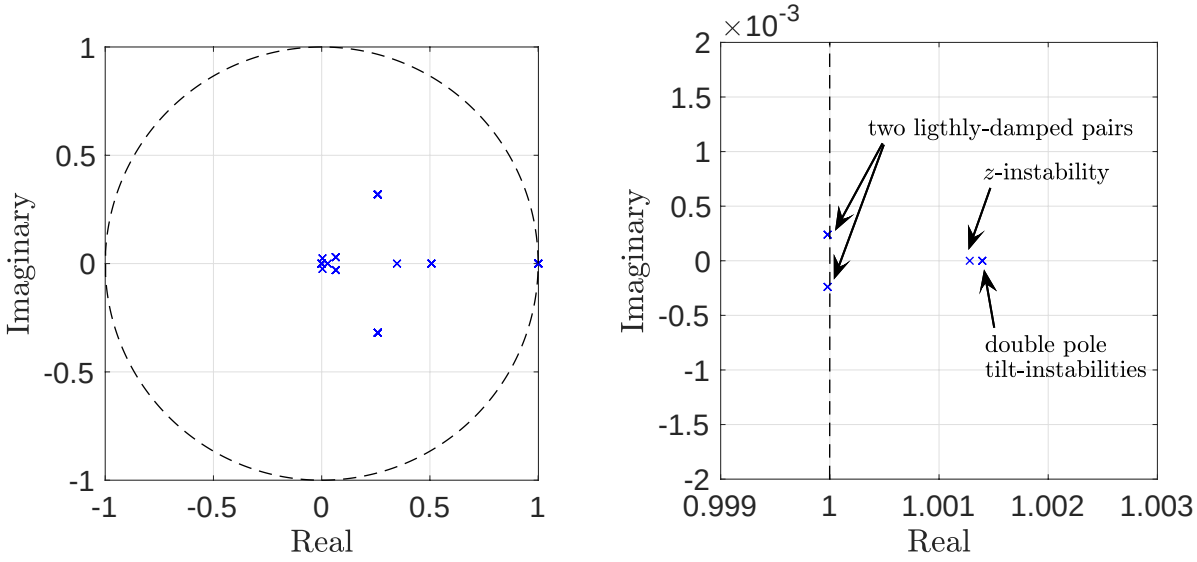

Figure 5.15: Characteristic multipliers of the time-periodic model in Eq. 5.42 (left). The poles near $1 + 0j$ correspond to the companion pairs of unstable and stable modes of the system (right).

by the (non-unique) transformation with the "new" input variables defined as $\{u_z, u_\varphi, u_\theta\}$,

$$\begin{bmatrix} u_1 \\ u_2 \\ u_3 \\ u_4 \end{bmatrix} = \underbrace{\begin{bmatrix} 0.5 & \frac{1}{\sqrt{2}} & 0 \\ 0.5 & 0 & -\frac{1}{\sqrt{2}} \\ 0.5 & -\frac{1}{\sqrt{2}} & 0 \\ 0.5 & 0 & \frac{1}{\sqrt{2}} \end{bmatrix}}_{N} \begin{bmatrix} u_z \\ u_\varphi \\ u_\theta \end{bmatrix}, \tag{5.44}$$

where $u_z > 0$ lifts the disk, $u_\varphi > 0$ provides a $\varphi > 0$ rotation, and $u_\theta > 0$ yields a $\theta > 0$ rotation. The columns of N are chosen as to have unit norm. An analogous transformation of the demodulated voltages in ζ (after feedthrough has been removed) can found via the kinematic equations in Eq. 5.15 to yield voltages directly related to the degrees-of-freedom. The disk-electrode gaps are governed by Eq. 5.15 and, therefore, ζ_k for $k = 1, \ldots, 4$ are as well. Substitution of the perturbation variables introduced previously into Eq. 5.15, the

following relations hold,

$$\sum_{k=1}^{4} z_k = 4\delta_z, \quad z_1 - z_3 = 2r_0\delta_\varphi, \quad z_4 - z_2 = 2r_0\delta_\theta.$$

In lieu of this fact, the demodulated, feedthrough compensated voltages in ζ are converted into voltages proxies for the DOFs, defined as $\{v_z, v_\varphi, v_\theta, v_x, v_y\}$,

$$\begin{bmatrix} v_z \\ v_\varphi \\ v_\theta \\ v_x \\ v_y \end{bmatrix} = \underbrace{\begin{bmatrix} 0.5 & 0.5 & 0.5 & 0.5 & 0 & 0 \\ \frac{1}{\sqrt{2}} & 0 & -\frac{1}{\sqrt{2}} & 0 & 0 & 0 \\ 0 & -\frac{1}{\sqrt{2}} & 0 & \frac{1}{\sqrt{2}} & 0 & 0 \\ 0 & 0 & 0 & 0 & 1 & 0 \\ 0 & 0 & 0 & 0 & 0 & 1 \end{bmatrix}}_{M} \begin{bmatrix} \zeta_1 \\ \zeta_2 \\ \zeta_3 \\ \zeta_4 \\ \zeta_5 \\ \zeta_6 \end{bmatrix}. \tag{5.45}$$

The rows of M are chosen to have unit norm. Voltage measurements corresponding to motion in x and y are inferred directly from the demodulated voltages registered from the transformers attached to the lateral electrodes. Pre- and post-multiplication of the

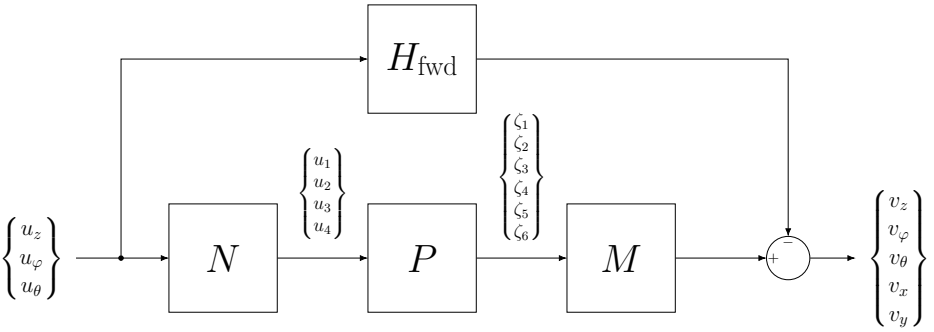

Figure 5.16: The feedforward-compensated and decoupled plant $\tilde{P} = MPN - H_{fwd}$. The decoupling matrices are defined in Eqs. 5.44 and 5.45.

plant P by N and M, respectively, transforms the system into a 3-input, 5-output plant, $\tilde{P} = MPN - H_{\text{fwd}}$. The system $\tilde{P}$ is referred to as the "decoupled" plant because the

transfer function matrix is of the form,

$$\tilde{P} = \begin{bmatrix} \star & 0 & 0 \\ 0 & \star & 0 \\ 0 & 0 & \star \\ 0 & \star & 0 \\ 0 & 0 & \star \end{bmatrix}$$

where $\star$ entires are non-zero. In this form, the $(1,1)$ elements of $\tilde{P}$ refers to v_z/u_z, the $(2,2)$ element to v_φ/u_φ, and so on. Due to the idealities of the modeled system, the other entries of $\tilde{P}$ are zero. The idealities include identical transformers, geometric symmetry, and gap uniformity. Diverging from any of these idealities raises the degree of coupling amongst all input/output channels, however, the original 5 transfer functions are still dominant. For this reason, the ideal model is only considered. A side-by-side compari-

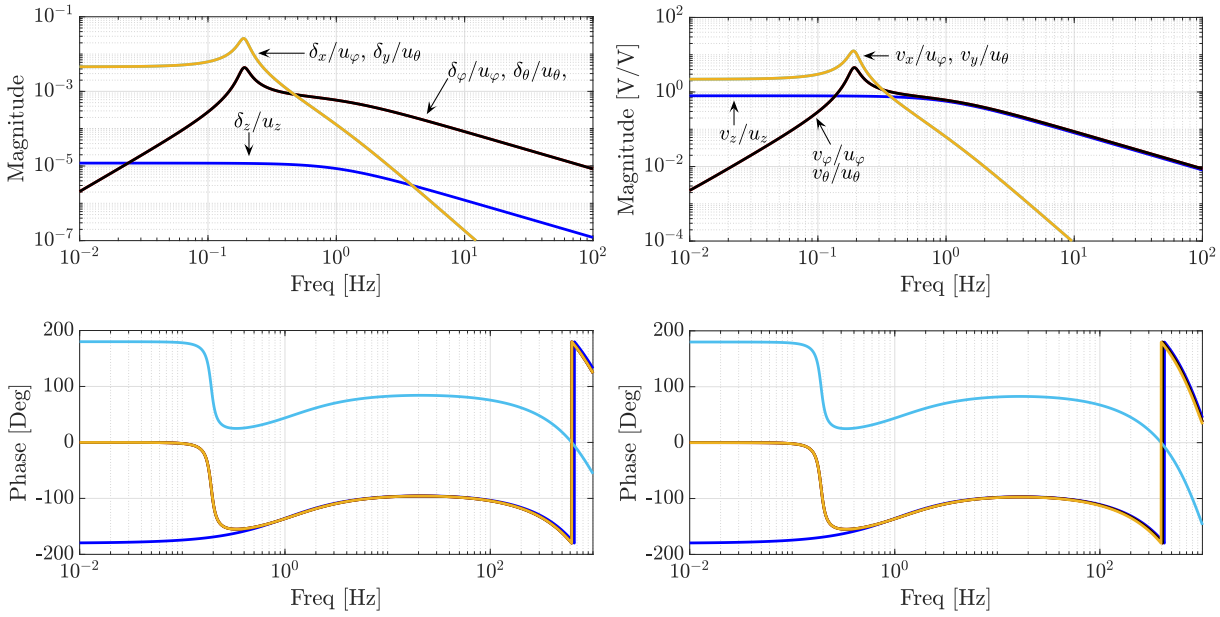

Figure 5.17: (Left) Frequency Response of the disk's kinematic perturbation variables $\{\delta_z, \delta_\varphi, \delta_\theta, \delta_x, \delta_y\}$. (Right) Frequency response of $\tilde{P}$.

son of the approximate frequency responses of decoupled, compensated plant $\tilde{P}$ and the degree-of-freedom variables is made in Fig. 5.17. Compensation of the feedthrough with a

feedforward filter reveals the same general trends as the measurements from the degrees-of-freedom. Further, the motional responses from all traces are essentially a low-pass filters. The corner frequencies of δ_z/u_z, δ_φ/u_φ, and δ_θ/u_θ are consistent with the stable and unstable companion poles computed from the eigenvalues $\Phi(\tau_p, 0)$. Due to the damping present in the model, the stable and unstable companion poles are bifurcated. The -20 dB per decade slope beyond the corner frequency is also consistent with this notion and the slope becomes steeper at higher frequencies beyond the stable pole location. A noticeable fact from these responses is a lightly damped resonance occurs in the neighborhood of 0.2Hz for the measurements v_θ, v_φ, v_x, and v_y. In addition, the frequency responses of the v_θ/u_θ and v_φ/u_φ roll-off below 0.2Hz. These facts have implications on the achievable loop gain in the control design. By comparison, one significant realization is the non-zero DC gain of the x and y frequency responses. The key remark from these figures indicates how commands for tilts, in θ and φ, cause the disk to slide along the y and x axes, respectively. In a stable closed-loop, the electrostatic forces would balance out the torques as the moment arms change and the disk would return to parallel with the electrodes (thus the zero DC gain in θ and φ), albeit shifted from the nominal configuration (the non-zero DC gain in y and x). This coupling between θ and y (likewise, φ and x) is evident in Eq. 5.41. It is therefore critical to include the lateral degrees-of-freedom in deriving an accurate model.

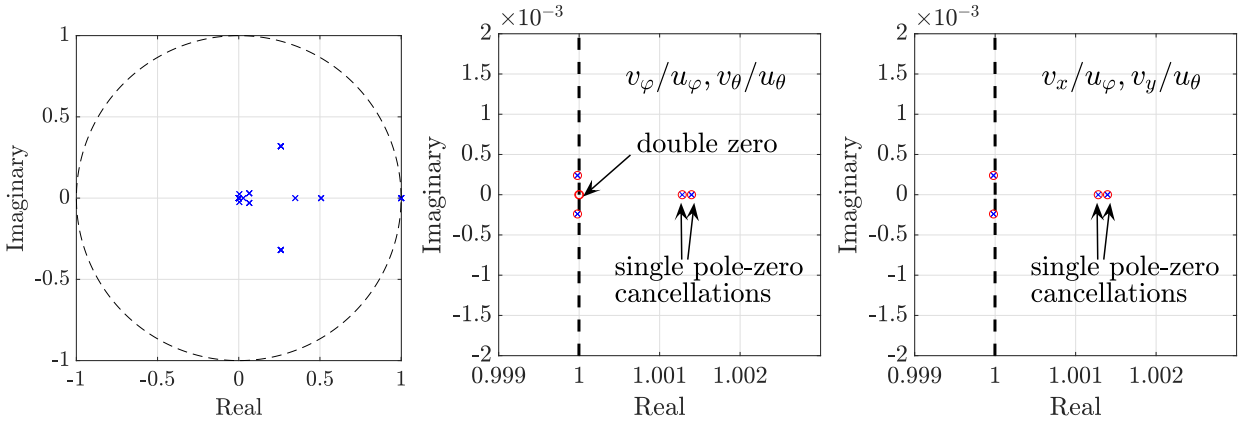

Figure 5.18: Eigenvalues of Φ and the detail of the unstable poles and zeros associated with the decoupled system transfer functions.

The pole-zero plots of the transfer functions in $\tilde{P}$ are shown in Fig. 5.18. The zeros of each

transfer function show multiple pole-zero cancellations and directly indicate the unstable poles associated with the transfer functions in $\tilde{P}$. In the transfer function v_z/u_z, two zeros located at the unstable pole locations $\{1.0014, 1.0014\}$. These blocking zeros indicate these two unstable poles are unobservable and uncontrollable in the transfer function v_z/u_z. Further, four zeros also cancel the two pairs of lightly-damped eigenvalues (c.f. Fig. 5.15) indicating these eigenvalues are unobservable as well. Thus, v_z/u_z can only stabilize the unstable pole at 1.00128 and is referred to as the 'z-instability'. Similarly, the tilt transfer functions v_φ/u_φ and v_θ/u_θ both have zeros at $\{1.00128, 1.0014\}$. Therefore, these transfer functions only exhibit one unstable pole at 1.0014, referred to as the 'tilt'-instability. The lightly-damped resonance near 0.2 Hz present in the frequency response plots is characteristic of the two pole pairs in Fig. 5.15. Both transfer function only contain a single pair of zeros to cancel out these poles, leaving the remaining conjugate pair in the transfer function. One feature unique to the tilt transfer functions is the double zero at 1. This creates an s^2 trend in the transfer function and implies a DC gain of zero. In terms of the physical system, this implies the disk angles are zero at equilibrium in the stabilized system. In fact, since no lateral forces act on the disk unless the disk is tilted. Since the electrode plates are normal to gravity, the disk cannot be held at a non-zero angle when the disk is at equilibrium. Finally, the v_x/u_φ and v_y/u_θ transfer functions exhibit the same properties as v_φ/u_φ and v_θ/u_θ with the exception of the double zeros at 1. However, the presence of the tilt-instabilities and lightly-damped pole pairs further indicate the coupling between these DOFs.

5.3.7 Controller Design for Decoupled Plant

Classical loop-shaping design is applied to the decoupled plant. Decoupling the plant simplifies the design method to loop-shaping about each of the decoupled transfer functions. SISO controllers, denoted G_z , G_φ and G_θ, are separately designed for v_z/u_z, v_φ/u_φ, and v_θ/u_θ to stabilize $\tilde{P}$. A block diagram of the closed-loop system is shown in Fig. 5.19. By using the lateral measurements, it is possible to regulate the lateral position of the disk.

This is accomplished by an "outer" feedback loop using the lateral position error as the references, denoted r_φ and r_θ, for the tilt degrees-of-freedom. These references are driven by the output of the lateral controllers, G_x and G_y.

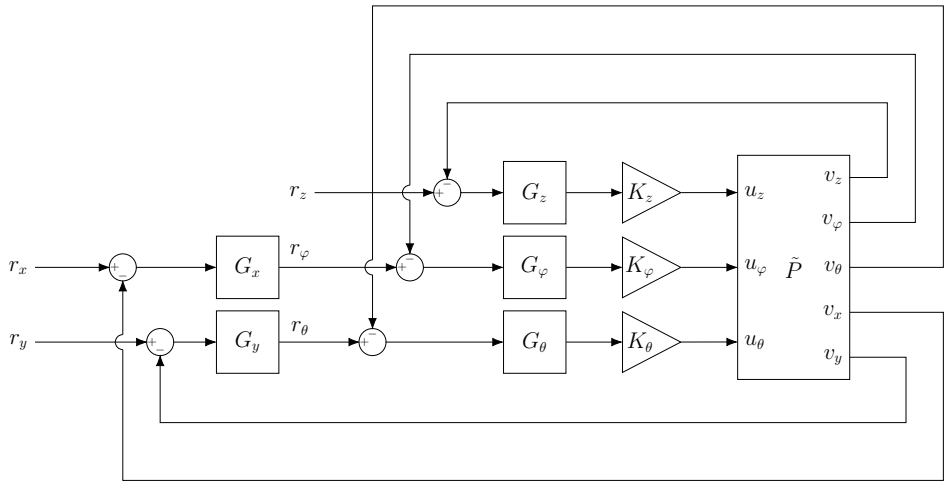

Figure 5.19: Block diagram of the closed-loop system. The pre- and post-multiplication matrices effectively decouples the input/output channels into the plant $\tilde{P}$ and G_{q_k} represent the controllers for the voltage proxy of the degree-of-freedom $q_k \in q$. Further, an "outer"-loop controller stabilizes the lateral degrees-of-freedom.

As shown in Fig. 5.18, v_z/u_z transfer function has only one unstable pole at 1.00128. The magnitude of v_z/u_z exhibits a low-pass characteristic whose corner frequency corresponds to this unstable pole (c.f Fig. 5.17), It is a simple matter to stabilize z-instability using constant gain feedback, however, due to uncertainty in the feedthrough cancellation at higher frequencies in the actual system, the controller gain is rolled off after 100 Hz. Thus, the (continuous-time) transfer function of the z-DOF controller, denoted G_z, is

$$G_z(s) = 4\frac{200\pi}{s + 200\pi} \tag{5.46}$$

In studying the tilt transfer functions reveals both v_φ/u_φ and v_θ/u_θ each have one unstable pole at 1.00140 -the other eigenvalue at this location is cancelled by a single zero. Stabilizing the tilt-instability is a unique problem because both v_φ/u_φ and v_θ/u_θ are not strongly stabilizable. Although this can be illustrated by analyzing the parity interlac-

ing property of the poles and zeros [Vid85], analysis of the Nyquist plot is insightful (see Fig. 5.21. Since $\|v_\varphi/u_\varphi\| \to 0$ when $\omega \to 0, \infty$, the loop gain (practically) must always have an even number of encirclements of $-1 + j0$. The loop gain of any physical system will have finite bandwidth and so no practical, realizable controller will be capable so negating this fact. The same is true of v_θ/u_θ. Since v_φ/u_φ and v_θ/u_θ have one unstable pole, the Nyquist stability criterion dictates the tilt controllers must necessarily have an odd number of unstable pole(s) if stability is to be achieved. The following controllers are implemented for v_φ/u_φ and v_θ/u_θ,

$$G_\theta(s) = G_\varphi(s) = \frac{14\pi}{s+14\pi}\frac{s^2+0.08\pi s+\omega_n^2}{s^2+0.4\pi s+\omega_n^2}\frac{s+3}{s-3} \tag{5.47}$$

where the unstable pole is set at 3 rad/s. A notch filter is included in the controllers to diminish the affect of the lightly-damped resonance. The loop gains of G_z and G_φ are shown in Fig. 5.20 and the Nyquist plots in Fig. 5.21. The loop gain and Nyquist plot for G_θ is the same as G_φ. Using these controllers to close the loops around v_z/u_z, v_φ/u_φ, and v_θ/u_θ the pole plot of the closed-loop system in Fig. 5.22 shows the closed-loop system is asymptotically stable. Although the closed-loop system is asymptotically stable, regulation

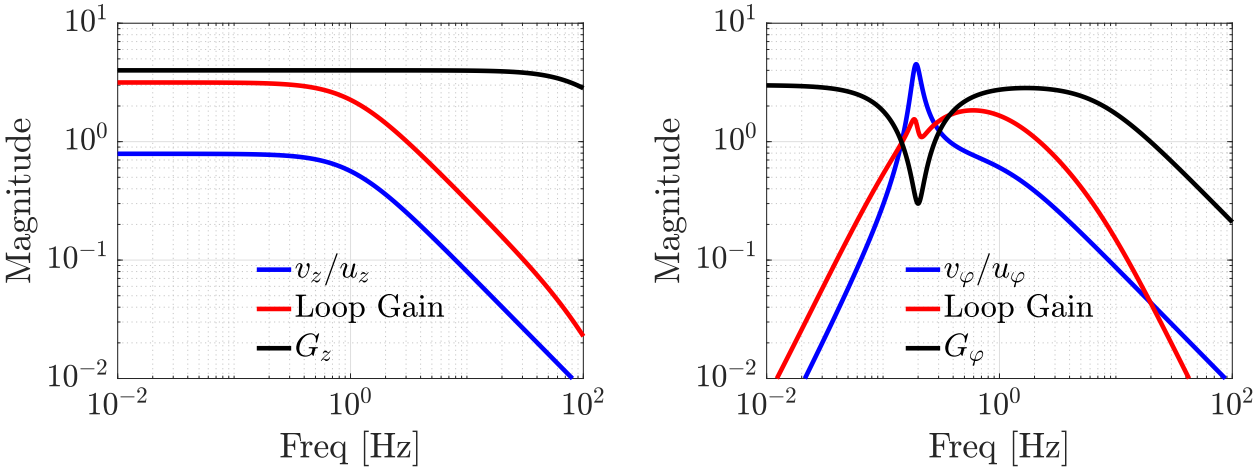

Figure 5.20: Loop gains and controllers for v_z/u_z (Left) and v_φ/u_φ (Right).

of the lateral position of the disk is also considered using measurements of the disk's lateral position. From the pole-zero plots (Fig. 5.18) of v_x/u_φ and v_y/u_θ, one tilt-instability

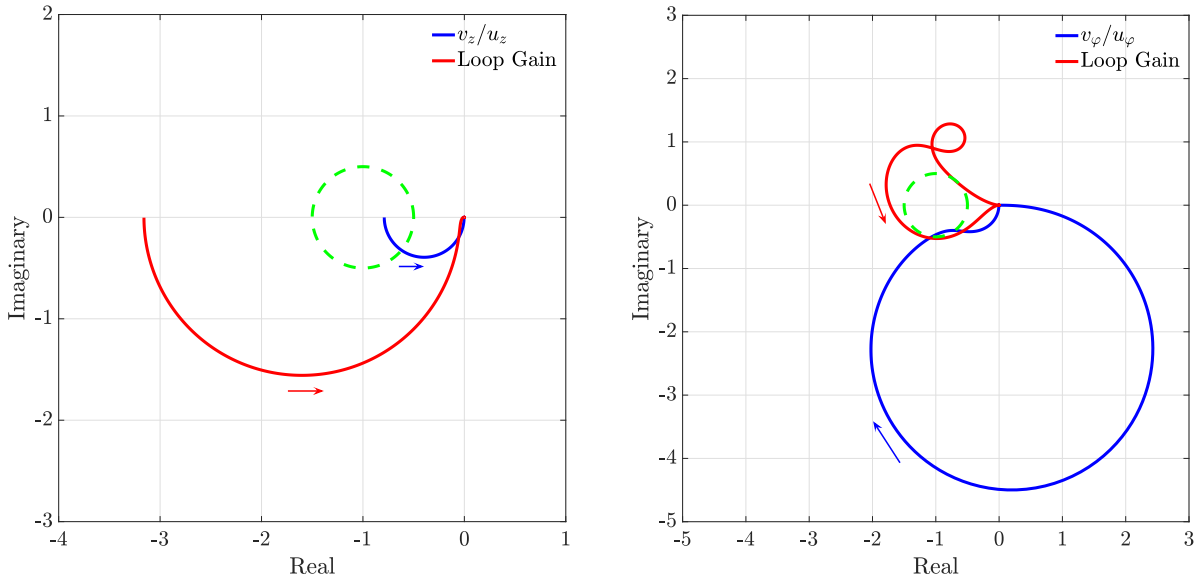

Figure 5.21: (Left) Nyquist plot of v_z/u_z and the loop gain illustrating one counterclockwise encirclement of -1 (only $\omega > 0$ shown). (Right) Nyquist plot of v_φ/u_φ and the loop gain illustrating two counter-clockwise encirclements of -1 (only $\omega > 0$ shown). Arrows indicate the direction of increasing frequency.

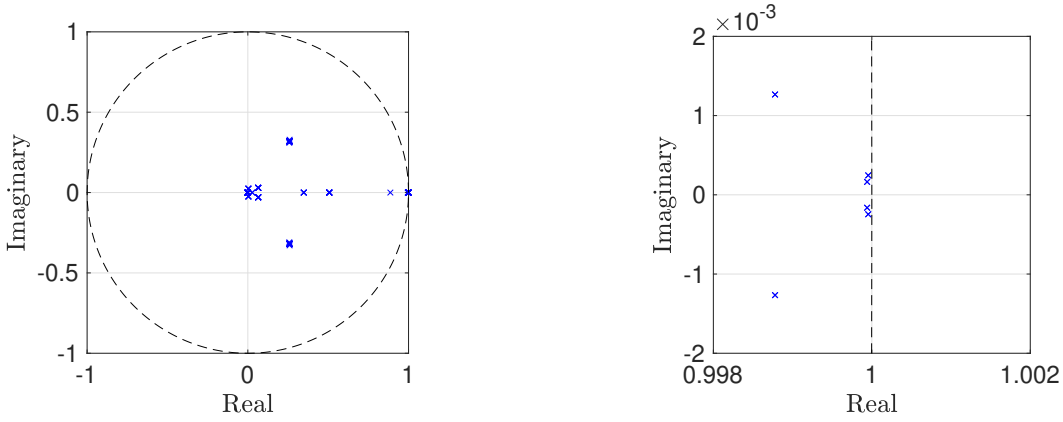

Figure 5.22: Pole plot of the closed-loop system. All eigenvalues of the closed-loop system reside within the unit disk and the unstable poles have been shifted inside (right).

pole appears in both transfer functions. These have been stabilized by the controllers in Eq. 5.46 and 5.47, but the coupling between these degrees-of-freedom imply the lateral position may be regulated through controlling the moments on the disk. The coupling is clear in Fig. 5.17. In addition, the DC gain of the v_x/u_φ and v_y/u_θ frequency responses indicate the following. If the disk is perturbed by a control input u_φ, the disk will move

to a new equilibrium condition in a stabilized system. This new, steady-state equilibrium condition corresponds to $v_\varphi = 0$ but $v_x \neq 0$. Indeed, physically, this is sensible. A moment Q_φ is applied to the disk by a non-zero u_φ. This configuration of the disk will increase the electrostatic forces (due to the gap change) generated by $\mathcal{E}_1$ and $\mathcal{E}_{13}$ while decreasing the forces from their antipodal pairs. In a stabilized system, the disk will seek an equilibrium point and achieve one by shifting in the $-\underline{n}_1$-direction until the moments created by the electrode pairs have cancelled each other out. The frequency responses of v_x/u_φ and v_y/u_θ are shown in Fig. 5.23 with the G_z, G_φ, and G_θ implemented, but $G_x = G_y = 0$. These frequency responses are associated with a stable system so the gain feedback is adequate for low-bandwidth regulation of x and y,

$$G_x = 1, \quad G_y = -1 \tag{5.48}$$

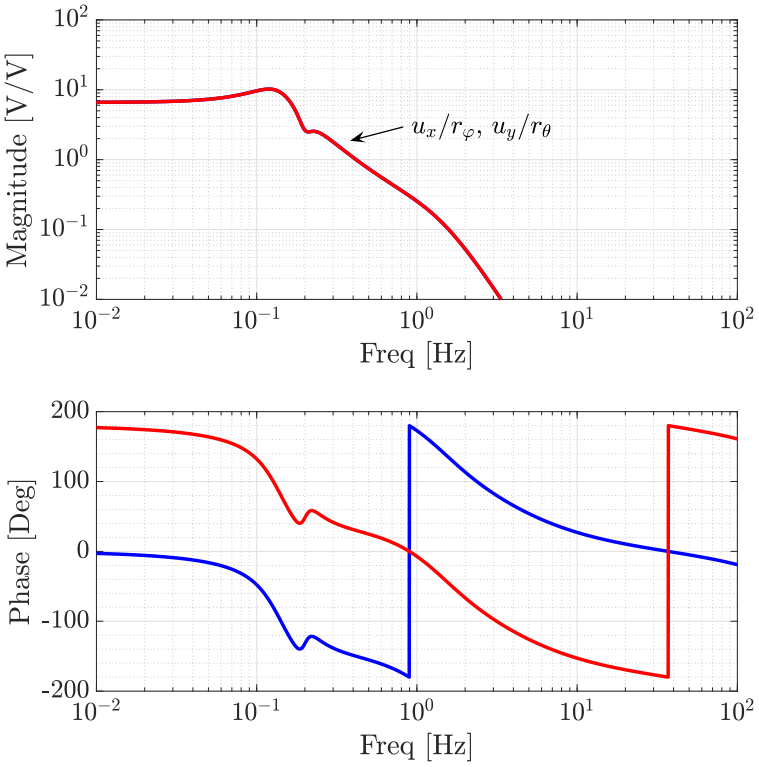

Figure 5.23: Closed-loop frequency responses of v_x/u_φ and v_y/u_θ when $G_x = G_y = 0$. Constant gains can be chosen for G_x and G_y in order to achieve regulation of v_x and v_y.

5.4 Experimental Results and Discussion

5.4.1 Feedforward Filter

The actuator-to-pick-off feedthrough is a consequence of using the electrodes for both sensing and actuation; it must be reduced in order to stabilize the system as it obscures the motional response of the disk. Using this electrode-pick-off configuration reduces the electrode voltages necessary for stabilizing the disk, however, this comes at the cost of significant coupling from controller inputs to measurements. The disk is not stabilizable in practice if the feedthrough is left uncompensated. An accurate estimate of the feedthrough is required so instead of relying on the model to predict the feedthrough, it is simply measured when the disk is at rest on the bottom electrodes (the photoresist and/or small bumpers on the bottom glass plate ensure the disk does not come into contact with the electrodes). Measurements are taken in the decoupled coordinates and represent the three-input/three-output feedthrough transfer function from $\{u_z, u_\varphi, u_\theta\}$ to the output of M in Fig. 5.17. The feedforward, H_{fwd} that is used to cancel the feedthrough is simply an FIR fit to each scalar frequency response.

5.4.2 Closed-loop Tests

The controllers are discretized and implemented as given in Eqs 5.46-5.48. Minor adjustments to the gains $\{K_z, K_\varphi, K_\theta\}$ in Fig. 5.19 are performed. The disk is demonstrated to be stably suspended by introducing pulse disturbances into the closed-loop system at the input of $\tilde{P}$. The pulse is sequentially summed in with the controller outputs in order to perturb u_z ,u_φ, and u_θ. These experiments are shown in Fig. 5.24. As shown, the disk returns to its equilibrium position (offsets in the measurement signals have been removed so 0 V represents the equilibrium configuration of the disk). The input sensitivity function (S_i) frequency response is measured by injecting test signals at the input of $\tilde{P}$. The norm of S_i is shown as a function of frequency in Fig. 5.25. Although the closed-loop system

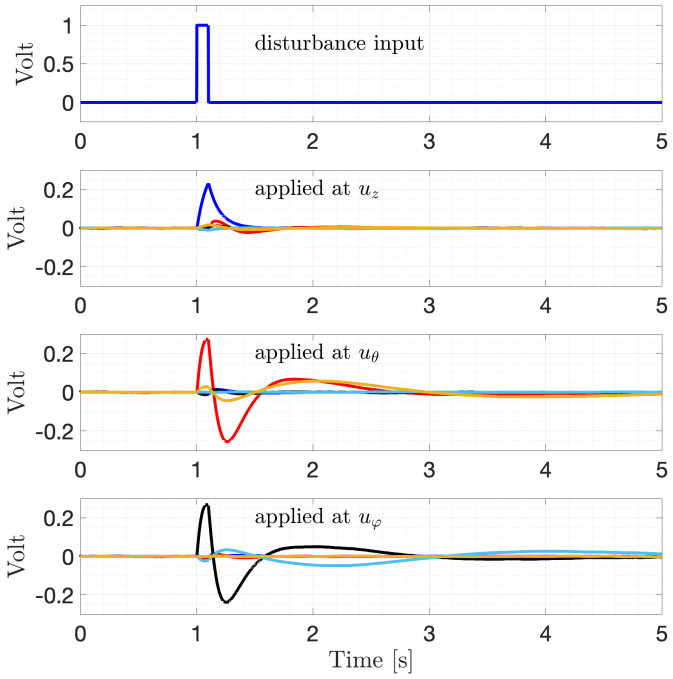

Figure 5.24: Closed-loop tests with pulse disturbances applied at the input of $\tilde{P}$. Outputs of $\{v_z, v_\varphi, v_\theta, v_x, v_y\}$ shown. This demonstrates closed-loop stability, i.e., the disk is suspended without contact.

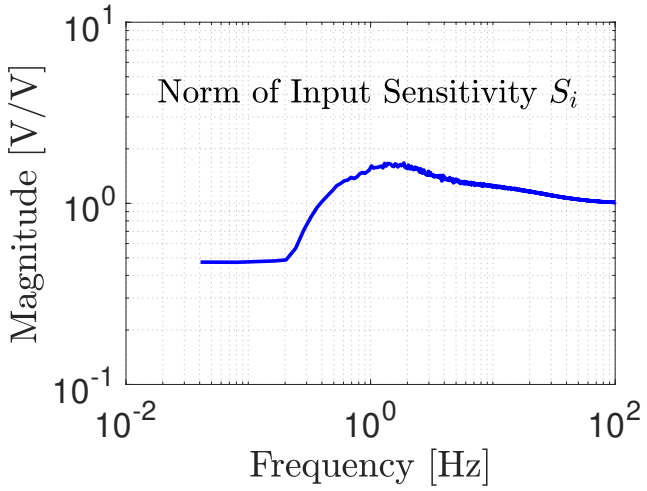

Figure 5.25: Norm of the input sensitivity function S_i.

is not particularly effective in rejecting disturbances at the plant input, the sensitivity function also shows that modest robustness to unstructured plant uncertainty is achieved.

In a similar spirit to the pulse disturbance test, step reference inputs of 0.1 V amplitude are applied to the input of the controllers G_z, G_φ, and G_θ in Fig. 5.26. The step references for r_φ and r_θ are summed in with the output of the G_x and G_y controllers, respectively, while the step reference r_z is summed with the feedback signal from v_z. These reference experiments are conducted separately. Fig. 5.26 not only indicates stability of the closed-loop system, but also demonstrates the coupling between the lateral and tilt degrees-of-freedom. For example, although the step is applied to r_φ, the proxy of φ, v_φ, converges to 0 while a measurement v_x tracks the step input. Similarly, v_y tracks the step input at r_θ. The polarity of the voltage measurement is especially significant. Although both step references have a positive voltage amplitude, the voltage measurement of v_y is negative whereas v_x is positive. This directly corresponds to the preceding physical insight of the tilt inputs of $\tilde{P}$. Namely, $u_\varphi > 0$ implies $v_x < 0$ in steady-state and $u_\theta > 0$, implies $v_y > 0$ as the disk, when stabilized, moves to offset the moments introduced by u_φ and u_θ and each equilibrium (with no tilt). The adjacent figure of Fig. 5.26 shows the corresponding control efforts u_z, $u\varphi$, and u_θ. Here it is seen that $u_\varphi < 0$ in steady-state, a consequence of the DC gain being negative in the controller (Eq. 5.47). Given how $\tilde{P}$ shapes the phase

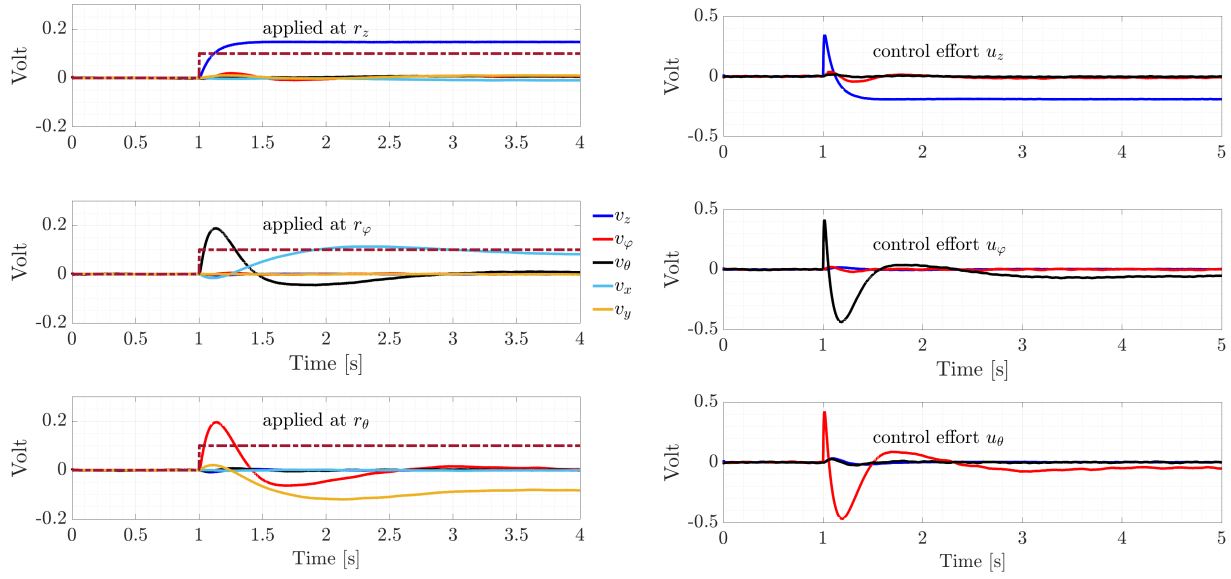

Figure 5.26: (Left) Response of disk to reference signals of 0.1 V amplitude at r_z, r_φ, r_θ. (Right) Corresponding control effort.

(Fig. 5.17), v_x should be positive in steady-state, as seen in Fig. 5.26. Similar conclusions can be drawn for the reference input r_θ.

Step references with 0.2 V amplitude are applied to r_x and r_y in separate experiments. Regulation of the disk's lateral position is demonstrated in Fig. 5.27. Step references with 0.2 V amplitude are applied to r_x and r_y in separate experiments. Again, the step references shed light on the steady-state nature of the system. By analyzing Figs. 5.2 and 5.17, if the desire is to move the disk in a positive $\underline{n}_1$-direction, the disk must be torqued about B_2 such that $\varphi < 0$. This is accomplished in closed-loop by issuing $u_\varphi < 0$. In steady-state, the differential moments introduced by the control In contrast, to lateral move the disk in a positive $\underline{n}_2$-direction, the disk must be torqued such that $\theta > 0$ which is accomplished in closed-loop by $u_\theta > 0$. In both instances, the differential moments generated on the electrodes by the control commands will tend to zero in steady-state as the disk moves laterally (attracted to the larger electrostatic forces). The step references provide a method for analyzing these steady-state properties and these insights are precisely seen in Fig. 5.27.

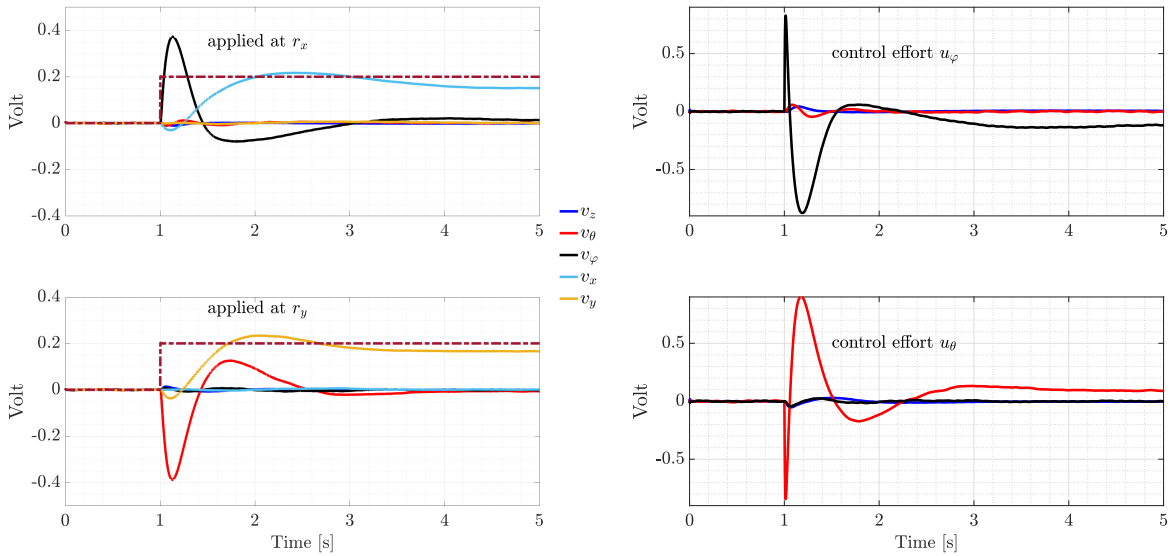

Figure 5.27: (Left) Response of disk to lateral step reference signals of 0.2 V amplitude. (Right) Corresponding control effort.

5.4.3 Estimate of Decoupled Plant Frequency Response

An empirical frequency response of $\tilde{P}$ is derived from the measurement of two closed-loop frequency responses. Broadband and sinusoidal test signals are introduced at the plant input and yield the estimates of the closed-loop frequency response functions $\tilde{P}S_i$ and S_i. The open-loop plant frequency response is derived from these measurements on a frequency-by-frequency basis [Wel81]. The physical plant exhibits coupling between input-output channels that is not present in the model. For example, v_φ and v_θ do not respond to signals applied to u_z in the decoupled plant model, however, the actual system shows u_z coupling to all outputs (Fig. 5.28). Nevertheless, v_z/u_z is the dominant transfer function associated with u_z. Similarly, the decoupled plant model indicates that only v_φ and v_x respond to u_φ, however, the estimates in Fig. 5.29 do show v_φ/u_φ and v_x/u_φ are dominant but that all outputs respond to u_φ. The same conclusion can be made concerning v_θ and v_y with respect to u_θ in Fig. 5.30.

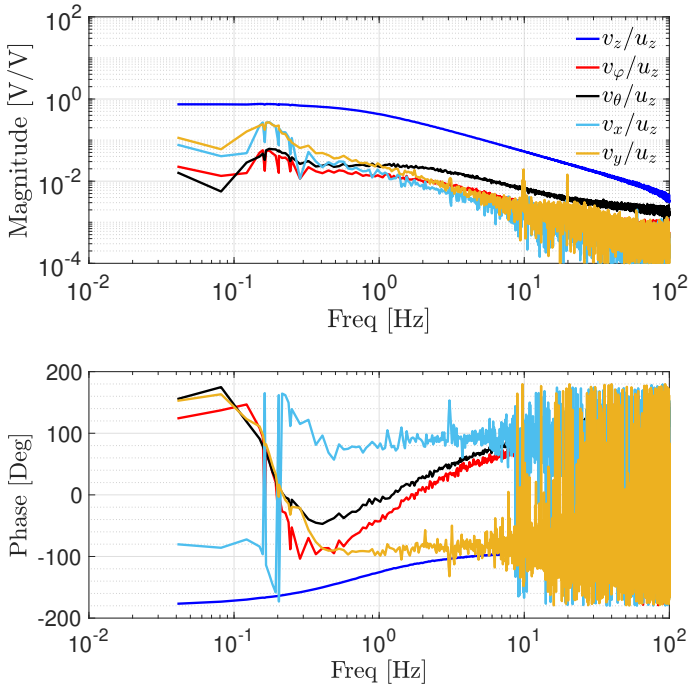

Figure 5.28: Empirical frequency response estimates of the outputs v_z–v_y with u_z input.

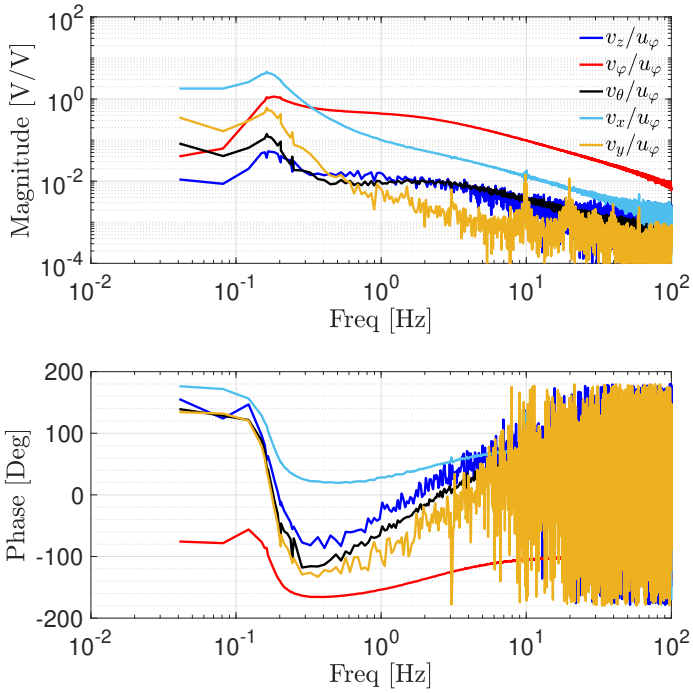

Figure 5.29: Empirical frequency response estimates of the outputs v_z–v_y with u_φ input.

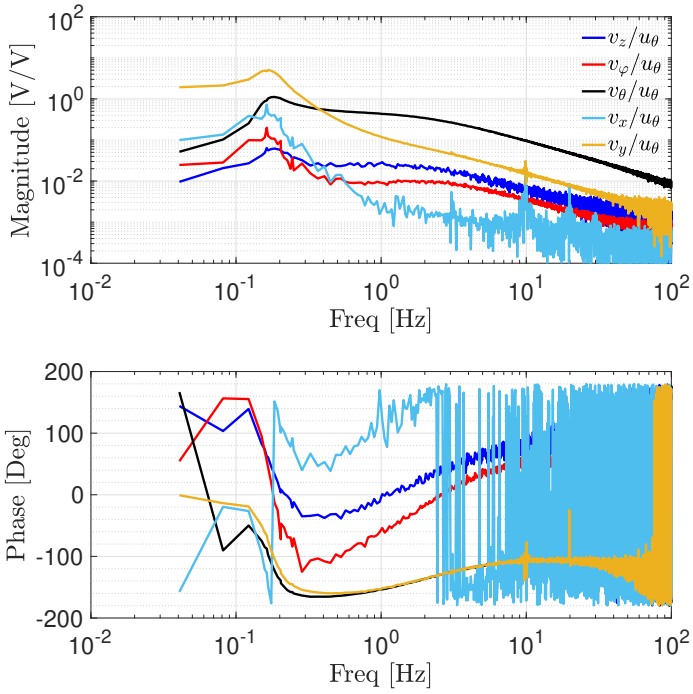

Figure 5.30: Empirical frequency response estimates of the outputs v_z–v_y with u_θ input.

CHAPTER 6

Concluding Remarks

The model and experimental results of an electrostatically suspend disk have been presented. Through analysis of the model, it was determined that an unstable controller was necessary to stabilize the disk's orientation about a desired reference point when the plant is transformed into a decoupled input/output system representative of the kinematic variables parameterizing the disk motion. Open-loop plant estimates were determined in closed-loop tests and show exceptional agreement with the model simulations. Furthermore, additional closed-loop tests, including step responses, reference tracking, and impulse responses were shown to demonstrate the asymptotic stability of the closed-loop system. A number of natural questions arise when comparing the model to closed-loop experiments. Notably, the resonant frequencies appearing in the model and experiments from the open-loop estimates of θ, φ, x, and y differ slightly. Although it seems unimportant, properly modeling these resonances is significant, especially when the tests are moved into a vacuum chamber. In the absence of the squeeze-film damping, the resonances will be lightly damped and the compensation must accurately notch these peaks for the stability and robustness. This is easily mitigated initially in atmospheric tests with a "wide" notch filter. However, this approach may not be possible in a vacuum. Plausible reasons for the inaccuracy could simple due to the estimated squeeze-film damping terms. In particular, the term associated with the tilt DOFs is an estimate based on a rotating rectangle. Another discrepancy is the identical transformers used in the analysis. In practice, these transformers are not all identical and would even introduce "off-diagonal" pieces in the decoupled plant. As seen in experiments, the "off-diagonal" transfer functions are not nec-

essarily negligible, having implications on the control design.

Now, there are several steps still required before testing disk resonators may proceed. First, the system must be miniaturized. The disk resonators to be tested have a stem approximately one centimeter in diameter. Thus, the electrodes must be redesign and fabricated for this new system. Furthermore, an appropriate gap must be settled on given the resonators density in order to suspend the resonator without creating voltage breakdown. Shrinking the nominal gap lowers the breakdown voltage while also increasing the chance of failure due to particle contamination of the electrodes. Another important step is the method of driving and measuring the resonators vibratory response. Typically, electrodes are positioned around the circumference of the disk resonator and are both used as a way to excite and measure the resonator's response. This same method can be applied to a suspended resonator with several considerations kept in mind. First, these electrodes must be placed in such a manner to measure and excite the resonator when it is in its nominal configuration. Care must be taken so as to not disturb an established nominal gap. This would most easily be accomplished by modifying the current structure to include these electrodes during the fabrication process rather than fix some external setup to the platform. However, as shown, lateral stabilization can be achieved with the current electrode configuration. As such, additional electrode may not be necessary to accurately determine the resonator's vibratory response without moving the resonator laterally.

Lastly, this system offers an exciting number of control designs to be studied. While a classical approach has been employed throughout this manuscript, more modern control synthesis techniques should be explored. The normalized coprime factor loop-shaping approach, [MG92], is one such method for synthesizing a robust controller for the decoupled plant. In fact, preliminary analysis of this loop-shaping design method produces a robust, stabilizing controller remarkably similar to the designed controller in Sec. 5.3.7 (c.f. Fig. 5.20), shown in Fig. 6.1. Of particular note is the fact this synthesis procedure produces unstable controllers for the v_φ/u_φ and v_θ/u_θ input/output channels. The unstable poles in the controllers are located at 2.69 rad/s, compared to 3 rad/s for the controller

previously designed. Interestingly, the synthesized controller contains 43 states, whereas

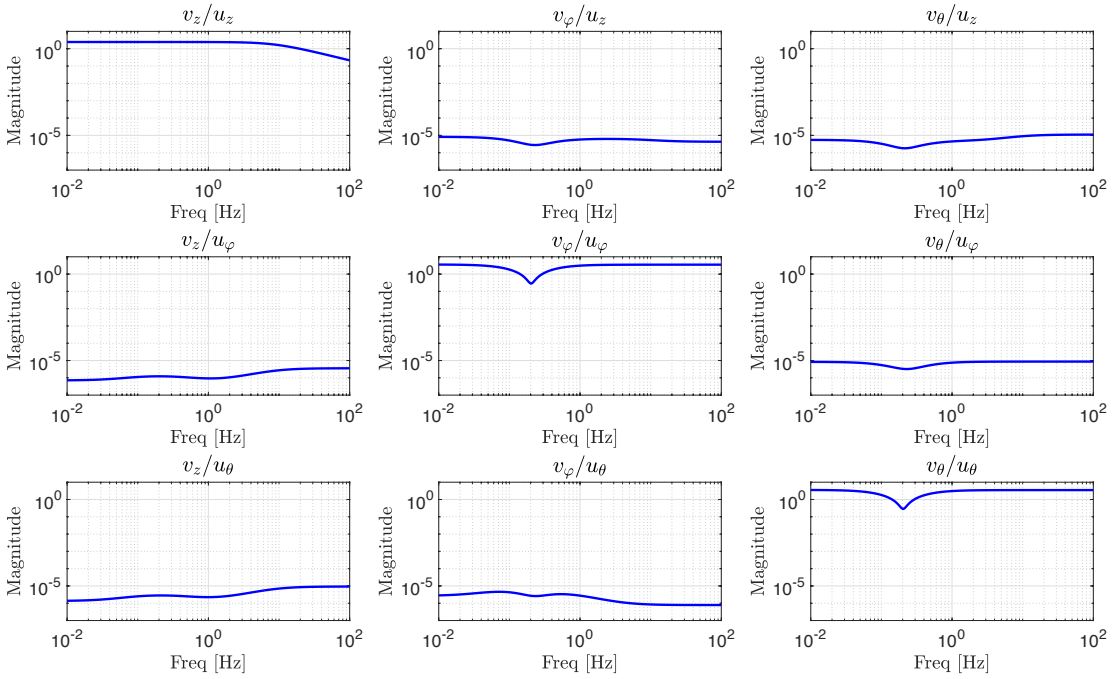

Figure 6.1: Controller (magnitude) synthesized via normalized coprime factors of the decoupled plant with $\epsilon = 0.27$. Of note, the "diagonal" controllers closely match those designed for the decoupled plant in Sec. 5.3.7. The remaining controllers are effectively zero.

the controller implemented on the inner loop of the decoupled plant is effectively 9. The additional states could simply be a result of the construction of the compensated, decoupled plant in the simulation and/or the "off-diagonal" controllers. Regardless, further analysis must be completed in order to determine the practicality of this synthesis procedure. This procedure could also be used to design a robust controller for the suspended disk system where the electrical measurements of the gaps are used (as opposed to the mixed signals) to close the loop. The current model could be used to build a discrete-time observer to be used for compensation. One particular merit of such an approach is the ease of the control design due to the separation principal between the feedback gains and the gain matrix in a state observer model. The idea here would be to use a plant model in the absence of lateral measurements to perform the control of lateral motion. Additionally, parameterization of the transfer functions in the MIMO system would provide a level of completeness to the presented research.

APPENDIX A

Fringing Field Capacitance

Throughout the analysis, the electric field between the controlled equipotential body and electrodes has been assumed to be uniform. In practice, however, the field diverges from uniformity, especially near the boundaries of the electrodes and disk edge. The electric field in these regions is referred to as the fringing field and has been neglected in throughout the presented analysis. Here, this assumption in the context of the electrode-disk system is investigated. Neglecting the influence of the fringe field may lead to significant errors in the electrostatic forces and capacitance. Nonetheless, this is ultimately not the case due to the geometry of the system and the dielectric medium between all the components. Modeling the fringe field in parallel plate capacitors is a classical electrostatic problem and has been thoroughly investigated in various contexts [Lov24], [Jac75], [BC85], [SBS86], [Par91]. This amounts to solving Laplace's equation

$$\nabla^2 \phi = 0 \tag{A.1}$$

where ϕ is the potential dependent on the given coordinate system and the PDE is subject to prescribed boundary conditions. Numerical methods for solving Laplace's equation are often considered [DM79], [BC85], [Par91]. However, the Schwartz-Christoffel transformation provides an exact calculation of the capacitance [Pal37]. Generally, this transformation maps polygons in one complex plane, Z, to an auxiliary plane, ξ, and lastly to a plane, W. The notion is to warp the geometry, via a conformal map to preserve the orthogonal relationships between field lines, and solve Laplace's equation in the new plane.

In [Pal37], the exact capacitance per unit length for finite parallel plates is given by

$$C = \epsilon \frac{K'(k)}{K(k)}$$

where K and K' are the complete elliptic integral of the first kind and complementary complete elliptic integral of the first kind for the elliptic modulus k which is dictated by the geometry of the plates in question. Here, the Schwartz-Christoffel transformation is used to investigate, independently, the fringe field arising from the central electrodes and outboard electrodes in the disk system. Since the purpose is to investigate the capacitance between the electrodes and disk, treating the two fields separately is justified as the mixing of the two fields can be modeled as a parasitic capacitance between the electrode sets. The decision to use such a method over numerical approximation is solely to the ability to obtain a closed form solution.

The following analysis largely follows work presented by [SBS86]. In the case of the capacitance between a central electrode and the disk, the system may be modeled with the two-dimension geometry in Fig. A.1. Here, the disk is in it's nominal position and the view considered is of half the cross-section down an electrode's axis of symmetry. The disk surface is modeled by the infinite plane of the x-axis while a central electrode, with potential v_0 due to the disk's configuration, is the semi-infinite line above. It is not necessary to consider the thickness of the disk in the capacitance calculation as it vanishes with respect of the disk's diameter. The ratio of the distance the disk protrudes from the central electrode to the disk-electrode gap is approximately 35. Although the disk is not protruding in a relatively large amount, modeling the disk by the infinite plane is reasonable when investigating the field near the electrode edge.

With the electrode-disk geometry present in the complex plane as in Fig. A.1, [KOB52] provides dictionary of conformal mappings from Z to W. In Koper, the mapping of this

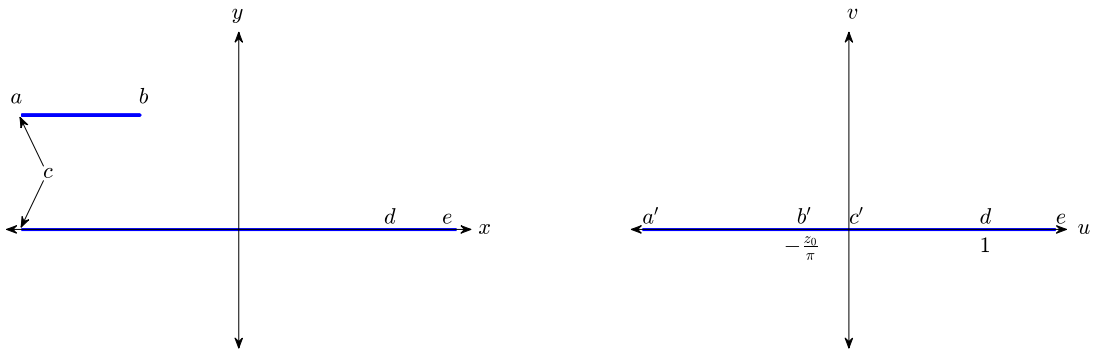

Figure A.1: (Left) 2D electrode-disk geometry in the standard complex plane, $Z = X + jY$. (Right) Transformation (not to scale) to W-plane, $W = U + jV$.

polygon to the upper half-plane in W is

$$Z = W + \frac{z_0}{\pi} \ln W \tag{A.2}$$

where z_0 is the nominal gap. This simplifies solving Laplace's equation to the upper half-plane in W

$$\frac{\partial^2}{\partial U^2}\phi(U,V) + \frac{\partial^2}{\partial V^2}\phi(U,V) = 0 \tag{A.3}$$

subject to the boundary conditions

$$\phi(U,0) = \begin{cases} v_0 & U < 0 \\ \\ 0 & U > 0 \end{cases}. \tag{A.4}$$

Note that the mapping transforms the electrode (represented by the line $a \to b \to c$) to $U < 0$ (the line $a' \to b' \to c'$) and the disk to $U > 0$, thus establishing the above boundary conditions. The Fourier transform (denoted $\mathcal{F}$) can be used to solve Eq. A.3. Consider the Fourier transform of ϕ with respect to the U variable,

$$\hat{\phi}(\xi, v) := \int_{-\infty}^{\infty} \phi(U,V) e^{-j\xi U} dU.$$

This transforms the PDE in Eq. A.3 to an ODE in V

$$-\xi^2\hat{\phi} + \frac{\partial^2}{\partial V^2}\hat{\phi} = 0. \tag{A.5}$$

The solution to Eq. A.5 is

$$\hat{\phi}(\xi, V) = A(\xi)e^{\xi V} + B(\xi)e^{-\xi V}. \tag{A.6}$$

This solution is unbounded in V, however, $\phi(U, V)$ is bounded since it represents the electric potential. Enforcing ϕ to be bounded implies $A(\xi) = 0$ as $V > 0$ and $B(\xi) = 0$ as $V < 0$ (since neither are a function of V). This reduces the solution in A.6 to

$$\hat{\phi}(\xi, V) = C(\xi)e^{-\xi|V|}. \tag{A.7}$$

Applying the boundary condition,

$$\hat{\phi}(\xi, 0) = C(\xi),$$

and the solution to Eq. A.5 is

$$\hat{\phi}(\xi, V) = \hat{\phi}(\xi, 0)e^{-\xi|V|}. \tag{A.8}$$

Note that the inverse Fourier transform ($\mathcal{F}^{-1}$) of $e^{-\xi|V|}$ is

$$\mathcal{F}^{-1}(e^{-\xi|V|}) = \frac{\frac{V}{\pi}}{U^2 + V^2}.$$

Using this result, Eq. A.8, and convolution theorem, the solution to Eq. A.3 is found

$$\begin{aligned}
\phi(U,V) &= \mathcal{F}^{-1}(\hat{\phi}(\xi,0)e^{-\xi|V|}) \\
&= \mathcal{F}^{-1}\left(\mathcal{F}(\phi(U,0))\cdot\mathcal{F}\left(\frac{\frac{V}{\pi}}{U^2+V^2}\right)\right) \\
&= \phi(U,0) * \frac{\frac{V}{\pi}}{U^2+V^2} \\
&= \int_{-\infty}^{\infty}\phi(\tau,0)\,\frac{\frac{V}{\pi}}{(U-\tau)^2+V^2}d\tau \\
&= \frac{v_0}{\pi}\int_{-\infty}^{0}\frac{V}{(U-\tau)^2+V^2}d\tau \\
&= \frac{v_0}{\pi}\tan^{-1}\left(\frac{V}{U}\right) \\
&= \frac{v_0}{\pi}\mathrm{Im}(\ln W)
\end{aligned} \tag{A.9}$$

where $\mathrm{Im}(\cdot)$ indicates the imaginary part of a complex number. The electric field in terms of X and Y are found via $\frac{\partial\phi}{\partial X}$ and $\frac{\partial\phi}{\partial Y}$. Using the fact that $\frac{dZ}{dW} = \frac{W+\frac{z_0}{\pi}}{W}$ and the chain rule, these components are

$$\begin{aligned}
\frac{\partial\phi}{\partial X} &= \frac{v_0}{\pi}\frac{\partial}{\partial X}\,\mathrm{Im}(\ln W) \\
&= \frac{v_0}{\pi}\mathrm{Im}\left(\frac{\partial}{\partial X}\ln W\right) \\
&= \frac{v_0}{\pi}\mathrm{Im}\left(\frac{\partial}{\partial W}\ln W\frac{dW}{dZ}\frac{\partial Z}{\partial X}\right) \\
&= \frac{v_0}{\pi}\mathrm{Im}\left(\frac{1}{W+\frac{z_0}{\pi}}\right)
\end{aligned} \tag{A.10}$$

$$\begin{aligned}
\frac{\partial\phi}{\partial Y} &= \frac{v_0}{\pi}\mathrm{Im}\left(\frac{\partial}{\partial Y}\ln W\right) \\
&= \frac{v_0}{\pi}\mathrm{Im}\left(\frac{\partial}{\partial W}\ln W\frac{dW}{dZ}\frac{\partial Z}{\partial Y}\right) \\
&= \frac{v_0}{\pi}\mathrm{Re}\left(\frac{1}{W+\frac{z_0}{\pi}}\right)
\end{aligned} \tag{A.11}$$

where $\mathrm{Re}(\cdot)$ denotes the real portion of a complex number. On the electrodes, $V = 0$ and

so $\frac{\partial \phi}{\partial X} = 0$ and

$$\frac{\partial \phi}{\partial Y} = \frac{v_0}{\pi} \frac{1}{U + \frac{z_0}{\pi}}. \tag{A.12}$$

In general, the capacitance between a given central electrode and the disk is

$$C_{k,f} = \frac{1}{v_0} \int \sigma \, dA \tag{A.13}$$

where σ is the the charge density over the electrode area. From Gauss's law

$$\sigma = \varepsilon_0 \varepsilon_r \nabla \cdot \mathbf{E}$$

where $\mathbf{E} = -\nabla \phi$ is the vector from of the electric field in terms of X and Y. The $\mathbf{E}$-field is shown Fig. A.2.

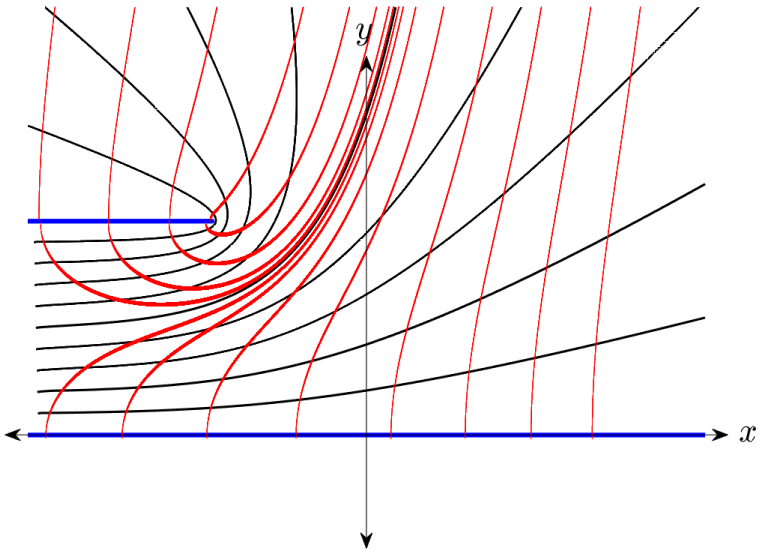

Figure A.2: Potential field (black) and electric field (red) as determined by the potential function in Eq. A.9

.

On the electrode, the component due to X vanishes, simplifying Eq. A.13 to

$$C_{k,f} = \frac{\varepsilon_0 \varepsilon_r}{v_0} \int -\frac{\partial \phi}{\partial Y}\, dA. \tag{A.14}$$

Since the fringe field is in addition to the uniform field, the computation changes on either side of the electrode. As such, the capacitance is computed by considering the upper and lower sides of the electrodes. Due to the electrode's circular shape, the capacitance may be considered on a per unit length basis for the geometry in Fig. A.1 and then integrated over the arc length to find the capacitance. The capacitance per unit length along the line from $a = -\infty$ to $b = \frac{z_0}{\pi}\left(\ln \frac{z_0}{\pi} - 1 + j\pi\right)$ in Fig. A.1 is

$$\begin{aligned}
\frac{\partial C_{k,f}}{\partial r} &= \frac{\varepsilon_0 \varepsilon_r}{v_0} \int_{-\infty}^{b} -\frac{\partial \phi}{\partial Y}\, dX. \\
&= \frac{\varepsilon_0 \varepsilon_r}{\pi} \int_{-\infty}^{-\frac{z_0}{\pi}} -\frac{1}{U + \frac{z_0}{\pi}} \frac{U + \frac{z_0}{\pi}}{U}\, dU \\
&= \frac{\varepsilon_0 \varepsilon_r}{\pi} \int_{-\infty}^{-\frac{z_0}{\pi}} -\frac{1}{U} dU \\
&= -\frac{\varepsilon_0 \varepsilon_r}{\pi} \ln U \Big|_{-\infty}^{-\frac{z_0}{\pi}}
\end{aligned}$$

This integral is unbounded (due to the lower limit), but may be approximated by considering the finite dimension of the electrode and setting the lower bound to r_e, the radius of the central electrodes. The fringing capacitance above the electrode becomes

$$\frac{\partial C_{k,f}}{\partial r} \approx \frac{\varepsilon_0 \varepsilon_r}{\pi} \ln \frac{r_e \pi}{z_0}. \tag{A.15}$$

For the underside of the electrode (spanning b to c), the fringe field is

$$-\left(\frac{\partial \phi}{\partial Y} - \frac{v_0}{z_0}\right) = -\frac{v_0}{\pi}\left(\frac{1}{U + \frac{z_0}{\pi}} - \frac{\pi}{z_0}\right)$$

due to the presence of the uniform field. The capacitance per unit length in this case is

$$\begin{aligned}\frac{\partial C_{k,f}}{\partial r} &= -\frac{\varepsilon_0\varepsilon_r}{\pi}\int_0^{-\frac{z_0}{\pi}}\left(\frac{1}{U+\frac{z_0}{\pi}}-\frac{\pi}{z_0}\right)\frac{U+\frac{z_0}{\pi}}{U}\,dU \\ &= -\frac{\varepsilon_0\varepsilon_r}{\pi}\int_0^{-\frac{z_0}{\pi}}\frac{\pi}{z_0}dU \\ &= \frac{\varepsilon_0\varepsilon_r}{\pi}. \end{aligned} \tag{A.16}$$

By summing Eq. A.15 and A.16, the capacitance per unit length is,

$$\frac{\partial C_{k,f}}{\partial r} \approx \frac{\varepsilon_0}{\pi}\left(1+\ln\frac{r_e\pi}{z_0}\right).$$

Integrating over the arc length of a single electrode ($\frac{\pi r_e}{2}$), the capacitance between a central electrode and the disk is

$$C_{k,f} \approx \frac{\varepsilon_0 r_e}{2}\left(1+\ln\frac{r_e\pi}{z_0}\right) \tag{A.17}$$

which is the result presented in [SBS86]. Evaluating Eq. A.17 with the parameters of the system yields 1.26pF of capacitance due to the fringe field. Compared to the 91.78pF of capacitance in the uniform field of a central electrode, this additional capacitance is negligible. Regarding the outboard electrodes, the same geometry in Fig. A.1 can be argued. From the figure, the electrode extending to $-\infty$ does not tend to the disk center but rather the edge. Further, the disk line extending to $+\infty$ heads towards the disk center. In this case, the gap to overlap (between the disk and an outboard electrode) ratio is roughly 25. So although the infinite lines don't quite resemble the system, the relative dimensions do provide a means of justifying the results near the electrode edge. As such, the same analysis may be applied to the outboard electrodes, indicating the fringe field of the outboard electrodes is also roughly 1.26pF. When compared to the 29.4pF of capacitance arising from a single outboard electrode, the fringe field, albeit relatively more prominent, may still be neglected.

APPENDIX B

Perturbations of the Generalized Forces

In this appendix, the gradients of the generalized forces acting on the disk are expounded. Although tedious, the gradients are insightful for studying the dynamics of the disk due to perturbations in the physical variables as well as the voltages on the electrodes. Since the equations for the forces and moments are similar in structure, the following relation reoccurs in every partial taken

$$\begin{aligned}\frac{\partial}{\partial q_k}\frac{1}{(z_0 \pm z_k)^2} &= -\frac{\frac{\partial}{\partial q_k}\left((z_0 \pm z)^2\right)}{(z_0 \pm z_k)^4} \\ &= \frac{-\frac{\partial}{\partial q_k}(\pm z_j)\left[2(z_0 \pm z)\right]}{(z_0 \pm z_k)^4} \\ &= \frac{\mp 2}{(z_0 \pm z_k)^3}\frac{\partial}{\partial q_k}(z_k)\,. \end{aligned} \tag{B.1}$$

Eq. B.1 will be used to simplify the process of computing the partials of the generalized forces. Referring to the partials in Eq. B.2, the gradient calculations will become cumbersome and difficult to parse with the inclusion of the trigonometric terms.

$$
\begin{aligned}
&\frac{\partial}{\partial x}(z_k) = \tan\varphi\cos\theta, && \forall k \\
&\frac{\partial}{\partial y}(z_k) = -\tan\theta, && \forall k \\
&\frac{\partial}{\partial z}(z_k) = 1, && \forall k \\
&\frac{\partial}{\partial \theta}(z_k) = \begin{cases} -y\sec^2\theta - \left(x + (-1)^{\frac{k-1}{2}} r_0\right)\tan\varphi\sin\theta & k = 1,3 \\ \left(-y + (-1)^{\frac{k}{2}} r_0\right)\sec^2\theta - x\tan\varphi\sin\theta & k = 2,4 \end{cases}, \\
&\frac{\partial}{\partial \varphi}(z_k) = \begin{cases} \left(x + (-1)^{\frac{k-1}{2}} r_0\right)\sec^2\varphi\cos\theta & k = 1,3 \\ x\sec^2\varphi\cos\theta & k = 2,4 \end{cases},
\end{aligned}
\tag{B.2}
$$

Furthermore, due to the equilibrium conditions, these terms effectively become a zero or one anyway. In order to simplify the expressions, without losing any of the meaningful dynamic properties of the system, the small-angle linearization is invoked to only retain the trigonometric terms up to the first order. As such, Eq. B.2 is simplified to

$$
\begin{aligned}
&\frac{\partial}{\partial x}(z_k) = \varphi, && \forall k \\
&\frac{\partial}{\partial y}(z_k) = -\theta, && \forall k \\
&\frac{\partial}{\partial z}(z_k) = 1, && \forall k \\
&\frac{\partial}{\partial \theta}(z_k) = \begin{cases} -y & k = 1,3, \\ \left(-y + (-1)^{\frac{k}{2}} r_0\right) & k = 2,4 \end{cases}, \\
&\frac{\partial}{\partial \varphi}(z_k) = \begin{cases} \left(x + (-1)^{\frac{k-1}{2}} r_0\right) & k = 1,3 \\ x & k = 2,4 \end{cases},
\end{aligned}
\tag{B.3}
$$

As indicated in Eq. 5.28, by applying the small-angle assumption, the normalized general-

ized forces are

$$f_x(q,\dot{q},w) = \varphi\frac{\epsilon_0\epsilon_r A_p}{2m}\sum_{k=1}^{4}\left\{\frac{v_k^2}{(z_0-z_k)^2}-\frac{v_{1k}^2}{(z_0+z_k)^2}\right\} \tag{B.4}$$

$$f_y(q,\dot{q},w) = -\theta\frac{\epsilon_0\epsilon_r A_p}{2m}\sum_{k=1}^{4}\left\{\frac{v_k^2}{(z_0-z_k)^2}-\frac{v_{1k}^2}{(z_0+z_k)^2}\right\} \tag{B.5}$$

$$f_z(q,\dot{q},w) = \frac{\epsilon_0\epsilon_r A_p}{2m}\sum_{k=1}^{4}\left\{\frac{v_k^2}{(z_0-z_k)^2}-\frac{v_{1k}^2}{(z_0+z_k)^2}\right\} \tag{B.6}$$

$$\begin{aligned} f_\theta(q,\dot{q},w) = \frac{\epsilon_0\epsilon_r A_p}{2J_{xy}}\Bigg[&-y\sum_{k=1,3}\left\{\frac{v_k^2}{(z_0-z_k)^2}-\frac{v_{1k}^2}{(z_0+z_k)^2}\right\}+\cdots \\ &\sum_{k=2,4}\left\{\left(-y+(-1)^{\frac{k}{2}}r_0\right)\right\}\left\{\frac{v_k^2}{(z_0-z_k)^2}-\frac{v_{1k}^2}{(z_0+z_k)^2}\right\}\Bigg] \\ &-\frac{1}{J_{xy}}\theta(J_z-J_{xy})\dot{\varphi}^2 \end{aligned} \tag{B.7}$$

$$\begin{aligned} f_\varphi(q,\dot{q},w) = \frac{\epsilon_0\epsilon_r A_p}{2J_{xy}}\Bigg[&\sum_{k=1,3}(x+(-1)^{\frac{k-1}{2}}r_0)\left\{\frac{v_k^2}{(z_0-z_k)^2}-\frac{v_{1k}^2}{(z_0+z_k)^2}\right\}+\cdots \\ &x\sum_{k=2,4}\left\{\frac{v_k^2}{(z_0-z_k)^2}-\frac{v_{1k}^2}{(z_0+z_k)^2}\right\}\Bigg] \\ &-\frac{2\theta}{J_{xy}}(J_z-J_{xy})\dot{\theta}\dot{\varphi} \end{aligned} \tag{B.8}$$

B.1 Gradient of Lateral Forces

The net lateral force in the x-direction normalized by mass is given by Eq. B.4:

$$f_x(q,\dot{q},w) = \varphi\frac{\epsilon_0\epsilon_r A_p}{2m}\sum_{k=1}^{4}\left\{\frac{v_k^2}{(z_0-z_k)^2}-\frac{v_{1k}^2}{(z_0+z_k)^2}\right\}.$$

The gradients of Eq. B.4 are computed as follows. With respect to the transformer vari-

ables, q,

$$\nabla_w f_x(q,\dot{q},w) = \varphi\frac{\epsilon_0\epsilon_r A_p}{m}\sum_{k=1}^{4}\left\{\frac{v_k}{(z_0-z_k)^2}\cdot\underline{e}_k - \frac{v_{1k}}{(z_0+z_k)^2}\cdot\underline{e}_{1k}\right\} \tag{B.9}$$

where $\underline{e}_k$ represents the unit vector in associated with the v_k component of q. The partials of Eq. B.4 with respect to x, y, z, φ, and θ, in light of Eqs. B.1 and B.2, are

$$\begin{aligned}\frac{\partial f_x(q,\dot{q},w)}{\partial x} &= \varphi\frac{\epsilon_0\epsilon_r A_p}{2m}\sum_{k=1}^{4}\left\{v_k^2\frac{\partial}{\partial x}\frac{1}{(z_0-z_k)^2} - v_{1k}^2\frac{\partial}{\partial x}\frac{1}{(z_0+z_k)^2}\right\}\\ &= \varphi^2\frac{\epsilon_0\epsilon_r A_P}{m}\sum_{k=1}^{4}\left\{\frac{v_k^2}{(z_0-z_k)^3} + \frac{v_{1k}^2}{(z_0+z_k)^3}\right\}\end{aligned} \tag{B.10}$$

$$\begin{aligned}\frac{\partial f_x(q,\dot{q},w)}{\partial y} &= \varphi\frac{\epsilon_0\epsilon_r A_P}{2m}\sum_{k=1}^{4}\left\{v_k^2\frac{\partial}{\partial y}\frac{1}{(z_0-z_k)^2} - v_{1k}^2\frac{\partial}{\partial y}\frac{1}{(z_0+z_k)^2}\right\}\\ &= -\varphi\theta\frac{\epsilon_0\epsilon_r A_p}{m}\sum_{k=1}^{4}\left\{\frac{v_k^2}{(z_0-z_k)^3} + \frac{v_{1k}^2}{(z_0+z_k)^3}\right\}\end{aligned} \tag{B.11}$$

$$\begin{aligned}\frac{\partial f_x(q,\dot{q},w)}{\partial z} &= \varphi\frac{\epsilon_0\epsilon_r A_p}{2m}\sum_{k=1}^{4}\left\{v_k^2\frac{\partial}{\partial z}\frac{1}{(z_0-z_k)^2} - v_{1k}^2\frac{\partial}{\partial z}\frac{1}{(z_0+z_k)^2}\right\}\\ &= \varphi\frac{\epsilon_0\epsilon_r A_p}{m}\sum_{k=1}^{4}\left\{\frac{v_k^2}{(z_0-z_k)^3} + \frac{v_{1k}^2}{(z_0+z_k)^3}\right\}\end{aligned} \tag{B.12}$$

$$\begin{aligned}\frac{\partial f_x(q,\dot{q},w)}{\partial \theta} &= \varphi\frac{\epsilon_0\epsilon_r A_p}{2m}\sum_{k=1}^{4}\left\{v_k^2\frac{\partial}{\partial \theta}\frac{1}{(z_0-z_k)^2} - v_{1k}^2\frac{\partial}{\partial \theta}\frac{1}{(z_0+z_k)^2}\right\}\\ &= -y\varphi\frac{\epsilon_0\epsilon_r A_p}{m}\sum_{k=1,3}\left\{\frac{v_k^2}{(z_0-z_k)^3} + \frac{v_{1k}^2}{(z_0+z_k)^3}\right\}\\ &\quad + \varphi\frac{\epsilon_0\epsilon_r A_p}{m}\sum_{k=2,4}\left(-y + (-1)^{\frac{k}{2}} r_0\right)\left\{\frac{v_k^2}{(z_0-z_k)^3} + \frac{v_{1k}^2}{(z_0+z_k)^3}\right\}\end{aligned} \tag{B.13}$$

$$
\begin{aligned}
\frac{\partial f_x(q,\dot{q},w)}{\partial \varphi} &= \frac{\epsilon_0 \epsilon_r A_p}{2m} \sum_{k=1}^{4} \left\{ \frac{v_k^2}{(z_0 - z_k)^2} - \frac{v_{1k}^2}{(z_0 + z_k)^2} \right\} \\
&\quad + \varphi \frac{\epsilon_0 \epsilon_r A_p}{2m} \sum_{k=1}^{4} \left\{ v_k^2 \frac{\partial}{\partial \varphi} \frac{1}{(z_0 - z_k)^2} - v_{1k}^2 \frac{\partial}{\partial \varphi} \frac{1}{(z_0 + z_k)^2} \right\} \\
&= \frac{\epsilon_0 \epsilon_r A_p}{2m} \sum_{k=1}^{4} \left\{ \frac{v_k^2}{(z_0 - z_k)^2} - \frac{v_{1k}^2}{(z_0 + z_k)^2} \right\} \\
&\quad + \varphi \frac{\epsilon_0 \epsilon_r A_p}{m} \sum_{k=1,3} \left(x + (-1)^{\frac{k-1}{2}} r_0 \right) \left\{ \frac{v_k^2}{(z_0 - z_k)^3} + \frac{v_{1k}^2}{(z_0 + z_k)^3} \right\} \\
&\quad + x \frac{\epsilon_0 \epsilon_r A_p}{m} \sum_{k=2,4} \left\{ \frac{v_k^2}{(z_0 - z_k)^3} + \frac{v_{1k}^2}{(z_0 + z_k)^3} \right\}
\end{aligned} \tag{B.14}
$$

Evaluation of Eqs. B.9 - B.14 at the equilibrium condition $q = q_0$ and $q = q_0$ yields

$$f_{x,w} := \nabla_w f_x(q_0, \dot{q}_0, w_0) = 0 \tag{B.15}$$

$$f_{x,x} := \frac{\partial f_x(q_0, \dot{q}_0, w_0)}{\partial x} = 0 \tag{B.16}$$

$$f_{x,y} := \frac{\partial f_x(q_0, \dot{q}_0, w_0)}{\partial y} = 0 \tag{B.17}$$

$$f_{x,z} := \frac{\partial f_x(q_0, \dot{q}_0, w_0)}{\partial z} = 0 \tag{B.18}$$

$$f_{x,\theta} := \frac{\partial f_x(q_0, \dot{q}_0, w_0)}{\partial \theta} = 0 \tag{B.19}$$

$$f_{x,\varphi} := \frac{\partial f_x(q_0, \dot{q}_0, w_0)}{\partial \varphi} = \frac{1}{2mz_0} \sum_{k=1}^{4} C_{k,0}(q_0) \left\{ v_{k,0}^2 - v_{1k,0}^2 \right\} \tag{B.20}$$

$$f_{x,\dot{q}} := \nabla_{\dot{q}} f_x(q_0, \dot{q}_0, w_0) = 0$$

In the analysis, these partials are used to describe the lateral forces in the x-direction due to a perturbation in the system's variables from equilibrium. With no electrodes directly affecting the lateral dynamics of the disk and the absence of the fringe field effects, it is expected that most of these partials would be zero. In essence, the force in the x-direction is only affected by a perturbation in φ. This is reasonable since the disk would only naturally begin to slide in the x-direction if the disk were tilted in φ due to a small force vector emerging from the resultant gravity vector no longer aligned directly with the z-axis. Ex-

amination of Fig. 5.9 elucidates this notion.

In the same fashion, the partials of Eq. B.5 with respect to q, x, y, z, φ, and θ, are

$$\nabla_w f_y(q,\dot{q},w) = -\theta\frac{\epsilon_0\epsilon_r A_p}{m}\sum_{k=1}^{4}\left\{\frac{v_k}{(z_0-z_k)^2}\cdot\underline{e}_k - \frac{v_{1k}}{(z_0+z_k)^2}\cdot\underline{e}_{1k}\right\} \tag{B.21}$$

$$\begin{aligned}\frac{\partial f_y(q,\dot{q},w)}{\partial x} &= -\theta\frac{\epsilon_0\epsilon_r A_p}{2m}\sum_{k=1}^{4}\left\{v_k^2\frac{\partial}{\partial x}\frac{1}{(z_0-z_k)^2} - v_{1k}^2\frac{\partial}{\partial x}\frac{1}{(z_0+z_k)^2}\right\}\\ &= -\varphi\theta\frac{\epsilon_0\epsilon_r A_p}{m}\sum_{k=1}^{4}\left\{\frac{v_k^2}{(z_0-z_k)^3} + \frac{v_{1k}^2}{(z_0+z_k)^3}\right\}\end{aligned} \tag{B.22}$$

$$\begin{aligned}\frac{\partial f_y(q,\dot{q},w)}{\partial y} &= -\theta\frac{\epsilon_0\epsilon_r A_p}{2m}\sum_{k=1}^{4}\left\{v_k^2\frac{\partial}{\partial y}\frac{1}{(z_0-z_k)^2} - v_{1k}^2\frac{\partial}{\partial y}\frac{1}{(z_0+z_k)^2}\right\}\\ &= \theta^2\frac{\epsilon_0\epsilon_r A_p}{m}\sum_{k=1}^{4}\left\{\frac{v_k^2}{(z_0-z_k)^3} + \frac{v_{1k}^2}{(z_0+z_k)^3}\right\}\end{aligned} \tag{B.23}$$

$$\begin{aligned}\frac{\partial f_y(q,\dot{q},w)}{\partial z} &= -\theta\frac{\epsilon_0\epsilon_r A_p}{2m}\sum_{k=1}^{4}\left\{v_k^2\frac{\partial}{\partial z}\frac{1}{(z_0-z_k)^2} - v_{1k}^2\frac{\partial}{\partial z}\frac{1}{(z_0+z_k)^2}\right\}\\ &= -\theta\frac{\epsilon_0\epsilon_r A_p}{m}\sum_{k=1}^{4}\left\{\frac{v_k^2}{(z_0-z_k)^3} + \frac{v_{1k}^2}{(z_0+z_k)^3}\right\}\end{aligned} \tag{B.24}$$

$$
\begin{aligned}
\frac{\partial f_y(q,\dot{q},w)}{\partial\theta} =& -\frac{\epsilon_0\epsilon_r A_p}{2m}\sum_{k=1}^{4}\left\{\frac{v_k^2}{(z_0-z_k)^2}-\frac{v_{1k}^2}{(z_0+z_k)^2}\right\} \\
& -\theta\frac{\epsilon_0\epsilon_r A_p}{2m}\sum_{k=1}^{4}\left\{v_k^2\frac{\partial}{\partial\theta}\frac{1}{(z_0-z_k)^2}-v_{1k}^2\frac{\partial}{\partial\theta}\frac{1}{(z_0+z_k)^2}\right\} \\
=& -\frac{\epsilon_0\epsilon_r A_p}{2m}\sum_{k=1}^{4}\left\{\frac{v_k^2}{(z_0-z_k)^2}-\frac{v_{1k}^2}{(z_0+z_k)^2}\right\} \\
& -y\theta\frac{\epsilon_0\epsilon_r A_p}{m}\sum_{k=1,3}\left\{\frac{v_k^2}{(z_0-z_k)^3}+\frac{v_{1k}^2}{(z_0+z_k)^3}\right\} \\
& +\theta\frac{\epsilon_0\epsilon_r A_p}{m}\sum_{k=2,4}\left(-y+(-1)^{\frac{k}{2}}r_0\right)\left\{\frac{v_k^2}{(z_0-z_k)^3}+\frac{v_{1k}^2}{(z_0+z_k)^3}\right\}
\end{aligned}
\tag{B.25}
$$

$$
\begin{aligned}
\frac{\partial f_y(q,\dot{q},w)}{\partial\varphi} =& -\theta\frac{\epsilon_0\epsilon_r A_p}{2m}\sum_{k=1}^{4}\left\{v_k^2\frac{\partial}{\partial\varphi}\frac{1}{(z_0-z_k)^2}-v_{1k}^2\frac{\partial}{\partial\varphi}\frac{1}{(z_0+z_k)^2}\right\} \\
=& -\theta\frac{\epsilon_0\epsilon_r A_p}{m}\sum_{k=1,3}\left(x+(-1)^{\frac{k-1}{2}}r_0\right)\left\{\frac{v_k^2}{(z_0-z_k)^3}+\frac{v_{1k}^2}{(z_0+z_k)^3}\right\} \\
& -x\theta\frac{\epsilon_0\epsilon_r A_p}{m}\sum_{k=2,4}\left\{\frac{v_k^2}{(z_0-z_k)^3}+\frac{v_{1k}^2}{(z_0+z_k)^3}\right\}
\end{aligned}
\tag{B.26}
$$

Evaluation of Eqs. B.21 - B.26 at the equilibrium condition $q = q_0$ and $q = q_0$ yields

$$f_{y,w} := \nabla_w f_y(q_0,\dot{q}_0,w_0) = 0 \tag{B.27}$$

$$f_{y,x} := \frac{\partial f_y(q_0,\dot{q}_0,w_0)}{\partial x} = 0 \tag{B.28}$$

$$f_{y,y} := \frac{\partial f_y(q_0,\dot{q}_0,w_0)}{\partial y} = 0 \tag{B.29}$$

$$f_{y,z} := \frac{\partial f_y(q_0,\dot{q}_0,w_0)}{\partial z} = 0 \tag{B.30}$$

$$f_{y,\theta} := \frac{\partial f_y(q_0,\dot{q}_0,w_0)}{\partial\theta} = -\frac{1}{2mz_0}\sum_{k=1}^{4}C_{k,0}\left\{v_{k,0}^2-v_{1k,0}^2\right\} \tag{B.31}$$

$$f_{y,\varphi} := \frac{\partial f_y(q_0,\dot{q}_0,w_0)}{\partial\varphi} = 0 \tag{B.32}$$

$$f_{y,\dot{q}} := \nabla_{\dot{q}} f_y(q_0,\dot{q}_0,w_0) = 0$$

These equations reveal the analogous evolution of motion along the y axis. Again, with

no electrodes directly forcing lateral translation in y, the only variable which affects the lateral force in y is θ. From Eq. B.31, a perturbation in θ could cause the disk to slide in the $-y$-direction.

B.2 Gradients of Vertical Force

The net vertical force in the z-direction normalized by mass is given by Eq. B.6:

$$f_z(q,\dot{q},w) = \frac{\epsilon_0\epsilon_r A_p}{2m}\sum_{k=1}^{4}\left\{\frac{v_k^2}{(z_0-z_k)^2} - \frac{v_{1k}^2}{(z_0+z_k)^2}\right\} - \frac{c_z}{m}\dot{z}$$

With respect to the transformer variables q, the gradient of f_z is

$$\nabla_w f_z(q,\dot{q},w) = \frac{\epsilon_0\epsilon_r A_p}{m}\sum_{k=1}^{4}\left\{\frac{v_k}{(z_0-z_k)^2}\cdot\underline{e}_k - \frac{v_{1k}}{(z_0+z_k)^2}\cdot\underline{e}_{1k}\right\} \tag{B.33}$$

where $\underline{e}_k$ represents the unit vector in the direction of the v_k component of q. Further, the partials of Eq. B.6 with respect to x, y, z, φ, and θ, in light of Eqs. B.1 and B.2, are

$$\begin{aligned}\frac{\partial f_z(q,\dot{q},w)}{\partial x} &= \frac{\epsilon_0\epsilon_r A_p}{2m}\sum_{k=1}^{4}\left\{v_k^2\frac{\partial}{\partial x}\frac{1}{(z_0-z_k)^2} - v_{1k}^2\frac{\partial}{\partial x}\frac{1}{(z_0+z_k)^2}\right\}\\ &= \varphi\frac{\epsilon_0\epsilon_r A_p}{m}\sum_{k=1}^{4}\left\{\frac{v_k^2}{(z_0-z_k)^3} + \frac{v_{1k}^2}{(z_0+z_k)^3}\right\}\end{aligned} \tag{B.34}$$

$$\begin{aligned}\frac{\partial f_z(q,\dot{q},w)}{\partial y} &= \frac{\epsilon_0\epsilon_r A_p}{2m}\sum_{k=1}^{4}\left\{v_k^2\frac{\partial}{\partial y}\frac{1}{(z_0-z_k)^2} - v_{1k}^2\frac{\partial}{\partial y}\frac{1}{(z_0+z_k)^2}\right\}\\ &= -\theta\frac{\epsilon_0\epsilon_r A_p}{m}\sum_{k=1}^{4}\left\{\frac{v_k^2}{(z_0-z_k)^3} + \frac{v_{1k}^2}{(z_0+z_k)^3}\right\}\end{aligned} \tag{B.35}$$

$$\frac{\partial f_z(q,\dot{q},w)}{\partial z} = \frac{\epsilon_0\epsilon_r A_p}{2m}\sum_{k=1}^{4}\left\{v_k^2\frac{\partial}{\partial z}\frac{1}{(z_0-z_k)^2} - v_{1k}^2\frac{\partial}{\partial z}\frac{1}{(z_0+z_k)^2}\right\}$$
$$= \frac{\epsilon_0\epsilon_r A_p}{m}\sum_{k=1}^{4}\left\{\frac{v_k^2}{(z_0-z_k)^3} + \frac{v_{1k}^2}{(z_0+z_k)^3}\right\} \tag{B.36}$$

$$\frac{\partial f_z(q,\dot{q},w)}{\partial \theta} = \frac{\epsilon_0\epsilon_r A_p}{2m}\sum_{k=1}^{4}\left\{v_k^2\frac{\partial}{\partial \theta}\frac{1}{(z_0-z_k)^2} - v_{1k}^2\frac{\partial}{\partial \theta}\frac{1}{(z_0+z_k)^2}\right\}$$
$$= -y\frac{\epsilon_0\epsilon_r A_p}{m}\sum_{k=1,3}\left\{\frac{v_k^2}{(z_0-z_k)^3} + \frac{v_{1k}^2}{(z_0+z_k)^3}\right\} \tag{B.37}$$
$$+ \frac{\epsilon_0\epsilon_r A_p}{m}\sum_{k=2,4}\left(-y + (-1)^{\frac{k}{2}}r_0\right)\left\{\frac{v_k^2}{(z_0-z_k)^3} + \frac{v_{1k}^2}{(z_0+z_k)^3}\right\}$$

$$\frac{\partial f_z(q,\dot{q},w)}{\partial \varphi} = \frac{\epsilon_0\epsilon_r A_p}{2m}\sum_{k=1}^{4}\left\{v_k^2\frac{\partial}{\partial \varphi}\frac{1}{(z_0-z_k)^2} - v_{1k}^2\frac{\partial}{\partial \varphi}\frac{1}{(z_0+z_k)^2}\right\}$$
$$= \frac{\epsilon_0\epsilon_r A_p}{m}\sum_{k=1,3}\left(x + (-1)^{\frac{k-1}{2}}r_0\right)\left\{\frac{v_k^2}{(z_0-z_k)^3} + \frac{v_{1k}^2}{(z_0+z_k)^3}\right\} \tag{B.38}$$
$$+ x\frac{\epsilon_0\epsilon_r A_p}{m}\sum_{k=2,4}\left\{\frac{v_k^2}{(z_0-z_k)^3} + \frac{v_{1k}^2}{(z_0+z_k)^3}\right\} \tag{B.39}$$

$$\nabla_{\dot{q}} f_z = \begin{bmatrix} 0 & 0 & -\frac{c_z}{m} & 0 & 0 \end{bmatrix} \tag{B.40}$$

Evaluation of Eqs. B.33 - B.40 at the equilibrium condition $q = q_0$ and $q = q_0$ yields

$$f_{z,w} := \nabla_w f_z(q_0, \dot{q}_0, w_0) = \frac{1}{mz_0} \sum_{k=1}^{4} C_{k,0} \left\{ v_{k,0} \cdot \underline{e}_k - v_{1k} \cdot \underline{e}_{1k} \right\} \tag{B.41}$$

$$f_{z,x} := \frac{\partial f_z(q_0, \dot{q}_0, w_0)}{\partial x} = 0 \tag{B.42}$$

$$f_{z,y} := \frac{\partial f_z(q_0, \dot{q}_0, w_0)}{\partial y} = 0 \tag{B.43}$$

$$f_{z,z} := \frac{\partial f_z(q_0, \dot{q}_0, w_0)}{\partial z} = \frac{1}{mz_0^2} \sum_{k=1}^{4} C_{k,0} \left\{ v_{k,0}^2 + v_{1k,0}^2 \right\} \tag{B.44}$$

$$f_{z,\theta} := \frac{\partial f_z(q_0, \dot{q}_0, w_0)}{\partial \theta} = \frac{r_0}{mz_0^2} \sum_{k=2,4} (-1)^{\frac{k}{2}} C_{k,0} \left\{ v_{k,0}^2 + v_{1k,0}^2 \right\} = 0 \tag{B.45}$$

$$f_{z,\varphi} := \frac{\partial f_z(q_0, \dot{q}_0, w_0)}{\partial \varphi} = \frac{r_0}{mz_0^2} \sum_{k=1,3} (-1)^{\frac{k-1}{2}} C_{k,0} \left\{ v_{k,0}^2 + v_{1k,0}^2 \right\} = 0 \tag{B.46}$$

$$f_{z,\dot{q}} := \nabla_{\dot{q}} f_z(q_0, \dot{q}_0, w_0) = \begin{bmatrix} 0 & 0 & -\frac{c_z}{m} & 0 & 0 \end{bmatrix} \tag{B.47}$$

Perturbations in the lateral directions should have no direct effect on the vertical forces acting on the disk. These perturbations would bear no impact on the electrode voltages (since the gap in-between would remain unchanged) and therefore only change the moment arms acting on the disk center of mass. Small changes in the angular rotations also would not perturb the disk center of mass vertically. Although these perturbations change the electrode-disk gaps, the net vertical electrostatic force is rendered to be zero. In Eq. B.45 and B.46, the symmetry of the electrode configuration lead to the result. Elaboration of Eq. B.46 shows

$$f_{z,\varphi} = \frac{r_0}{mz_0^2} \left(C_{1,0} \left\{ v_{1,0}^2 + v_{11,0}^2 \right\} - C_{3,0} \left\{ v_{3,0}^2 + v_{13,0}^2 \right\} \right).$$

Since $C_{1,0} = C_{3,0}$, $v_{1,0} = v_{3,0}$ and $v_{11,0} = v_{13,0}$, $f_{z,\varphi} = 0$. Similarly, $f_{z,\theta} = 0$. As a result, the only variables which induce vertical motion of the disk from equilibrium are perturbations in q and z. Due to the attractive nature of the electrostatic forces, a positive perturbation in z should cause the disk to accelerate upwards, as evident in Eq. B.44.

B.3 Gradients of Torques

From Eq. B.7, the net torque about the x-axis (normalized by the corresponding inertia) is given as:

$$\begin{aligned} f_\theta(q,\dot{q},w) = \frac{\epsilon_0\epsilon_r A_p}{2J_{xy}}\Bigg[& -y\sum_{k=1,3}\left\{\frac{v_k^2}{(z_0-z_k)^2}-\frac{v_{1k}^2}{(z_0+z_k)^2}\right\}+\cdots \\ & \sum_{k=2,4}\left(-y+(-1)^{\frac{k}{2}}r_0\right)\cos\theta-\left\{\frac{v_k^2}{(z_0-z_k)^2}-\frac{v_{1k}^2}{(z_0+z_k)^2}\right\}\Bigg] \\ & -\frac{1}{J_{xy}}\theta(J_z-J_{xy})\dot{\varphi}^2-\frac{c_\theta}{J_{xy}}\dot{\theta} \end{aligned}$$

With respect to q, the gradient of f_θ is

$$\begin{aligned} \nabla_x f_\theta(q,\dot{q},w) = \frac{\epsilon_0\epsilon_r A_p}{J_{xy}}\Bigg[& -y\sum_{k=1,3}\left\{\frac{v_k}{(z_0-z_k)^2}\underline{e}_k-\frac{v_{1k}}{(z_0+z_k)^2}\underline{e}_{1k}\right\}+\cdots \\ & \sum_{k=2,4}\left(-y+(-1)^{\frac{k}{2}}r_0\right)\left\{\frac{v_k}{(z_0-z_k)^2}\underline{e}_k-\frac{v_{1k}}{(z_0+z_k)^2}\underline{e}_{1k}\right\}\Bigg] \end{aligned} \tag{B.48}$$

The partials of Eq. B.7 with respect to x, y, z, θ, and φ, using Eqs. B.1 and B.2, are computed to be

$$\begin{aligned} \frac{\partial f_\theta(q,\dot{q},w)}{\partial x} = & -y\frac{\epsilon_0\epsilon_r A_p}{2J_{xy}}\sum_{k=1,3}\left\{v_k^2\frac{\partial}{\partial x}\frac{1}{(z_0-z_k)^2}-v_{1k}^2\frac{\partial}{\partial x}\frac{1}{(z_0+z_k)^2}\right\} \\ & +\frac{\epsilon_0\epsilon_r A_p}{2J_{xy}}\sum_{k=2,4}(-y+(-1)^{\frac{k}{2}}r_0)\left\{v_k^2\frac{\partial}{\partial x}\frac{1}{(z_0-z_k)^2}-v_{1k}^2\frac{\partial}{\partial x}\frac{1}{(z_0+z_k)^2}\right\} \\ = & -y\varphi\frac{\epsilon_0\epsilon_r A_p}{J_{xy}}\sum_{k=1,3}\left\{\frac{v_k^2}{(z_0-z_k)^3}+\frac{v_{1k}^2}{(z_0+z_k)^3}\right\} \\ & +\varphi\frac{\epsilon_0\epsilon_r A_p}{J_{xy}}\sum_{k=2,4}(-y+(-1)^{\frac{k}{2}}r_0)\left\{\frac{v_k^2}{(z_0-z_k)^3}+\frac{v_{1k}^2}{(z_0+z_k)^3}\right\} \end{aligned} \tag{B.49}$$

$$
\begin{aligned}
\frac{\partial f_\theta(q,\dot{q},w)}{\partial y} =& -\frac{\epsilon_0\epsilon_r A_p}{2J_{xy}}\sum_{k=1}^{4}\left\{\frac{v_k^2}{(z_0-z_k)^2}-\frac{v_{1k}^2}{(z_0+z_k)^2}\right\} \\
& -y\frac{\epsilon_0\epsilon_r A_p}{2J_{xy}}\sum_{k=1,3}\left\{v_k^2\frac{\partial}{\partial y}\frac{1}{(z_0-z_k)^2}-v_{1k}^2\frac{\partial}{\partial y}\frac{1}{(z_0+z_k)^2}\right\} \\
& +\frac{\epsilon_0\epsilon_r A_p}{2J_{xy}}\sum_{k=2,4}(-y+(-1)^{\frac{k}{2}}r_0)\left\{v_k^2\frac{\partial}{\partial y}\frac{1}{(z_0-z_k)^2}-v_{1k}^2\frac{\partial}{\partial y}\frac{1}{(z_0+z_k)^2}\right\} \\
=& -\frac{\epsilon_0\epsilon_r A_p}{2J_{xy}}\sum_{k=1}^{4}\left\{\frac{v_k^2}{(z_0-z_k)^2}-\frac{v_{1k}^2}{(z_0+z_k)^2}\right\} \\
& +y\theta\frac{\epsilon_0\epsilon_r A_p}{J_{xy}}\sum_{k=1,3}\left\{\frac{v_k^2}{(z_0-z_k)^3}+\frac{v_{1k}^2}{(z_0+z_k)^3}\right\} \\
& -\theta\frac{\epsilon_0\epsilon_r A_p}{J_{xy}}\sum_{k=2,4}(-y+(-1)^{\frac{k}{2}}r_0)\left\{\frac{v_k^2}{(z_0-z_k)^3}+\frac{v_{1k}^2}{(z_0+z_k)^3}\right\}
\end{aligned}
\tag{B.50}
$$

$$
\begin{aligned}
\frac{\partial f_\theta(q,\dot{q},w)}{\partial z} =& -y\frac{\epsilon_0\epsilon_r A_p}{2J_{xy}}\sum_{k=1,3}\left\{v_k^2\frac{\partial}{\partial z}\frac{1}{(z_0-z_k)^2}-v_{1k}^2\frac{\partial}{\partial z}\frac{1}{(z_0+z_k)^2}\right\} \\
& +\frac{\epsilon_0\epsilon_r A_p}{2J_{xy}}\sum_{k=2,4}(-y+(-1)^{\frac{k}{2}}r_0)\left\{v_k^2\frac{\partial}{\partial z}\frac{1}{(z_0-z_k)^2}-v_{1k}^2\frac{\partial}{\partial z}\frac{1}{(z_0+z_k)^2}\right\} \\
=& -y\frac{\epsilon_0\epsilon_r A_p}{J_{xy}}\sum_{k=1,3}\left\{\frac{v_k^2}{(z_0-z_k)^3}+\frac{v_{1k}^2}{(z_0+z_k)^3}\right\} \\
& +\frac{\epsilon_0\epsilon_r A_p}{J_{xy}}\sum_{k=2,4}(-y+(-1)^{\frac{k}{2}}r_0)\left\{\frac{v_k^2}{(z_0-z_k)^3}+\frac{v_{1k}^2}{(z_0+z_k)^3}\right\}
\end{aligned}
\tag{B.51}
$$

$$
\begin{aligned}
\frac{\partial f_\theta(q,\dot{q},w)}{\partial \theta} =& -y\frac{\epsilon_0\epsilon_r A_p}{2J_{xy}}\sum_{k=1,3}\left\{v_k^2\frac{\partial}{\partial\theta}\frac{1}{(z_0-z_k)^2}-v_{1k}^2\frac{\partial}{\partial\theta}\frac{1}{(z_0+z_k)^2}\right\}\\
&+\frac{\epsilon_0\epsilon_r A_p}{2J_{xy}}\sum_{k=2,4}(-y+(-1)^{\frac{k}{2}}r_0)\left\{v_k^2\frac{\partial}{\partial\theta}\frac{1}{(z_0-z_k)^2}-v_{1k}^2\frac{\partial}{\partial\theta}\frac{1}{(z_0+z_k)^2}\right\}\\
&-\frac{1}{J_{xy}}(J_z-J_{xy})\dot{\varphi}^2\\
=& y^2\frac{\epsilon_0\epsilon_r A_p}{J_{xy}}\sum_{k=1,3}\left\{\frac{v_k^2}{(z_0-z_k)^3}+\frac{v_{1k}^2}{(z_0+z_k)^3}\right\}\\
&+\frac{\epsilon_0\epsilon_r A_p}{J_{xy}}\sum_{k=2,4}(-y+(-1)^{\frac{k}{2}}r_0)^2\left\{\frac{v_k^2}{(z_0-z_k)^3}+\frac{v_{1k}^2}{(z_0+z_k)^3}\right\}\\
&-\frac{1}{J_{xy}}(J_z-J_{xy})\dot{\varphi}^2
\end{aligned}
\tag{B.52}
$$

$$
\begin{aligned}
\frac{\partial f_\theta(q,\dot{q},w)}{\partial \varphi} =& -y\frac{\epsilon_0\epsilon_r A_p}{2J_{xy}}\sum_{k=1,3}\left\{v_k^2\frac{\partial}{\partial\varphi}\frac{1}{(z_0-z_k)^2}-v_{1k}^2\frac{\partial}{\partial\varphi}\frac{1}{(z_0+z_k)^2}\right\}\\
&+\frac{\epsilon_0\epsilon_r A_p}{2J_{xy}}\sum_{k=2,4}(-y+(-1)^{\frac{k}{2}}r_0)\left\{v_k^2\frac{\partial}{\partial\varphi}\frac{1}{(z_0-z_k)^2}-v_{1k}^2\frac{\partial}{\partial\varphi}\frac{1}{(z_0+z_k)^2}\right\}\\
=& -y\frac{\epsilon_0\epsilon_r A_p}{J_{xy}}\sum_{k=1,3}(x+(-1)^{\frac{k-1}{2}}r_0)\left\{\frac{v_k^2}{(z_0-z_k)^3}+\frac{v_{1k}^2}{(z_0+z_k)^3}\right\}\\
&+x\frac{\epsilon_0\epsilon_r A_p}{J_{xy}}\sum_{k=2,4}(-y+(-1)^{\frac{k}{2}}r_0)\left\{\frac{v_k^2}{(z_0-z_k)^3}+\frac{v_{1k}^2}{(z_0+z_k)^3}\right\}
\end{aligned}
\tag{B.53}
$$

$$
\nabla_{\dot{q}} f_\theta = \begin{bmatrix} 0 & 0 & 0 & -\frac{c_\theta}{J_{xy}} & -\frac{1}{J_{xy}}(J_z-J_{xy})\theta\dot{\varphi}\end{bmatrix} \tag{B.54}
$$

$$f_{\theta,q} := \nabla_q f_\theta(q_0, \dot{q}_0, w_0) = \frac{r_0}{J_{xy} z_0} \sum_{k=2,4} (-1)^{\frac{k}{2}} C_{k,0} \left\{ v_{k,0} \cdot \underline{e}_k - v_{1k,0} \cdot \underline{e}_{1k} \right\} \tag{B.55}$$

$$f_{\theta,x} := \frac{\partial f_\theta(q_0, \dot{q}_0, w_0)}{\partial x} = 0 \tag{B.56}$$

$$f_{\theta,y} := \frac{\partial f_\theta(q_0, \dot{q}_0, w_0)}{\partial y} = -\frac{1}{2 J_{xy} z_0} \sum_{k=1}^{4} C_{k,0} \left\{ v_{k,0}^2 - v_{1k,0}^2 \right\} \tag{B.57}$$

$$f_{\varphi,z} := \frac{\partial f_\theta(q_0, \dot{q}_0, w_0)}{\partial z} = \frac{r_0}{J_{xy} z_0^2} \sum_{k=2,4} (-1)^{\frac{k}{2}} C_{k,0} \left\{ v_{k,0}^2 + v_{1k,0}^2 \right\} = 0 \tag{B.58}$$

$$f_{\theta,\theta} := \frac{\partial f_\theta(q_0, \dot{q}_0, w_0)}{\partial \theta} = \frac{r_0^2}{J_{xy} z_0^2} \sum_{k=2,4} C_{k,0} \left\{ v_{k,0}^2 + v_{1k,0}^2 \right\} \tag{B.59}$$

$$f_{\theta,\varphi} := \frac{\partial f_\theta(q_0, \dot{q}_0, w_0)}{\partial \varphi} = 0 \tag{B.60}$$

$$f_{\theta,\dot{q}} := \nabla_{\dot{q}} f_\theta(q_0, \dot{q}_0, w_0) = \begin{bmatrix} 0 & 0 & 0 & -\frac{c_\theta}{J_{xy}} & 0 \end{bmatrix} \tag{B.61}$$

Perturbations in x, z, and φ do not imbalance the electrostatic forces arising from $\mathcal{E}_2$, $\mathcal{E}_{12}$, $\mathcal{E}_4$, and $\mathcal{E}_{14}$. As such, no net torque is induced with respect to θ and corroborated by Eqs. B.56, B.58, and B.60. A perturbation in y effectively shortens the moment arm in the direction of $+y$ and lengthens the moment arm in the direction of $-y$. Under the equilibrium conditions, this change in y would torque the disk clockwise with respect to the x-axis, e.g., produce a torque opposing the positive convention for θ. Eq. B.57 validates this notion. Again the attractive nature of the electrostatic forces is made clear in Eq. B.59, where a tilt in θ would cause an angular acceleration in the positive direction of θ.

Given in Eq. B.8, the net torque about the y-axis (normalized by the corresponding inertia) is

$$\begin{aligned} f_\varphi(q, \dot{q}, w) = {} & \frac{\epsilon_0 \epsilon_r A_p}{2 J_{xy}} \sum_{k=1,3} (x + (-1)^{\frac{k-1}{2}} r_0) \left\{ \frac{v_k^2}{(z_0 - z_k)^2} - \frac{v_{1k}^2}{(z_0 + z_k)^2} \right\} \\ & + x \frac{\epsilon_0 \epsilon_r A_p}{2 J_{xy}} \sum_{k=2,4} \left\{ \frac{v_k^2}{(z_0 - z_k)^2} - \frac{v_{1k}^2}{(z_0 + z_k)^2} \right\} \\ & - \frac{2\theta}{J_{xy}} (J_z - J_{xy}) \dot{\theta} \dot{\varphi} - \frac{c_\varphi}{J_{xy}} \dot{\varphi} \end{aligned}$$

As before, the partials of Eq. B.8 with respect to q, x, y, z, θ, and φ, are found to be

$$\nabla_q f_\varphi(q,\dot{q},w) = \frac{\epsilon_0\epsilon_r A_p}{J_{xy}} \sum_{k=1,3} (x + (-1)^{\frac{k-1}{2}} r_0) \left\{ \frac{v_k}{(z_0 - z_k)^2} \cdot \underline{e}_k - \frac{v_{1k}}{(z_0 + z_k)^2} \cdot \underline{e}_{1k} \right\} + x \frac{\epsilon_0\epsilon_r A_p}{J_{xy}} \sum_{k=2,4} \left\{ \frac{v_k}{(z_0 - z_k)^2} \cdot \underline{e}_k - \frac{v_{1k}}{(z_0 + z_k)^2} \cdot \underline{e}_{1k} \right\} \tag{B.62}$$

$$\begin{aligned} \frac{\partial f_\varphi(q,\dot{q},w)}{\partial x} &= \frac{\epsilon_0\epsilon_r A_p}{2J_{xy}} \sum_{k=1}^{4} \left\{ \frac{v_k^2}{(z_0 - z_k)^2} - \frac{v_{1k}^2}{(z_0 + z_k)^2} \right\} \\ &\quad + \frac{\epsilon_0\epsilon_r A_p}{2J_{xy}} \sum_{k=1,3} (x + (-1)^{\frac{k-1}{2}} r_0) \left\{ v_k^2 \frac{\partial}{\partial x} \frac{1}{(z_0 - z_k)^2} - v_{1k}^2 \frac{\partial}{\partial x} \frac{1}{(z_0 + z_k)^2} \right\} \\ &\quad + x \frac{\epsilon_0\epsilon_r A_p}{2J_{xy}} \sum_{k=2,4} \left\{ v_k^2 \frac{\partial}{\partial x} \frac{1}{(z_0 - z_k)^2} - v_{1k}^2 \frac{\partial}{\partial x} \frac{1}{(z_0 + z_k)^2} \right\} \\ &= \frac{\epsilon_0\epsilon_r A_p}{2J_{xy}} \sum_{k=1}^{4} \left\{ \frac{v_k^2}{(z_0 - z_k)^2} - \frac{v_{1k}^2}{(z_0 + z_k)^2} \right\} \\ &\quad + \varphi \frac{\epsilon_0\epsilon_r A_p}{J_{xy}} \sum_{k=1,3} (x + (-1)^{\frac{k-1}{2}} r_0) \left\{ \frac{v_k^2}{(z_0 - z_k)^3} + \frac{v_{1k}^2}{(z_0 + z_k)^3} \right\} \\ &\quad + \varphi x \frac{\epsilon_0\epsilon_r A_p}{J_{xy}} \sum_{k=2,4} \left\{ \frac{v_k^2}{(z_0 - z_k)^3} + \frac{v_{1k}^2}{(z_0 + z_k)^3)} \right\} \end{aligned} \tag{B.63}$$

$$\begin{aligned} \frac{\partial f_\varphi(q,\dot{q},w)}{\partial y} &= \frac{\epsilon_0\epsilon_r A_p}{2J_{xy}} \sum_{k=1,3} (x + (-1)^{\frac{k-1}{2}} r_0) \left\{ v_k^2 \frac{\partial}{\partial y} \frac{1}{(z_0 - z_k)^2} - v_{1k}^2 \frac{\partial}{\partial y} \frac{1}{(z_0 + z_k)^2} \right\} \\ &\quad + x \frac{\epsilon_0\epsilon_r A_p}{2J_{xy}} \sum_{k=2,4} \left\{ v_k^2 \frac{\partial}{\partial y} \frac{1}{(z_0 - z_k)^2} - v_{1k}^2 \frac{\partial}{\partial y} \frac{1}{(z_0 + z_k)^2} \right\} \\ &= -\theta \frac{\epsilon_0\epsilon_r A_p}{J_{xy}} \sum_{k=1,3} (x + (-1)^{\frac{k-1}{2}} r_0) \left\{ \frac{v_k^2}{(z_0 - z_k)^3} + \frac{v_{1k}^2}{(z_0 + z_k)^3} \right\} \\ &\quad - \theta x \frac{\epsilon_0\epsilon_r A_p}{J_{xy}} \sum_{k=2,4} \left\{ \frac{v_k^2}{(z_0 - z_k)^3} + \frac{v_{1k}^2}{(z_0 + z_k)^3)} \right\} \end{aligned} \tag{B.64}$$

$$\begin{aligned}\frac{\partial f_\varphi(q,\dot{q},w)}{\partial z} &= \frac{\epsilon_0\epsilon_r A_p}{2J_{xy}}\sum_{k=1,3}(x+(-1)^{\frac{k-1}{2}}r_0)\left\{v_k^2\frac{\partial}{\partial z}\frac{1}{(z_0-z_k)^2}-v_{1k}^2\frac{\partial}{\partial z}\frac{1}{(z_0+z_k)^2}\right\}\\ &\quad+x\frac{\epsilon_0\epsilon_r A_p}{2J_{xy}}\sum_{k=2,4}\left\{v_k^2\frac{\partial}{\partial z}\frac{1}{(z_0-z_k)^2}-v_{1k}^2\frac{\partial}{\partial z}\frac{1}{(z_0+z_k)^2}\right\}\\ &= \frac{\epsilon_0\epsilon_r A_p}{J_{xy}}\sum_{k=1,3}(x+(-1)^{\frac{k-1}{2}}r_0)\left\{\frac{v_k^2}{(z_0-z_k)^3}+\frac{v_{1k}^2}{(z_0+z_k)^3}\right\}\\ &\quad+x\frac{\epsilon_0\epsilon_r A_p}{J_{xy}}\sum_{k=2,4}\left\{\frac{v_k^2}{(z_0-z_k)^3}+\frac{v_{1k}^2}{(z_0+z_k)^3)}\right\}\end{aligned}\tag{B.65}$$

$$\begin{aligned}\frac{\partial f_\varphi(q,\dot{q},w)}{\partial \theta} &= \frac{\epsilon_0\epsilon_r A_p}{2J_{xy}}\sum_{k=1,3}(x+(-1)^{\frac{k-1}{2}}r_0)\left\{v_k^2\frac{\partial}{\partial \theta}\frac{1}{(z_0-z_k)^2}-v_{1k}^2\frac{\partial}{\partial \theta}\frac{1}{(z_0+z_k)^2}\right\}\\ &\quad+x\frac{\epsilon_0\epsilon_r A_p}{2J_{xy}}\sum_{k=2,4}\left\{v_k^2\frac{\partial}{\partial \theta}\frac{1}{(z_0-z_k)^2}-v_{1k}^2\frac{\partial}{\partial \theta}\frac{1}{(z_0+z_k)^2}\right\}\\ &\quad-\frac{2}{J_{xy}}(J_z-J_{xy})\dot{\theta}\dot{\varphi}\\ &= -y\frac{\epsilon_0\epsilon_r A_p}{J_{xy}}\sum_{k=1,3}(x+(-1)^{\frac{k-1}{2}}r_0)\left\{\frac{v_k^2}{(z_0-z_k)^3}+\frac{v_{1k}^2}{(z_0+z_k)^3}\right\}\\ &\quad+x\frac{\epsilon_0\epsilon_r A_p}{J_{xy}}\sum_{k=2,4}(-y+(-1)^{\frac{k}{2}}r_0)\left\{\frac{v_k^2}{(z_0-z_k)^3}+\frac{v_{1k}^2}{(z_0+z_k)^3}\right\}\\ &\quad-\frac{2}{J_{xy}}(J_z-J_{xy})\dot{\theta}\dot{\varphi}\end{aligned}\tag{B.66}$$

$$\begin{aligned}\frac{\partial f_\varphi(q,\dot{q},w)}{\partial \varphi} &= \frac{\epsilon_0\epsilon_r A_p}{2J_{xy}}\sum_{k=1,3}(x+(-1)^{\frac{k-1}{2}}r_0)\left\{v_k^2\frac{\partial}{\partial \varphi}\frac{1}{(z_0-z_k)^2}-v_{1k}^2\frac{\partial}{\partial \varphi}\frac{1}{(z_0+z_k)^2}\right\}\\ &\quad+x\frac{\epsilon_0\epsilon_r A_p}{2J_{xy}}\sum_{k=2,4}\left\{v_k^2\frac{\partial}{\partial \varphi}\frac{1}{(z_0-z_k)^2}-v_{1k}^2\frac{\partial}{\partial \varphi}\frac{1}{(z_0+z_k)^2}\right\}\\ &= \frac{\epsilon_0\epsilon_r A_p}{J_{xy}}\sum_{k=1,3}(x+(-1)^{\frac{k-1}{2}}r_0)^2\left\{\frac{v_k^2}{(z_0-z_k)^3}+\frac{v_{1k}^2}{(z_0+z_k)^3}\right\}\\ &\quad+x^2\frac{\epsilon_0\epsilon_r A_p}{J_{xy}}\sum_{k=2,4}\left\{\frac{v_k^2}{(z_0-z_k)^3}+\frac{v_{1k}^2}{(z_0+z_k)^3}\right\}\end{aligned}\tag{B.67}$$

$$\nabla_{\dot{q}}f_\varphi=\begin{bmatrix}0 & 0 & 0 & -\frac{2\theta}{J_{xy}}(J_z-J_{xy})\dot{\varphi} & -\frac{2\theta}{J_{xy}}(J_z-J_{xy})\dot{\theta}-\frac{c_\varphi}{J_{xy}}\end{bmatrix}\tag{B.68}$$

Upon evaluating Eqs. B.62–B.67 at the equilibrium condition,

$$f_{\varphi,q} := \nabla_q f_\varphi(q_0, \dot{q}_0, w_0) = \frac{r_0}{J_{xy} z_0} \sum_{k=1,3} (-1)^{\frac{k-1}{2}} C_{k,0} \left\{ v_{k,0} \cdot \underline{e}_k - v_{1k,0} \cdot \underline{e}_{1k} \right\} \tag{B.69}$$

$$f_{\varphi,x} := \frac{\partial f_\varphi(q_0, \dot{q}_0, w_0)}{\partial x} = \frac{1}{2 J_{xy} z_0} \sum_{k=1}^{4} C_{k,0} \left\{ v_{k,0}^2 - v_{1k,0}^2 \right\} \tag{B.70}$$

$$f_{\varphi,y} := \frac{\partial f_\varphi(q_0, \dot{q}_0, w_0)}{\partial y} = 0 \tag{B.71}$$

$$f_{\varphi,z} := \frac{\partial f_\varphi(q_0, \dot{q}_0, w_0)}{\partial z} = \frac{r_0}{J_{xy} z_0^2} \sum_{k=1,3} (-1)^{\frac{k-1}{2}} C_{k,0} \left\{ v_{k,0}^2 + v_{1k,0}^2 \right\} = 0 \tag{B.72}$$

$$f_{\varphi,\theta} := \frac{\partial f_\varphi(q_0, \dot{q}_0, w_0)}{\partial \theta} = 0 \tag{B.73}$$

$$f_{\varphi,\varphi} := \frac{\partial f_\varphi(q_0, \dot{q}_0, w_0)}{\partial \varphi} = \frac{r_0^2}{J_{xy} z_0^2} \sum_{k=1,3} C_{k,0} \left\{ v_{k,0}^2 + v_{1k,0}^2 \right\} \tag{B.74}$$

$$f_{\varphi,\dot{q}} := \nabla_{\dot{q}} f_\varphi(q_0, \dot{q}_0, w_0) = \begin{bmatrix} 0 & 0 & 0 & 0 & -\frac{c_\varphi}{J_{xy}} \end{bmatrix} \tag{B.75}$$

The analogous arguments made for the accelerations seen in θ can be made for φ. In doing so, the only non-zero accelerations for φ would be expected to appear in Eqs. B.69, B.70, and B.74.

REFERENCES

[AB75] James L. Atkinson and Joseph C. Boltinghouse. "Speed control for an electrostatically suspended ball gyroscope." U.S. Patent 3 906 804, 1975.

[Atk67] James L. Atkinson. "Electrostatic bearing." U.S. Patent 3 334 949, 1967.

[BC85] D F Bartlett and T R Corle. "The circular parallel plate capacitor: a numerical solution for the potential." Journal of Physics A: Mathematical and General, **18**(9):1337–1342, jun 1985.

[BKS17] A. H. Behbahani, D. Kim, P. Stupar, J. DeNatale, and R. T. M'Closkey. "Tailored Etch Profiles for Wafer-Level Frequency Tuning of Axisymmetric Resonators." J. Microelectromech. Syst., pp. 1–11, 2017. to appear.

[BY07] Minhang Bao and Heng Yang. "Squeeze film air damping in MEMS." Sensors and Actuators A: Physical, **136**(1):3 – 27, 2007. 25th Anniversary of Sensors and Actuators A: Physical.

[DFT91] John C. Doyle, Bruce A. Francis, and Allen R. Tannenbaum. Feedback Control Theory. Prentice Hall, New York, 1991.

[DM79] M. DiStasio and W. C. McHarris. "Electrostatic problems? Relax!" American Journal of Physics, **47**(5):440–444, 1979.

[GK03] M. V. Gindila and M. Kraft. "Electronic interface design for an electrically floating micro-disc." J. Micromech. Microeng., **13**:S11 – S16, 2003.

[Hal63] Jack K. Hale. Oscillations in nonlinear systems. McGraw-Hill Book Company, Inc., New York, 1963.

[HGW02] Feng Tian Han, Zhongyu Gao, and Yongliang Wang. "A differential capacitance to voltage converter for electrostatic levitation applications." Sensors and Actuators A: Physical, **99**(3):249 – 255, 2002.

[Jac75] J. D. Jackson. Classical Electrodynamics. Wiley, New York, 1975.

[JTK99] V. Josselin, P. Touboul, and R. Kielbasa. "Capacitive detection scheme for space accelerometers applications." Sensors and Actuators A: Physical, **78**(2–3):92 – 98, 1999.

[KOB52] H. KOBER. Dictionary of conformal representations. Dover, New-York, 1952.

[LHK95] Lu Jin, T. Higuchi, and M. Kanemoto. "Electrostatic levitator for hard disk media." IEEE Transactions on Industrial Electronics, **42**(5):467–473, 1995.

[Lov24] A. E. H. Love. "Some Electrostatic Distributions in two Dimensions." Proceedings of the London Mathematical Society, **s2-22**(1):337–369, 1924.

[MEF03] Takao Murakoshi, Yasuo Endo, Keisuke Fukatsu, Sigeru Nakamura, and Masayoshi Esashi. "Electrostatically Levitated Ring-Shaped Rotational-Gyro/Accelerometer." Japanese Journal of Applied Physics, **42**(Part 1, No. 4B):2468–2472, apr 2003.

[MG92] D. McFarlane and K. Glover. "A loop-shaping design procedure using H/sub infinity / synthesis." IEEE Transactions on Automatic Control, **37**(6):759–769, 1992.

[Pal37] H. B. Palmer. "The Capacitance of a Parallel-Plate Capacitor by the Schwartz-Christoffel Transformation." Transactions of the American Institute of Electrical Engineers, **56**(3):363–366, 1937.

[Par91] G. W. Parker. "What is the Capacitance of Parallel Plates?" Computers in Physics, **5**(5):534–540, 1991.

[SBS86] G J Sloggett, N G Barton, and S J Spencer. "Fringing fields in disc capacitors." Journal of Physics A: Mathematical and General, **19**(14):2725–2736, oct 1986.

[SKS15] D.M. Schwartz, D. Kim, P. Stupar, J. DeNatale, and R.T. M'Closkey. "Modal Parameter Tuning of an Axisymmetric Resonator via Mass Perturbation." J. Microelectromech. Syst., **24**(3):545–555, June 2015.

[TTM02] R. Toda, N. Takeda, T. Murakoshi, S. Nakamura, and M. Esashi. "Electrostatically levitated spherical 3-axis accelerometer." In Technical Digest. MEMS 2002 IEEE International Conference. Fifteenth IEEE International Conference on Micro Electro Mechanical Systems (Cat. No.02CH37266), pp. 710–713, Jan 2002.

[TWM12] T. Terasawa, T. Watanabe, and T. Murakoshi. "Electrostatically levitated ring-shaped rotational-gyro/accelerometer using all-digital OFDM detection with TAD." In SENSORS, 2012 IEEE, pp. 1–4, 2012.

[Vid85] Mathukumalli Vidyasagar. Control System Synthesis: A Factorization Approach. MIT Press, 3rd edition, 1985.

[Wel81] Peter E. Wellstead. "Non-parametric methods of system identification." Automatica, **17**(1):55 – 69, 1981.

[WYH10] E. van West, Akio Yamamoto, and Toshiro Higuchi. "Manipulation of Thin Objects Using Levitation Techniques, Tilt Control, and Haptics." IEEE Transactions on Automation Science and Engineering, **7**(3):451–462, 2010.